Metal sulfide-based nanomaterials for electrochemical CO_2 reduction

Mukherjee, Anirban; Abdinejad, Maryam; Mahapatra, Susanta Sinha; Ruidas, Bidhan Chandra

DOI
10.1039/d2ta08209h

Publication date
2023

Document Version
Final published version

Published in
Journal of Materials Chemistry A

Journal of Materials Chemistry A

ROYAL SOCIETY OF CHEMISTRY

REVIEW

View Article Online
View Journal

Cite this: DOI: 10.1039/d2ta08209h

Metal sulfide-based nanomaterials for electrochemical CO_2 reduction

Anirban Mukherjee, [a] Maryam Abdinejad, *[b] Susanta Sinha Mahapatra [c] and Bidhan Chandra Ruidas *[a]

Received 20th October 2022
Accepted 6th April 2023

DOI: 10.1039/d2ta08209h

rsc.li/materials-a

The electrochemical CO_2 reduction (ECO_2R) is critical to enabling the widespread use of abundant renewable energy sources. However, in order to successfully implement such technologies on an industrial scale, necessary advancement in both the material and molecular design of electrocatalysts is required. In recent years, metal-sulfide (MS)-based nanomaterials have been explored as promising electrocatalysts for ECO_2R. This article provides a systematic review of the design and development of MS-based catalysts for ECO_2R, including their synthesis, characterization, reaction mechanism, catalytic performance, and strategies for future optimization. The current state-of-the-art MS-based ECO_2R catalysts and their technical challenges are outlined herein with the purpose of establishing new guidelines for the rational design of next generation MS-based catalysts for CO_2 electroreduction.

1 Introduction

The excessive usage of fossil fuels leads to their rapid depletion, CO_2 emission, and other toxic gases in the atmosphere, resulting in global warming and climate change.[1,2] To overcome this problem, a decrease in CO_2 emissions through effective CO_2 capture, utilization, and storage approach has been considered in the past few years (Fig. 1).[3,4] The conversion of carbon dioxide to valuable products has emerged as a promising technology for CO_2 utilization over the past decades, which can be executed *via* thermochemical,[5] photochemical,[6] photoelectrochemical,[7] electrochemical,[8] and biochemical[9] processes. Among all, the electrochemical CO_2 reduction (ECO_2R) to valuable chemicals and chemical feedstocks such as small C_1 products (mainly carbon monoxide, formic acid methane, and methanol)[10–13] and high-energy dense C_{2+} products (ethylene, ethanol, *n*-propanol),[14–16] has drawn significant attention among the aforementioned processes due to its (a) tunability of the procedure (*e.g.*, potential and temperature), (b) compatibility with media (*e.g.*, organic and aqueous), and (c) scalability.[17,18]

However, the ECO_2R is challenging due to the stable and chemically inert linear CO_2 molecule.[19,20] CO_2 transformation is driven by nucleophilic attacks at the carbon molecule, which is an energy uphill procedure requiring a considerable input of energy (750 kJ mol^{-1} required to break the C=O bond) and convert to valuable chemicals.[21] The conversion mechanism is a complex process that involves multiple proton-coupled electron transfers (PCET) and may comprise several side reactions and intermediates.[22] In this regard, the electrocatalysts are instrumental in ECO_2R to overcome the kinetically sluggish reaction and promote the PCET reaction. Therefore, early research emphasized developing different solid-state electrocatalysts and discovering several reaction intermediates or final products formed during catalysis.

When conducted in aqueous electrolytes, the ECO_2R inhibits by competition from the HER (Hydrogen Evolution Reaction), which occurs in the same potential window as the ECO_2R but with lower thermodynamic barriers due to the energetically favorable proton adsorption and reduction than CO_2 activation. Evidently, the high stability of the CO_2 molecule necessitates the use of large overpotentials for the reactant to be adsorbed and activated at the active site. However, the HER outperforms the ECO_2R due to faster kinetics at high overpotentials, resulting in a high FE (Faradaic Efficiency) for hydrogen generation at

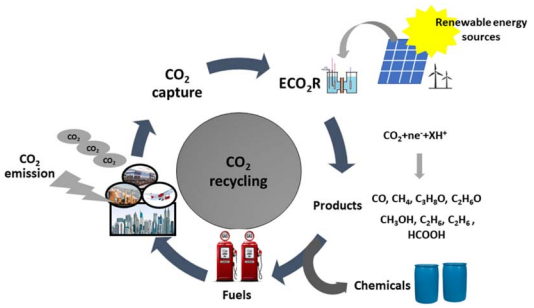

Fig. 1 A schematic representation of closed-loop CO_2 recycling.

[a]Department of Chemical Engineering, Birla Institute of Technology, Mesra, Ranchi 835215, India. E-mail: bidhanruidas@gmail.com

[b]Materials for Energy Conversion and Storage (MECS), Department of Chemical Engineering, The Delft University of Technology, van der Maasweg 9, 2629 HZ Delft, The Netherlands

[c]Department of Chemistry, Birla Institute of Technology, Mesra, Ranchi 835215, India

the expense of selectivity for CO_2 reduction products. Therefore, special attention should be paid to the design of catalyst systems that maximize product selectivity for ECO_2R and suppress proton reduction as much as possible. So far, according to the final product selectivity, ECO_2R catalysts are divided into four classes.[22] For instance: – (i) Cd, Hg, Sn, In, Bi, Pb: produce formate as the primary product with high faradaic efficiencies;[23–27] (ii) Au, Ag, Zn, Pd: provide high binding strength of *COOH intermediates into electrode surface resulting in a fast reduction to *CO intermediates followed by CO production;[28–35] (iii) Ni, Fe, Si, V, Pt: produce H_2 due to the low overpotential towards hydrogen evolution reaction (HER);[36–39] (iv) Cu yield 16 valuable compounds under different operating conditions, including various multi-carbon products depending on the *COH or *CHO intermediates.[40] In this regard, Hori *et al.*[41] performed ECO_2R in 0.5 M $KHCO_3$ at 5 mA cm^{-2} for one hour on different polycrystalline metal electrodes. The results are illustrated in Table 1.[42] This Table 1 exhibits that a significant overpotential is required for each metal electrode to achieve a specific current density (here -5 mA cm^{-2}). The lowest overpotential (0.6 V) is required for Au to obtain CO (87%), while the highest (1.1 V) is required for Pb to obtain formate (97%). In addition to the aforementioned transition metal electrocatalysts, metal oxides (MOs),[43,44] MXenes,[45,46] transition metal chalcogenides (TMDs),[47,48] metal-functionalized porphyrin-based structures,[49,50] nitrogen-based electrocatalysts,[51–53] and aerogels[54,55] are also reported to have promising catalytic ECO_2R activity.

Despite the significant advancement that has been achieved, some bottlenecks still exist with the practical application of ECO_2R, including high overpotential, slow reaction rate resulting in low current densities, competitive HER, poor product selectivity, and unsatisfactory stability.[56,57] First, the process requires high overpotential and predominantly suffers from considerable energy input due to the thermodynamic stability of CO_2 molecules. Then, the complex PCET steps and the low solubility of the CO_2 in an aqueous electrolyte hinder the electron transfer kinetics. The low current density ($j < 200$ mA cm^{-2}) and poor faradaic efficiency (FE<90%) are insufficient to meet the scale-up demands.[58–60] As the reduction process produces several products and intermediates, it makes the reaction paths more complex. Finally, the reaction selectivity is found to be considerably lower due to a competitive HER.[61] For these scenarios, advanced research efforts have been desired to design and develop novel, economic, and robust electrocatalysts that can convert CO_2 at high rates with a minimum overpotential.

Considering those limitations, metal-sulfide-based (MS-based) nanomaterials are particularly attractive as possible electrocatalysts or precursors due to their unique properties, such as high electrical conductivity and good electrochemical stability compared to their corresponding metal oxide field.[62–67] Furthermore, the following properties make them a flexible class of materials for the design of electrocatalysts: (1) higher electrical conductivity than other semiconductor materials, layered MS-based nanomaterials often have good metallic conductivity.[68,69] (2) Adjustable composition, crystalline phase, structural and morphological features of functional materials.[70,71] (3) An appropriate band gaps. The band gap has a direct impact on d-orbital filling and electronic character. At the Fermi energy level (E_f), the density of states is dominated by d-orbital electron states.[72,73] (4) Different atomic vibration modes, which will directly affect the surface state of the catalyst and the adsorption mode of the reaction intermediates, so it is directly related to the active sites.[74] These remarkable properties motivated extensive research on every aspect of these materials, with innumerable works investigating their electronic structure, synthesis techniques, and catalytic performance for ECO_2R. Indeed, the design of ECO_2R catalytic systems capable of overcoming all bottlenecks is becoming a critical topic in the

Table 1 Different metals with the FE of several products produced at a particular potential and constant current density[a]

Group no.	Metal	E (V *vs.* RHE)	j_{total} (mA cm^{-2})	CO (%)	CH_4 (%)	C_2H_4 (%)	EtOH (%)	PrOH (%)	$HCOO^-$ (%)	H_2 (%)	Total (%)
(i)	Pb	−1.24	5.0	0	0	0	0	0	97.4	5.0	102.4
	Hg	−1.12	5.0	0	0	0	0	0	99.5	0	99.5
	Tl	−1.21	5.0	0	0	0	0	0	95.1	6.2	101.3
	In	−1.16	5.0	2.1	0	0	0	0	94.9	3.3	100.3
	Sn	−1.09	5.0	7.1	0	0	0	0	88.4	4.6	100.1
	Cd	−1.24	5.0	13.9	1.3	0	0	0	78.4	9.4	103.0
(ii)	Au	−0.65	5.0	87.1	0	0	0	0	0.7	10.2	98.0
	Ag	−0.98	5.0	81.5	0	0	0	0	0.6	12.4	94.6
	Zn	−1.15	5.0	79.4	0	0	0	0	6.1	9.9	95.4
	Pd	−0.81	5.0	28.3	2.9	0	0	0	2.8	26.2	60.2
	Ga	−0.85	5.0	23.2	0	0	0	0	0	79.0	102.0
(iii)	Ni	−1.09	5.0	0	1.8	0.1	0	0	1.4	88.9	92.4
	Fe	−0.52	5.0	0	0	0	0	0	0	94.8	94.8
	Pt	−0.68	5.0	0	0	0	0	0	0.1	95.7	95.8
	Ti	−1.21	5.0	Tr	0	0	0	0	0	99.7	99.7
(iv)	Cu	−1.05	5.0	1.3	33.3	25.5	5.7	3.0	9.4	20.5	103.5

[a] The potential values have been converted from the reported standard hydrogen electrode (SHE) potential to the reversible hydrogen electrode (RHE) scale [$T = 18.5$ °C, pH = 6.8] by adding (RT/F) ln 10 pH = 0 : 39 V: (Copyright 2019, American Chemical Society)[42]

context of the widespread adoption of these electrocatalytic technologies. Till now, several physical and chemical methodologies have been developed for preparing high-quality MS-based nanomaterials, including mono, bi, and multi-metallic sulfides.[75] Based on those methodologies, synthesis methods are divided into a 'top-down' and 'bottom-up approach.[76–78] The top-down approach uses mechanical methods to crush bulk materials into smaller pieces to generate nanoparticles. Many top-down approaches, including sputtering,[79,80] electrospinning,[81,82] lithography,[83,84] ball-milling,[85,86] exfoliation,[87–90] *etc.*, are already reported in the literature for MS-based nanomaterials synthesis. The bottom-up technique is a well-known approach to synthesizing structures of nanomaterials made atom-by-atom or molecule-by-molecule. The atoms/molecules are attached through covalent or non-covalent bonds.[91] The commonly used bottom-up approaches are chemical vapour decomposition,[92,93] atomic layer deposition,[94,95] spray pyrolysis,[96,97] pulsed layer deposition,[98,99] thermal deposition,[100,101] combustion,[102,103] micro-emulsion,[104,105] precipitation,[106,107] hydrothermal,[108–111] solvothermal,[112,113] sulfidation,[114,115] microwave irradiation,[116–118] and electrodeposition.[119,120] Thus, the strong connections between the various nanomaterials and their unique properties have encouraged research to perform the controlled fabrication of noble electrocatalysts with modified nanostructures.

This review attempts to fill the gap and create a pedagogical guide on the morphology and structural variation of MS-based nanomaterials in terms of their unique capacity and control over the CO_2 reduction process. It provides an overview of the various synthesis methods for MS-based nanomaterials preparation and their structural, chemical, and physical properties modification for ECO_2R. The correlation between synthesis methods, metal loading, sulfur concentration, morphology, and structures to the catalytic activity will also be summarized. Finally, insights on future research and development of MS-based compounds for next-generation ECO_2R catalysts will be discussed.

2 Metal-sulfide-based electrocatalysts for ECO_2R

MS-based electrocatalysts composed of metal and sulfur are now the alternatives for researchers due to their tunable and unique chemical structures, which can be synthesized through a green process.[121] This review categorizes MS-based catalysts into ten effective systems, including copper, cadmium, bismuth, indium, molybdenum, lead, tin, titanium, and zinc (Table 2). Subsequently, their electroreduction properties are also explored.

2.1 Copper-based sulfide

The copper sulfide system shows various stoichiometric structures over a wide range. Their structures varies from copper-rich to copper-deficient (Cu_2S to CuS_2), such as chalcocite Cu_2S, djurleite $Cu_{1.96}S$, digenite $Cu_{1.8}S$, anilite $Cu_{1.75}S$, geerite ($Cu_{1.6}S$), spionkopite ($Cu_{1.39}S$), yarrowite ($Cu_{1.12}S$), covellite CuS and villamaninite (CuS_2).[122–126] Owing to their variations in phase states, morphologies, and crystal structures, these copper sulfide systems have been used in many applications, including photocatalysis,[127] optoelectronic devices,[128] sensors,[129] batteries,[130] supercapacitors,[131] and many others. This section is designed to summarize several strategies of copper sulfide-based electrocatalysts in converting CO_2 into valuable products.

2.1.1 Substrate coupling. The deposition of a thin, nanometer layer of metal sulfide catalyst on top of a substrate material with well-defined morphological and electrical properties makes possible the optimization of the exposure of the active sites and the maximization of the electrochemical surface area (ECSA) of the resulting catalytic framework. This technique was widely used for electrocatalysis and was thoroughly discussed in comprehensive review works.[132,133] Coupling the catalyst layer with a conductive substrate with controlled morphology is specifically effective for metal sulfides. Indeed, despite their high intrinsic activity, these materials are usually synthesized by low-temperature routes to obtain mesoporous structures with suboptimal exposure of active sites. On the other hand, the coupling with conductive supports, drastically improves the ECSA as well as the conductivity of the architecture.[134–136] In this regard, Kahsay *et al.*[137] presented a unique and straightforward successive ionic layer adsorption reaction (SILAR) method to deposit CuS onto a thermally produced Cu_2O/CuO heterostructure. At low overpotential, the modified electrocatalyst showed good selectivity for formate production. Cu_2O/CuO/CuS electrode achieved a $FE_{Formate}$ of 84% with a partial current density (j_{Hcoo^-}) of -20 mA cm^{-2} at an overpotential of -0.7 V *vs.* RHE, which is higher as compared to metallic Cu nanowires ($FE_{CO} = 60\%$). Similarly, Li *et al.*[138] reported that highly porous Cu_2O/CuS nanocomposites (Fig. 2), which exhibit a $FE_{Formate}$ of 67.6% with a j_{HCOOH} value of 15.3 mA cm^{-2} at -0.5 V *vs.* RHE. More importantly, it maintained an average faradaic efficiency of 62.9% at the same applied potential for at least 30 hours. The synergistic effect between the Cu nanoparticles and S concentration reduced the activation energy barrier for conversion of the COOH* intermediates and enabled the CO_2 conversion at low potentials. That way, the rate of HCOOH generation was boosted. In above-mention both the cases the current density was much higher than that of the unsupported CuS electrocatalyst.

On the other hand, the coupling with conductive supports, usually carbon-based, drastically improves the electrochemical surface area as well as the conductivity of the framework. In this context, Oversteeg *et al.*[139] investigated the role of carbon-supported copper sulfide (CuS@C and Cu_2S@C) catalysts prepared *via* a liquid phase sulfidation of CuO@C nanoparticles (Fig. 3a–f). They did cyclic voltammetry and *in situ* X-ray absorption spectroscopy experiments, which revealed that CuS@C and Cu_2S@C nanoparticles undergo metallic Cu reduction during CO_2 electroreduction. Later, the group reported that compared to the CuO@C-derived catalyst, the selectivity towards the formate synthesis was increased at low current densities for the CuS@C- and Cu_2S@C- derived catalysts. Surprisingly, with less than 4% carbon surface coverage, the catalyst obtained a maximum of 12% FE for overall formate

Table 2 A state of the art summary of MS-based catalysts for ECO_2R

Electrode	Synthesis method	Potential	Electrolyte	Main products	Reactor	Current density (mA cm^{-2})	FE (%)	Stability	Ref.
Cu_2O/CuO/CuS	Successive ionic layer adsorption and reaction method (SILAR)	−0.7 V_{RHE}	0.1 M $KHCO_3$	HCOOH	H-cell	$j_{HCOO^-} = 20$	84	2.5 h	137
Cu_2S/Cu_2O	Hydrothermal method followed by electrochemical treatment	−0.9 V_{RHE}	0.1 M $KHCO_3$	HCOOH	H-cell	$j_{HCOO^-} = 12.3$	67.6	30 h	138
Cu_2S@C	Wetness impregnation method followed by drying and heat treatment	−0.78 ± 0.02 V_{RHE}	0.5 M KCl +0.5 M $KHCO_3$	HCOOH	H-cell	j_{total} =1.5	12	5 h	139
$Cu_{1.81}S$@MWCNT-600-OD	*In situ* crystallization strategy	−0.67 V_{RHE}	0.5 M $KHCO_3$	HCOOH	H-cell	$j_{total} = 3.75$	82	20 h	140
Submicron-sized Cu-S	Solvothermal method	−0.8 V_{RHE}	0.1 M $KHCO_3$	HCOOH	H-cell	$j_{total} = \sim 10$	80	12 h	145
Cu_xS	Dipping	−0.6 V_{RHE}	0.1 M $KHCO_3$	HCOOH	H-cell	$j_{HCOOH} = 2.5$	72	72 h	146
Cu_2S/Cu-foam	Electrodeposition method	−2.0 V (*vs.* Ag/Ag^+)	0.5 mol L^{-1} $BmimBF_4$	HCOOH	H-cell	$j_{HCOOH} = 5.3$	85	6 h	149
Hollow CuS microcubes	Galvanic replacement method	−0.16 V_{RHE}	0.5 M $KHCO_3$	CO	H-cell	—	32.7	10 h	150
CuS-thiourea precursors	Hydrothermal method	−0.51 V_{RHE}	0.1 M $KHCO_3$	CO	H-cell	—	72.67	5 h	151
CuS nanosheet arrays on Ni foam	Hydrothermal method	−1.1 V_{RHE}	0.1 M $KHCO_3$	CH_4	H-cell	$j_{total} = 7.32$	73.5 ± 5	60 h	152
CuS nanoflowers	Ethylene glycol solvothermal method	−0.8 V_{RHE} to −1.0 V_{RHE}	0.1 M $KHCO_3$	HCOOH	H-cell	$j_{formate} = \sim 6.5$	~52	2 h	153
CuS/BM coated with PTFE	Chemical bath deposition method	−0.7 V_{RHE}	0.5 mol L^{-1} $KHCO_3$	HCOOH	H-cell	$j_{formate} = 50$	70	1.5 h	154
MOF-derived hierarchical CuS hollow polyhedron	MOF self-sacrificial template method	−0.6 V_{RHE}	0.5 M K_2SO_4 aqueous solution	HCOOH	H-cell	$j_{formate} = \sim 16$	>90	36 h	155
Polycrystalline Cu nanoparticles (Cu-s)	Electrochemical reduction	−1.2 V_{RHE}	0.1 M $KHCO_3$	C_2H_4	H-cell	$j_{C_2H_4} = 40.8$	68.6	8 h	156
AC-CuS_x	Electrodeposition method	−0.9 V_{RHE}	0.1 M $KHCO_3$	HCOOH	H-cell	$j_{HCOO^-} = 9$	75	3 h	158
Sulfur-doped Cu_2O-derived Cu catalyst (Cu-5000S)	Electrodeposition followed by immersion	−0.8 V_{RHE}	0.1 M $KHCO_3$	HCOOH	H-cell	$j_{HCOO^-} = 13.9$	~75	12 h	159
Cu_2S nanocrystals	Electrochemically driven cation exchange method	−0.9 V_{RHE}	0.1 M $NaHCO_3$	HCOOH	H-cell	$j_{HCOO^-} = 19$	87.3	9 h	160
Bimetallic sulfide nanosheets (CA-nano-*x*)	Electrochemically driven cation exchange method	−0.2 V_{RHE}	0.05 M K_2CO_3	HCOOH	H-cell	—	~70	16 h	161
Cu_2S–Cu-V (V denoted as vacancy)	Solvothermal method followed by electrochemical reduction	−0.95 V_{RHE}	1.0 M KOH	Multi-carbon alcohols	Flow cell	$j_{multi\text{-}carbon\ alcohols} = 120$	32	16 h	165
Double sulfur vacancy-rich CuS	Electrochemical lithium tuning strategy	−1.05 V_{RHE}	0.1 M $KHCO_3$	*n*-propanol	H-cell	$j_{n\text{-}propanol} = 9.9$	15.4 ± 1	10 h	166
SnO_2 confined on CuS nanosheets	One-pot precipitation synthesis	−1.0 V_{RHE}	0.1 M $KHCO_3$	CO	H-cell	$j_{co} = 15.24$	>85	24 h	168
Heterostructure Bi-Cu_2S nanocrystals	One-pot solution-phase method	−1.0 V_{RHE}	0.1 M $KHCO_3$	HCOOH	H-cell	$j_{HCOO^-} = \sim 17$	>98	10 h	169

Table 2 (*Contd.*)

Electrode	Synthesis method	Potential	Electrolyte	Main products	Reactor	Current density (mA cm^{-2})	FE (%)	Stability	Ref.
$CuInS_2$ hollow nanostructures	Template-free method	−0.7 V_{RHE} & −1.0 V_{RHE}	0.1 M $KHCO_3$	HCOOH & CO	H-cell	$j_{total} = \sim 13$	72.8 & 82.3	4 h	170
Cu-S motif is dispersed in the framework of HKUST-1 (S-HKUST-1)	Hydrothermal method	−1.94 V_{RHE}	1.0 M KOH	C_2H_4	Flow cell	$J_{C_2H_4} = 228$	57.2	8 h	171
Porous Cd modified by sulfur	Liquid-phase synthesis strategy	−0.8 V_{RHE}	0.5 M $KHCO_3$	CO	H-cell	$j_{co} = 89.8$	88	10 h	183
Cadmium sulfide (CdS) nanoneedle arrays	Microwave heating strategy	−1.2 V_{RHE}	0.1 M $KHCO_3$	CO	Flow-cell	$j_{co} = 212$	95.5 ± 4.0	24 h	184
CdS_xSe_{1-x} nanorods	Solvothermal method	−1.2 V_{RHE}	0.1 M $KHCO_3$	CO	H-cell	$j_{co} = \sim 22$	81	10 h	185
CdS nanorods	Solvothermal method	−0.8 to −1.1 V_{RHE}	0.5 M $KHCO_3$	CO	H-cell	$j_{-0.9\ V(CO)} = \sim 1.3$	95	40 h	190
CdS surface with S vacancy	Solvothermal method	−1.1 V_{RHE}	0.5 M $KHCO_3$	CO	H-cell	$j_{co} = 20.5$	100 ± 0.5	10 h	191
Cadmium sulfide and carbon nanotubes composite catalyst (CdS-CNTs)	Solvothermal method	−1.2 V_{RHE}	0.1 M $KHCO_3$	CO	H-cell	$j_{total} = \sim 13$	~95	10 h	192
CdS/Ti_3C_2 MXene	Solvothermal method	−1.0 V_{RHE}	0.1 M $KHCO_3$	CO	H-cell	$j_{co} = \sim 6$	94	8 h	198
Ag_2S nanodots modified CdS nanorods	Co-solvothermal process	−1.1 V_{RHE}	0.5 M $KHCO_3$	CO	Flow-cell	$j_{co} = 10.6$	95	20 h	199
SD-$CuCd_2$	Co-precipitation method	−0.8 V_{RHE}	0.1 M $KHCO_3$	Ethanol	H-cell	$j_{co} = 0.6$	32	6 h	201
Ag-SnS_2	Polyol method	−0.1 V_{RHE}	0.5 M $KHCO_3$	HCOOH & CO/H_2	H-cell	$j_{formate} = 23.3$, $j_{CO/H_2} = 15.5$	60, 20.5	10 h	227
Atomically thin SnS_2 nanosheets with 5% Ni doping	Solvothermal method	−0.9 V_{RHE}	0.1 M $KHCO_3$	CO & HCOOH	H-cell	$j_{total} = 19.6$	93	8 h	228
Sulfur modulated tin catalysts (Sn(S)/Au)	Atomic layer deposition of SnS_x followed by a reduction process	−0.75 V_{RHE}	0.1 M $KHCO_3$	HCOOH	H-cell	$j_{HCOOH} = 51$	93.3	40 h	229
SnS/aminated-C	Modified hard template-induced method	−0.9 V_{RHE}	0.5 M $KHCO_3$	HCOOH	H-cell	$j_{HCOOH} = 41.1$	92.6	15 h	230
SnS_2/rGO	Hydrothermal method	−1.4 V_{RHE}	0.5 M $NaHCO_3$	HCOOH	H-cell	$j_{HCOOH} = 11.75$	84.5	2 h	231
SnS_2 monolayers	Li-intercalation/exfoliation method	−0.8 V_{RHE}	0.1 M $KHCO_3$	HCOOH	H-cell	$j_{total} = \sim 45$	94 ± 5	80 h	232
Nitrogen-enriched Sn(S) nanosheets	Nitrogen plasma engraving and topo-chemical electroreduction	−0.7 V_{RHE}	0.1 M $KHCO_3$	HCOOH	Flow-cell	$j_{total} = 25$	93.3	20 h	233
Stable semimetal 1H-SnS_2	Hydrogen-assisted low temperature calcination	−0.8 V_{RHE}	0.1 M $KHCO_3$	CO	H-cell	$j_{co} = 10.9$	98.2	15 h	234
S doped-Bi_2O_3-CNT	Solvothermal method	−0.9 V_{RHE}	0.5 M $KHCO_3$	HCOOH	H-cell	$j_{HCOOH} = 48.64$	97.06	10 h	244
Sulfur-derived Bi	Hydrothermal method	−0.75 V_{RHE}	0.5 M $NaHCO_3$	HCOOH	H-cell	$j_{total} = 5$	84	24 h	245
Bi_2S_3–Bi_2O_3@rGO	Partial precipitation conversion method	−0.9 V_{RHE}	0.1 M $KHCO_3$	HCOOH	H-cell	$j_{HCOOH} = \sim 3.8$	90	24 h	246

Table 2 (*Contd.*)

Electrode	Synthesis method	Potential	Electrolyte	Main products	Reactor	Current density (mA cm^{-2})	FE (%)	Stability	Ref.
Bi–Bi_2S_3	Solvothermal method	−1.0 V_{RHE}	0.1 M $KHCO_3$	HCOOH	H-cell	$j_{formate}$ = ~14	85	12 h	247
Sulfur-modulated bismuth sub carbonate nanosheets (S-BiOC)	Solvothermal method	−0.9 V_{RHE}	0.5 M $KHCO_3$	HCOOH	H-cell	$j_{formate}$ = 29	>90	20 h	249
Bulk MoS_2 with Mo-terminated edge	Chemical vapor deposition method	−0.764 V_{RHE}	4 mol% EMIM-BF_4 solution	CO	H-cell	j_{co} = 65	98	10 h	256
rGO-PEI-MoS_x	Drop casting followed by electrodeposition	−0.65 V_{RHE}	0.5 M $NaHCO_3$	CO	H-cell	j_{total} = 55	85.1	—	263
N-MoS_2@NCDs-180	Solvothermal method	−0.9 V_{RHE}	6 mol% EMIM-BF_4 solution	CO	H-cell	j_{CO/H_2} = 36.2	90.2	10 h	264
Cu-g-C_3N_4/MoS_2	Hydrothermal method	−0.67 V_{RHE}	0.5 M $KHCO_3$	CH_3OH	H-cell	$j_{methanol}$ = 78	19.7	30 h	265
Edge-exposed 2H MoS_2 N-Doped carbon hybridization	ZIF-assisted method	−0.7 V_{RHE}	4 mol% EMIM-BF_4 solution	CO	H-cell	j_{co} = 34.31	92.68	24 h	266
Cu/MoS_2	Microwave hydrothermal method	−1.4V_{SCE}	0.1 M $KHCO_3$	CH_4	H-cell	j_{CH_4} = ~3.2	17.08	48 h	267
5% Nb-doped on vertically oriented MoS_2	Chemical vapor deposition method	−0.8 V_{RHE}	50 vol% EMIM-BF_4	CO	H-cell	j_{total} = 237	80	—	268
Cu_2O nanoparticles decorated onto the MoS_2 nanosheets	Solution chemistry method	−1.3 V_{RHE} and −1.1 V_{RHE}	0.5 M $KHCO_3$	Methanol & ethanol	H-cell	j_{total} = 113	12.3 & 7.9	2 h	269
Hydrophobic exfoliated MoS_2 with decoration of fluorosilane	Ball milling method	−0.9 V_{RHE}	6 mol% EMIM-BF_4 solution	CO	H-cell	—	81	10 h	270
MoSeS alloy monolayers	Liquid–liquid interface-mediated strategy	−0.15 V_{RHE}	4 mol% EMIM-BF_4 solution	CO	H-cell	j_{CO/H_2} = 43	45.2	10 h	276
In nanoparticles on In_2S_3 nanosheets	Hydrothermal method	−1.0 V_{RHE}	1 M $KHCO_3$	HCOOH	H-cell	$j_{formate}$ = 40.3	76	8 h	282
Mn-doped In_2S_3 nanosheets	Modified thermal decomposition method	−0.9 V_{RHE}	0.1 M $KHCO_3$	HCOOH	H-cell	j_{total} = 20.1	90	8 h	283
$ZnIn_2S_4$	Hydrothermal method	−1.18 V_{RHE}	1 M $KHCO_3$	HCOOH	Flow cell	$j_{formate}$ = ~298	99.3	60 h	284
Flowerlike In_2S_3	Ionothermal method	−2.3 V_{RHE}	$BmimPF_6$/MeCN-H_2O solution	HCOOH & CO	H-cell	$j_{formate}$ = 25.6	86	10 h	285
Sulfur-doped indium	Hydrothermal followed bu electroreduction	−0.98 V_{RHE}	0.1 M $KHCO_3$	HCOOH	H-cell	j_{total} = 84	93	10 h	286
Wafer structured sulfur-derived Pb	Electroreduction	−1.08 V_{RHE}	0.1 M $KHCO_3$	HCOOH	H-cell	j_{HCOOH} = 12	88	—	288
PbS nanocrystals	Hot injection colloidal method	−1.2 V_{RHE}	0.1 M $KHCO_3$	HCOOH	H-cell	—	97.6 ± 5.3	10 h	289
ZnS/Zn	Sulfur infiltration method	−2.4 V_{Fc/Fc^+}	Propylene carbonate/						
$(CH_3CH_2CH_2CH_2)_4N(ClO_4)$	CO	H-cell	j_{CO/H_2} = 6.4	92	4 h	297			
S–Zn–S nanosheets	Chemical vapor decomposition	−0.8 V_{RHE}	0.1 M $KHCO_3$	CO	H-cell	j_{CO} = ~11	94.2	15 h	298

Table 2 (*Contd.*)

Electrode	Synthesis method	Potential	Electrolyte	Main products	Reactor	Current density (mA cm^{-2})	FE (%)	Stability	Ref.
ZnS/ZnO interface	Hydrothermal followed by centrifugation and sulfurization	−0.56 V_{RHE}	1 M KOH	CO	H-cell	$j_{CO} = \sim 109$	97.2 ± 0.5	40 h	299
Semi-metallic titanium disulfide (TiS_2)	Atomic layer deposition	−0.5 V_{RHE}	0.1 M NBu_4-PF_6	CO	H-cell	$j_{co} = 5$	83	16 h	302
Ni_2FeS_4 nanosheets	Microwave-assisted non-aqueous sol–gel method	−0.7 V_{RHE}	0.1 M $KHCO_3$	CO	H-cell	—	5.9	1 h	303
FeS_2/NiS nanocomposite	Hydrothermal method	−0.6 V_{RHE}	0.5 M $KHCO_3$	CH_3OH	H-cell	$j_{total} = 3.1$	64	4 h	304
Bulk Fe/Ni sulfides ($Fe_{4.5}Ni_{4.5}S_8$ pentlandite)	High-temperature synthesis	−1.80 V_{NHE}	0.1 M $TBAPF_6$	CO & methane	H-cell	$j_{total} = 3$	87 & 13	15 h	305
$Fe_3Ni_6S_8$	High-temperature synthesis	−1.80 V_{NHE}	0.1 M $TBAPF_6$/ acetonitrile solution	CO	H-cell	$j_{total} = 15$	3.6	8 h	306
$Fe_{4.5}Ni_{4.5}S_4Se_4$	Hot pressing method	−1.80 V_{NHE}	Acetonitrile	CO	H-cell	$j_{co} = 11$	84	2 h	307
Cu/Ag(S)	Electrochemical treatment	−1.0 V_{RHE}	0.1 M $KHCO_3$	CO and C_{2+} products	H-cell	$J_{ECO_2R} = 2.9$	93	1.5	308

Fig. 2 (a) Schematic illustration of the synthesis of Cu_2O/CuS nanocomposites. (b and c) SEM images of Cu_2O/CuS nanocomposites grown on a copper gauze collected at different magnifications. (d) HR-TEM image collected from a representative Cu_2O/CuS particle. (e) Corresponding FFT image of (d). Blue and yellow dashed lines highlight the diffraction rings of polycrystalline Cu_2O and CuS particles, respectively. (f–i) HAADF-TEM image of Cu_2O/CuS nanocomposites and the corresponding mapping images of elements O, Cu, and S (reprinted with permission from ref. 138. Copyright 2021, American Chemical Society).

selectivity. The use of sulfide-derived Cu with carbon catalysts can improve the efficiency of formate production in ECO_2R. Furthermore, the substrate/catalyst interaction can also improve the ECO_2R stability: Zhang *et al.*[140] synthesized multi-walled carbon nanotube (MWCNT) supported $Cu_{1.81}S$ catalyst through a simple two-step coupling strategy. The $Cu_{1.81}$-S@MWCNT-600 composite catalyst shown in Fig. 3g–j was accomplished with better ECO_2R performance with a 30 h stability upon continuous operation owing to the highly active sites of homogeneously dispersed $Cu_{1.81}S$ particles (Fig. 3i) and efficient electron transfer and active sites granted by MWNCT. Later, they reported that oxide-modification $Cu_{1.81}S$@MWCNT-600 ($Cu_{1.81}S$@MWCNT-600-OD) exhibited better catalytic activity with a high $FE_{Formate}$ of 82%. The authors attribute this enhancement in electrocatalytic activity belongs to copper oxide compounds which undergo restructuring in a needle-like morphology and offer more active sites during electrolysis.

2.1.2 Nanoscale engineering. Since the electronic structure of the catalyst can be optimised by acting on the atomic and molecular organization, extensive research effort has been devoted to fine-tuning the nanoscale structure of MS-based nanomaterials, and a number of reviews[141,142] have detailed the modifications induced on the electronic structure and, consequently, the positive effects of this technique on

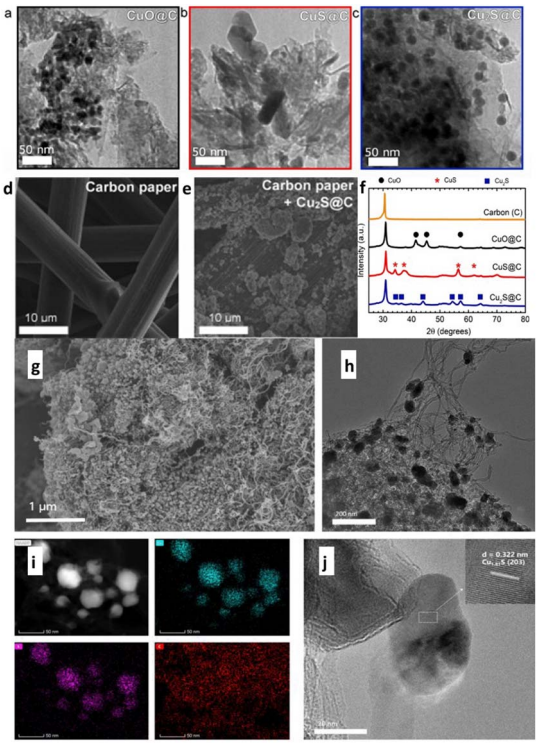

Fig. 3 TEM images of (a) CuO@C, (b) CuS@C and (c) Cu_2S@C nanoparticles and corresponding particle size histograms, indicating an average particle size of 9 ± 3 nm, 25 ± 13 nm and 17 ± 1 nm, respectively. SEM images of the carbon paper substrate (d) without any catalyst and (e) with Cu_2S@C deposited on the carbon fibers by spraying. (f) X-ray diffractograms of the bare GNP-500 carbon support (orange) and of the CuO@C (black), CuS@C (red) and Cu_2S@C (blue) nanoparticles on this carbon support. (Reprinted with permission from ref. 139. Copyright 2020, Elsevier); representative (g) SEM and (h) TEM micrographs of $Cu_{1.81}S$@MWCNT-600, (i) HAADF-STEM image and corresponding EDS maps revealing the uniform distribution of Cu (blue), S (purple) in the $Cu_{1.81}S$ particles, and (j) HRTEM of $Cu_{1.81}$-S@MWCNT-600 (reprinted with permission from ref. 140. Copyright 2021, Elsevier).

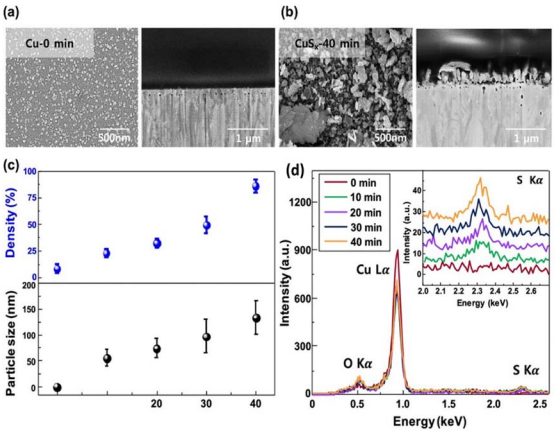

Fig. 4 Top-view and cross-sectional SEM images of (a) Cu-0 min without sulfur species and (b) CuS_x-40 min catalysts. (c) Average particle size and surface density of CuS_x NPs calculated by a computing-based image analyzer. (d) EDX spectra of Cu and CuS_x catalysts (reprinted with permission from ref. 146. Copyright 2020, American Chemical Society).

electrocatalysis. The nanoscale engineering strategy enhances both the ECSA by maximizing the surface area to volume ratio and the intrinsic activity of the material because nanoscale effects like quantum confinement or plasmonic resonance modify the electronic structure at this length scale.[143,144]

For example, Shinagawa *et al.*[145] synthesized size-controlled carbon-supported nanometric CuS catalysts using the wet chemistry method. The experimental study revealed that synthesized nanometric CuS was further reduced to S-modified copper (Cu-S) catalysts during ECO_2R. Therefore, S-modified copper (Cu-S) showed formate production (FE> 60%) with only trace amounts of CO at moderate overpotential (−0.8 V *vs.* RHE). They observed that HCOOH generation enhanced slightly as particle size increased from 3 nm to 20 nm, which highlights the correlation between particle size and catalytic effect. Later on, in the same work, it was also shown that the submicron-sized CuS electrodes prepared *via* solvothermal method exhibited much higher FE_{HCOOH} (80%) for electroreduction of CO_2 to HCOOH compared to the nanometric CuS electrodes (FE_{HCOOH} > 60%), revealing the crucial role of particle size in enhancing catalytic activity. On the other hand, Lim *et al.*[146] examined the efficiency and product selectivity of a size-controlled CuS_x catalyst prepared by dipping Cu foil in an industrial CO_2-containing H_2S in aqueous media. It was shown that the interaction between Cu foil and sulfur enhanced as the concentration of dissolved sulfur increased in an electrolyte (Fig. 4a and b). The simultaneous interaction increased the average particle size and surface sulfur density to 133.2 ± 33.1 nm and 86.2 ± 3.3%, respectively, for CuS_x nanoparticles (NPs) (Fig. 4c and d). The $FE_{Formate}$ was also enhanced from 22.7 to 72.0% at −0.6 V *vs.* RHE as the sulfur concentration and particle sizes of the CuS_x NPs increase gradually. Although the CuS_x catalysts showed less current density, the stability of 72 h must also be considered for converting industrial CO_2 to formate.

2.1.3 Morphology and structure modification. Modulating the morphology and structure of MS-based nanomaterials has always been a practical approach to optimizing catalytic performance and has achieved many outstanding research outcomes. By modulating the morphology and structure, the physicochemical properties of the promoter can be changed, thereby changing the catalytic activity and selectivity.[147,148] For example, it can effectively improve the active surface area of the catalyst, increase active sites for specific needs, generate novel and exciting physical phenomena, change the adsorption strength of the catalyst on the electrolyte or CO_2, *etc.*[70,72]

Furthermore, this approach can tailor the microenvironments near the catalyst surface for target products. A study by Zhu *et al.*[149] showed that the Cu_2S-modified Cu foam acts as an active electrocatalyst for CO_2 reduction in an H-cell setup. They deposited Cu_2S nanoarrays on Cu foam *via* a two-step anodization method followed by heat treatment. In the first step, anodization occurred in an electrochemical cell where Cu foam worked as an anode and platinum foil as the cathode in an

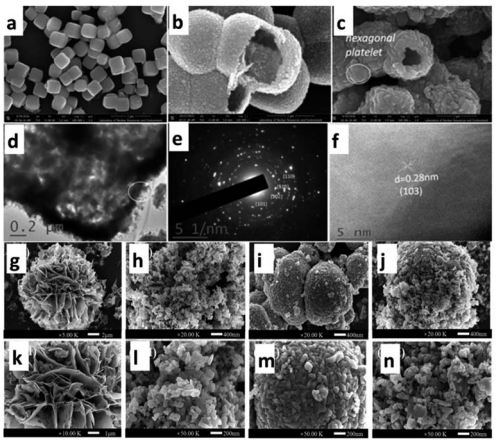

Fig. 5 SEM images of the samples (a–c): (a) Cu_2O MCs, (b) h-Cu_7S_4 MCs, (c) h-CuS MCs. (d) TEM image of h-CuS MCs. (e) SAED patterns of the white circled region in (d). (f) HRTEM image of the h-CuS MCs. (Reprinted with permission from ref. 150. Copyright 2017, Elsevier). SEM of the different CuS catalysts. (g and h) CuS-TU, (i and j) CuS-TAA, (k and l) CuS-STS, and (m and n) CuS-SS at a low magnification and high magnification (reprinted with permission from ref. 151. Copyright 2023, American Chemical Society).

aqueous Na_2S solution. In the second step, the anodized copper foam was rinsed with distilled water and thermally treated. The synthesized three-dimensional (3D) Cu_2S/Cu-foam electrode exhibits significantly better HCOOH production (85% of FEco with $j = 5.3$ mA cm^{-2} at -2.0 V *vs.* Ag/AgCl) than the Cu-foam electrode (maximum 38.9% of Feco at -1.8 V *vs.* Ag/AgCl). Shao *et al.*[150] reported CO_2 reduction over hollow CuS microcubes (MCs) electrodes (Fig. 5a–c) and reported less overpotential. It was shown from Fig. 5d–f that as-prepared h-CuS MCs led to a higher density of defective edge exposed sites and are considered a key in the improved performance and stable selectivity ($FE_{CO} = 32.7\%$ at a low onset potential -0.2 V *vs.* reversible hydrogen electrode). In 2023, Guo *et al.*[151] synthesized a series of CuS catalysts with various sulfur precursors *via* hydrothermal synthesis (Fig. 5g–n). Among all, CuS-thiourea exhibited superior ECO_2R activities compared to CuS-sodium thiosulfate, CuS-thioacetamide, and CuS-sodium sulfide CO_2-saturated 0.1 M $KHCO_3$ electrolyte, high CO selectivity of 72.67% @ -0.51 V *vs.* RHE. The fast S decomposition of the thiourea precursor resulted in a higher S^{2-} concentration for faster nucleation rate and subsequent growth of unique nanoflower-shaped CuS-thiourea catalyst for facilitated mass transfer and favorable ECO_2R kinetics (Fig. 5g and h).

Later on, Zhao *et al.*[152] successfully synthesized efficient and stable CuS nanosheet arrays supported on nickel foam (CuS@NF) substrate *via* a facile hydrothermal route for ECO_2R activity. The highly-dense CuS nanosheet is uniformly distributed on the Ni foam framework and forms a 3D hierarchical foam structure. The developed CuS@NF possessed highly open and porous structures with a thickness ranging from 20 to 25 nm. It was observed that modification with S species promotes CO_2 adsorption and produces $CO_2^{\bullet-}$ intermediate. Afterward, the $CO_2^{\bullet-}$ intermediate reacts with H^+ and e^- to generate the CH_4. As a result, the CuS@NF obtained excellent FE_{CH4} of 73.5% with a stability of 60 h for CH_4 production with a high overpotential of -1.1 V *vs.* RHE.

Chen and co-workers[153] prepared a series of differently structured copper sulfides using a simple ethylene glycol solvothermal process for ECO_2R to HCOOH. Then the group varied the morphology and composition of CuS nanoparticles by changing the Cu/S feed ratio and reaction temperature (Fig. 6a–f). Among all the synthesized Cu-rich nanoparticles, CuS nanoflowers exhibited the maximum ECO_2R performance with a significantly better FE_{HCOOH} of ~52%. Likewise, Dou *et al.*[154] prepared CuS nanosheet arrays decorated on the brass mesh (BM) using a facile and energy-saving one-step chemical bath deposition process (Fig. 6g and h). Meanwhile, coupling of CuS with BM enhanced a large total current density up to 75 mA cm^{-2} at -0.7 V *vs.* RHE with an FE of 67.8 ± 1% for $HCOO^-$ generation. But CuS/BM coated with PTFE obtained an FE of 70.2 ± 1% for HCOOH/$HCOO^-$ at -0.7 V *vs.* RHE. Systematic studies show that a significant enhancement in catalytic reactivity was achieved through the restructuring of CuS/BM during the reduction process, resulting in a highly dispersed nanowire network with many active sites. They combined DFT studies with experimental observations. According to the study, excellent selectivity for $HCOO^-$ generation was attributed to the reconstructed development of Cu (111)/CuS (102) facet during the reduction process. The theoretical study also indicates that S under the Cu^0 layer was found to reduce the binding energies of HCOO* and *COOH on Cu(111)/CuS(102) compared to the

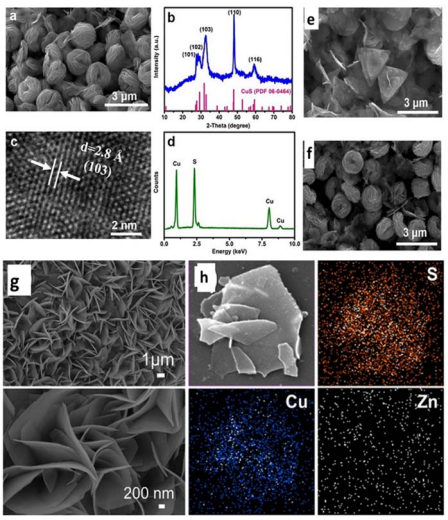

Fig. 6 (a) SEM image, (b) XRD pattern, (c) HR-TEM image, (d) EDX spectra of CuS nanoflowers synthesized at 150 °C with Cu/S feed ratio of 1/3. (e) SEM image of $Cu_{1.45}S$ nanoplates synthesized at 150 °C with Cu/S feed ratio of 1/0.75; (f) SEM image of $Cu_{1.54}S$ nanoflowers synthesized at 180 °C with Cu/S feed ratio of 1/3. (Reprinted with permission from ref. 140. Copyright 2020, Elsevier); (g) SEM image of CuS/BM. (h) EDS mapping result of the CuS nanosheet for S, Cu, and Zn elements (reprinted with permission from ref. 154. Copyright 2021, American Chemical Society).

Cu(111) plane, facilitating the production of HCOOH or HCOO*.

In 2021 Zhang *et al.*[155] reported that MOF-derived hierarchical CuS hollow polyhedron (CuS-HP) structures effectively enhance ECO_2R performance in neutral pH aqueous conditions. Their analysis showed that the CuS-HP is reduced into a sulfur-doped metallic Cu catalyst during catalysis. The durability of the *in situ* evolved catalyst observed a stable performance for 36 hours at a formate partial current density of 16 mA cm^{-2} at −0.6 V *vs.* RHE with a faradaic efficiency of >90%. According to theoretical research, S-doping in the metallic Cu (111) facet does not change the reaction pathways but decreases the activation energy barriers for formate generation while suppressing HER. These works provide a clear understanding of enhancing $HCOO^-$ selectivity mechanisms for CuS electrode materials. Similarly, He *et al.*[156] studied the catalytic behavior of $Cu_{2-x}S$ derived polycrystalline Cu (Cu-S) catalyst for CO_2 conversion to C_2H_4 formation. The nanostructured Cu-S catalysts exhibited better catalytic activity (FE of C_2H_4 was 68.6% and partial current density of 40.8 mA cm^{-2}) due to the high index facets during surface modification. *In situ* operando Raman techniques proved that the Cu-S catalysts follow the *COCHO pathway to produce C_2H_4 during the ECO_2R process.

The modifications in electronic structure triggered by the surface modification can be fine-tuned to control the selectivity of the material for the desired electrocatalytic application against the competitive HER, Phillips and their team investigated the formate selectivity over copper electrodes derived from copper sulfide by *in situ* electro-reduction.[157] The surface-enhanced infrared absorption spectroscopy (SEIRA) observed that the S-derived Cu catalyst suppresses H_2 and CO generation while increasing the formate generation. The authors explain this improvement of formate selectivity *via* a plausible reaction mechanism: the CO_{ads} tightly occupy some active catalytic sites, which interrupt the adsorbed hydrogen species (H_{ads}) to combine and create an H_2 molecule. Therefore, H_{ads} could only form H_2 in the solution phase by bonding protons *via* PCET. DFT calculations show that H_{ads} might react with a CO_2 molecule in the solution phase instead of a solution containing H^+ to produce HCOOH. Thus, H_{ads} intermediates adsorbed on S-derived Cu produced formic acid with solution-phase CO_2 through PCET.[157] In 2018, Deng *et al.*[158] compared ECO_2R activity for active CuS_x (AC-CuS_x), desulfurized CuS_x (DS-CuS_x), and bare Cu catalysts (Fig. 7a–c). The AC-CuS_x catalyst reported good selectivity and activity for formate synthesis (FE_{HCOO} = 75% and j_{HCOO} = 9.0 mA cm^{-2} at −0.9 V_{RHE}) compared to DS-CuS_x (FE of 29.3%) and bare Cu (FE of 22.5%). The DFT analysis confirms that sulfur concentration reduces the adsorption strengths of HCOO* and *COOH, with *COOH exhibiting less adsorption energy than HCOO* (Fig. 7d–i). According to the findings, the high surface coverage of *COOH intermediates occupies Cu sites surrounded by the sulfur atom, which thus interrupts electron transfer from those Cu sites to the intermediates (Fig. 7h and i). Therefore, the high amount of sulfur doping also weaker the adsorption of HCOO*, which resulted in energy downhill of the rate-limiting step for formate production and increased its formation (Fig. 7e and f). Huang and the

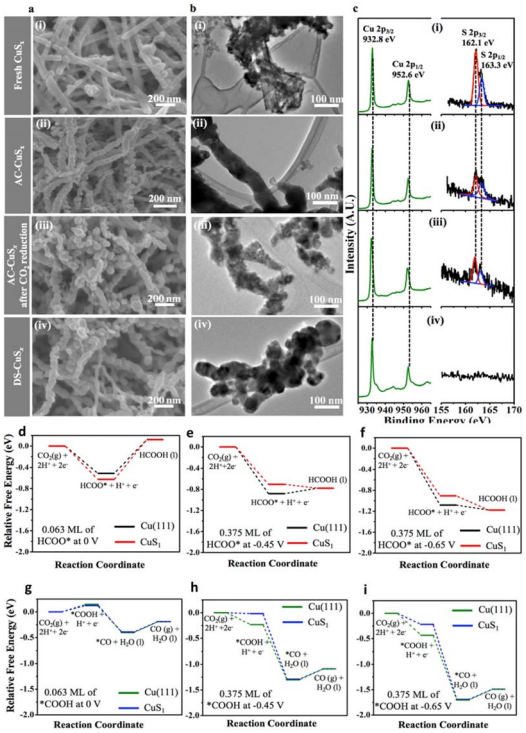

Fig. 7 (a) SEM images, (b) TEM images, and (c) XPS spectra of (i) fresh CuS_x sample, (ii) AC-CuS_x sample, (iii) AC-CuS_x samples after 40 min of CO_2 reduction in 0.1 M $KHCO_3$ at −0.85 V *vs.* RHE, and (iv) DS-CuS_x sample. Free energy diagrams of the HCOO* pathways to formate on Cu (111) and CuS_1 surfaces at (d) 0 V and 0.063 ML (monolayer) of HCOO*, (e) −0.45 V and 0.375 ML of HCOO*, and (f) −0.65 V and 0.375 ML of HCOO*. Free energy diagrams for *COOH pathways to CO on Cu (111) and CuS_1 surfaces at (g) 0 V and 0.063 ML of *COOH, (h) −0.45 V and 0.375 ML of *COOH, and (i) −0.65 V and 0.375 ML of *COOH (reprinted with permission from ref. 158. Copyright 2018, American Chemical Society).

group[159] prepared novel sulfur-doped Cu catalysts derived from Cu_2O to give CO_2 to HCOOH. The authors observed that optimizing sulfur concentration is crucial in activating HCOOH production. Their study claimed that electrocatalyst (Cu-5000S) containing 2.7 atom% sulfur exhibits higher catalytic activity and formate selectivity (FE = 75% and j = −13.9 mA cm^{-2} at −0.9 V *vs.* RHE). The mechanistic studies show that the sulfur-doped Cu lowers the binding strength of CO production intermediates COOH*, which facilitates the production of HCOOH.

A novel electrochemically driven cation-exchange (ED-CE) technique introduced as a powerful method to systematically tune and modify the composition, morphology, and phase structure of a target nanocrystal (NC) assembly by a precise replacement of metal cations in a predesigned NC template: He *et al.*[160] used ED-CE approach for obtaining highly active ECO_2R copper sulfide catalysts. This synthesis method converted 3D-shaped CoS_2 into Cu_2S with the novel 3-dimensional shape, although high grain boundaries were preserved (GBs), as illustrated in Fig. 8a. A ∼87% faradaic efficiency (at −1.9 V_{RHE} With a j = 19 mA cm^{-2}) for CO_2 conversion to HCOOH was reported with the Cu_2S nanocrystal electrode. Similarly, Jinghan Li *et al.*[161] incorporated ED-CE method that used copper sulfide as a growth

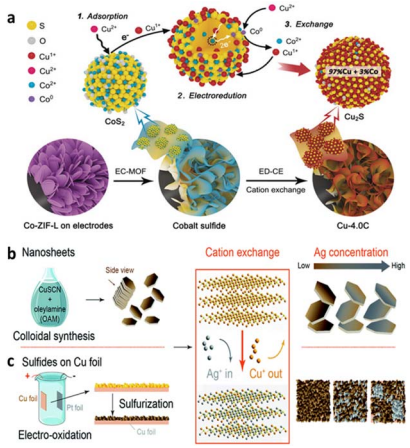

Fig. 8 (a) Schematic illustration of the experimental pathways and mechanisms for electrochemically driven cation exchange (ED-CE); synthetic strategies for Ag/Cu sulfide catalysts (reprinted with permission from ref. 160. Copyright 2020, John Wiley & Sons, Inc). (b) Cu sulfide nanosheets (C-nano-0, 100 nm lateral dimension, 14 nm thick) were obtained through colloidal synthesis with CuSCN in oleylamine (OAM). (c) Cu sulfides on Cu foil (C-foil-*x*) were obtained through electrooxidation in 1 M NaOH to produce an oxide layer of a few 10 s of microns thick, followed by sulfurization with 0.1 M Na_2S. After cation exchange where Ag^+ replaces the Cu^+ in the Cu sulfides, Ag/Cu sulfide nanosheets (CA-nano-*x*) remain nanosheet structure with some distortion in shape as the Ag/Cu mass ratio ranges from 0.3 to 25; while for C-foil-*x*, Ag nucleates at higher Ag concentration, that impedes the uniform distribution of Ag and Cu (reprinted with permission from ref. 161. Copyright 2021, The Royal Society of Chemistry).

template to synthesize Ag/Cu bimetallic catalysts for ECO_2R (Fig. 8b and c). They used $Cu_{2-x}S$ nanosheets (denoted as C-nano-0 with a lateral dimension of 100 nm and 14 nm thick) as a precursor. It was observed that during synthesis increasing Ag^+ concentration (by changing Ag/Cu mass ratio ranges from 0.3 to 25) in the exchange solution possesses a steady shift in crystal structures from Cu_7S_4 to Ag_2S (CA-nano-*x*, where *x* denotes higher Ag concentration). Therefore, both C-nano-0 and cation-exchanged nanosheets showed extremely good FE_{HCOOH} at a low overpotential (−0.2 V *vs.* RHE). Surprisingly, the Ag combination enhanced the generation of C_{2+} products at −1.0 V *vs.* RHE compared to C-nano-0, which mainly generates formate. In the next step, Cu sulfides to a depth of a few 10 s of microns were deposited using a two-step electrooxidation/sulfurization on Cu foil (C-foil-*x*). They observed that cation exchange creates evenly dispersed Ag at lower Ag^+ concentrations; however, at higher Ag^+ concentrations, Ag particles nucleate on the surface. Their findings show that the production of ethylene and methane initially increased with time for silver/copper sulfides on Cu foil (CA-foil-*x*-*y*). Later, it decreased as H_2 evolution occurred, and the catalyst's shape evolved towards a nest-like structure with a diameter of 20 nm, which could explain the change in selectivity. This result is due to the ED-CE process, which modified uncoordinated sites, crystal phase structure, composition, and density, enabling the construction of additional active sites for ECO_2R catalysis.

2.1.4 Defects engineering. Theoretical and experimental studies revealed the possibility of tuning the electronic structure by introducing defects (*i.e.*, chalcogen or distortion in the material's lattice). Introducing defects and distortion is the most investigated technique employed to activate the otherwise inert basal plane. The primary role of the vacancy sites has been comprehensively studied in the literature:[162–164] the missing chalcogen atom exposes the underlying metal surface, whose dangling bonds states of the d-orbital are responsible for the creation of the gap states near the Fermi level, with an energy reaching that of the Fermi level as the chalcogen vacancy percentage increases. These gap states can hybridize with the orbitals of the reactant, thus favoring their adsorption and improving the catalytic activity of the material.

A shift in selectivity can be obtained by employing S-vacancy metal sulfide-based catalysts, where CO_2 can be transformed into value-added C_{2+} products. Zhuang and colleagues[165] demonstrated that incorporating sulfur atoms in the catalyst core and copper vacancies in its shell present excellent ECO_2R activity. The bifunctional Cu_2S–Cu-V (V denotes vacancy) electrocatalyst consists of S atoms in the nanoparticle core and copper vacancies in the shell with high electron density. The Cu_2S–Cu-V catalyst exhibited excellent electrochemical activity by generating C_{2+} alcohols (*i.e.*, C_3H_7OH and CH_3CH_2OH) with a faradaic efficiency of 32% ± 1%. Compared to simple copper nanoparticles, the alcohol-to-ethylene ratio increased six times, suggesting an alternate path for alcohol production rather than alkenes. DFT simulations revealed that core–shell vacancy engineering increases the energy barrier of the C_2H_4 route (1.148 eV) but has no effect on the CH_3CH_2OH path (0.427 eV). Peng *et al.*[166] investigated the roles of double-sulfur vacancies (DSV) structure in ECO_2R. It was shown that the DSV in CuS_x enabled the stability of both CO* and a *C_2 dimer (*i.e.*, OCCO*), with a subsequent coupling with a third *CO through CO–OCCO, as depicted in Scheme 1. The DSV-rich CuS_x showed an enhanced $FE_{n\text{-PrOH}}$ of ∼15.4% for *n*-propanol generation at −1.05 V_{RHE} in 0.1 M $KHCO_3$ in the H-cell configuration.

2.1.5 Interfacial engineering. Interface engineering is an essential strategy for modulating electrocatalytic activity. Interfaces enable rapid charge transfer and modified free energies of intermediates due to the strong interfacial interactions between components.[167]

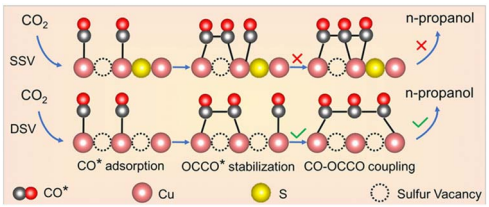

Scheme 1 Schematics of CuS_x with double sulfur vacancies for converting CO_2 to *n*-propanol, and the corresponding calculations. A Mechanism of *n*-propanol formation on adjacent CuS_x-DSV, showing the dimerization of CO–CO followed by CO–OCCO coupling (reprinted with permission from ref. 166. Copyright 2021, Nature Publishing Group).

Constructing bridging bonds at the interface to form strongly coupled hybrid catalysts can significantly increase the ECO_2R activity. For example, Wang *et al.*[168] synthesized novel hierarchical 0D/2D heterostructures of SnO_2 nanoparticles confined on CuS nanosheets (SnO_2/CuS NSs) for syngas production with a ratio tuned of 0.11–3.86 (CO/H_2). Their catalytic system was found to be highly selective for syngas production with a FE of >85%, a turnover frequency (TOF) value of 96.12 h^{-1}, and long-term stability of 24 hours. The authors explain this higher catalytic activity for two reasons: (a) the uniformly dispersed ultrasmall SnO_2 nanoparticles on ultrathin CuS nanosheets provide the highest number of active sites, which allow a faster rate of electron transfer; and (b) the distinct SnO_2 and CuS interfaces reduce the activation energy of reaction intermediates, thus improving ECO_2R activity to produce high-ratio tunable syngas. The DFT study revealed that individual SnO_2(110) and CuS(001) surfaces favored HCOOH generation, but in this case, SnO_2/CuS interface significantly reduced free energy of 0.52 eV for COOH* intermediate formation and promoted CO formation.

Modulating and understanding the intermediates that form on the surface of an electrocatalyst during ECO_2R is vital to overcome limitations associated with the adsorption of CO_2 molecules. Han *et al.*[169] constructed an intermetallic ternary Bi-Cu_2S heterostructure catalyst prepared by the one-pot solution-phase method. Owing to the strong chemical interaction effects between Bi and Cu_2S and its unique heterostructure, it attained a reduced overpotential (240 mV lower than Bi) and an exceptional FE (>98%) for formate generation with a high partial current density (2.4 and 5.2 times more $-J_{HCOO}$ than bare Cu_2S and Bi at 1.0 V_{RHE}). Mechanisms study demonstrated that the higher rate of electron transfer from Bi to Cu_2S at the interface preferentially stabilizes the *OCHO intermediates over *COOH and *H, which facilitates HCOOH formation. Similarly, Xiong *et al.*[170] synthesized bimetallic $CuInS_2$ hollow nanoparticles with a homogeneous mixing procedure. The combined benefits of the synergistic effect of the metal center and hollow nanostructures resulted in faster electron transfer. As a result, the bimetallic catalyst achieved a FE_{CO} of 82.3% at −1.0 $V_{RHE,}$ while FE_{HCOOH} was 72.8% at −0.7 V_{RHE}. *In situ* Raman spectroscopy revealed that CO_2 was activated to $CO_2^{\bullet-}$ intermediates, and electron redistribution occurred under differing potentials, resulting in a change in product distribution (CO to HCOOH). In addition, according to Nyquist plots, $CuInS_2$ hollow nanostructures have a significantly higher charge-transfer rate during the CO_2 reduction reaction because their interfacial charge-transfer impedance (R_{ct}) is lower than that of Cu_2In.

In another effort to modulate interfacial charge distribution and promote CO_2 adsorption, Wen and co-workers proposed a robust technique based on local sulfur doping of a Cu-based metal–organic framework precatalyst and stable Cu-S motif distributed throughout the HKUST-1 framework (denoted as S-HKUST-1). The regenerative catalysts matrix exhibits a high C_2 product (C_2H_4) selectivity of up to 57.2% at the operated current density of 400 mA cm^{-2}. For ECO_2R catalysis, this is the best selectivity and activity value for C_2H_4 among the Cu-based metal–organic species and MOFs. The operando XAFS investigation and systematic characterizations depicted that the Cu-S motif is stable during the process and stabilizes more active $Cu^{\delta+}$ species. The authors rationalize the excellent selectivity of S-HKUST-1 compared to copper or copper sulfide as follows: the approximate Cu^0–$Cu^{\delta+}$ distance was favorable for the *CO dimerization step at the Cu/Cu_2S interface. Moreover, an extremely high S-content catalyst (*i.e.*, Cu_2S) exhibited a long Cu–Cu distance, which hindered *CO dimerization geometrically; the Cu/Cu_2S interface offered lower binding energy to *CO species in rising to *CO dimerization than a pure metallic Cu catalyst.[171]

2.2 Cadmium (Cd)-based sulfide

Cadmium sulfide (CdS) is a low-cost II–VI group semiconductor material with a narrow bandgap energy of 2.42 eV. Because of its inexpensive cost, variety of polymorphs, and outstanding optical/electronic properties, it has been extensively explored for solar energy applications. The above-mentioned inherent characteristics of CdS make it suitable for photochemical and electrochemical water-splitting, photochemical CO_2 reduction, *etc.* Several strategies, such as heterojunction formation, co-catalyst loading, and heteroatom doping, are being reported.[172–174] Among all, doping heteroatoms in CdS have proven to be a very useful technique because it manipulates the intrinsic electronic structure and revises the Fermi energy level. It also unveils some impurity levels between the conduction band maximum and the valence band maximum, which are normally electron trapping centres.[175] For example, Ag material has been chosen for doping because it has excellent electrical and thermal conductivity and is also ideal for electrical applications.[176] In some recent studies, CdS is doped with two or more reactants as precursors, with the goal of overcoming the difficulty of modulating electronic configuration and nanostructures due to the multi-component reaction.[177,178] Some promising findings for CdS-based hybrids with various materials for various applications have been reported such as photocatalytic and electrocatalytic water splitting, photocatalytic CO_2 reduction, photoelectrochemical water splitting, and it is also used in solar cells.[179–181] This section will discuss current advancements in CdS-based electrocatalysts for CO_2 reduction in terms of their morphological structures, doping, vacancies, and electrode surface modification.

2.2.1 Morphology and structure modification. Apart from the inherent properties of electrocatalysts, the surface morphology also plays a crucial role in tailoring the efficiency of electrocatalytic CO_2 reduction. Since the superior accessibility of porous configuration with gas molecules, it is notably important to design porous electrocatalysts for the improvement of CO_2 adsorption and efficiency of ECO_2R.[182] Sulfur atoms attachment of an electrocatalyst to amorphous and porous Cadmium (Cd) support (P-CdlS) has been shown to selectivity shift from HCOOH to CO as demonstrated by Wu *et al.*[183] in which Cd^{2+} cations were tetrahedrally coordinated with S^{2-} anions *via* covalent orbital hybridizing s and p bands (Fig. 9a–g). They reported the DFT study, as shown in Fig. 9h–l. According to this finding, the hybridized sp band of CdlS

systems adsorbs CO_2 to generate *COOH intermediate, which accelerates CO formation.

Furthermore, Gao *et al.*[184] reported that a high-curvature CdS nanosized catalyst has a significant proximity effect that results in massive electric field amplification, which may concentrate alkali-metal cations. They synthesized a series of CdS nanoparticles (*i.e.*, nanoneedles, nanorods, and nanoparticles) with various tip radii by taking different reactant quantities using a microwave heating strategy (Fig. 10a–d). They detected that the tip-concentrated electric fields rise tenfold at −1.0 V as the tip stiffens from a radius of 24 nm to 3 nm (Fig. 10d and e). However, Gao *et al.* also found that the concentration of K^+ adsorbed on the surface of the CdS tip increased by 114-fold due to the highly concentrated electric field. The finite-element method simulations revealed that CdS needles in close proximity could further restrict electric fields that offer influence in K^+ concentrations. They also exhibited that gap width decreases with increasing K^+ concentration distribution because of the higher electric field inside the nanogap (Fig. 10f and g). Therefore, it is well established that K^+ ions interact with CO_2 through a non-covalent effect; that facilitates fast CO_2 stabilization at the CdS needle tips and nanogaps, where CO_2 reduction occurs. As a result, CdS nanoneedle exhibited excellent faradaic efficiency above 90% at −1.2 V_{RHE} with a current density of 212 mA cm^{-2}. Gao and his group conducted a 24 hours extreme stability test on CdS needles at 1.0 V_{RHE} in 0.1 M $KHCO_3$. Notably, the findings reveal a steady FE_{CO} of over 90% with a low current density decay. This work enables ECO_2R by creating a catalyst structure that adsorbs more electrolyte cations, stabilizing the intermediates.

Although H_2 is considered a "by-product" in the majority of cases of ECO_2R, and several strategies have been implemented to reduce the HER, its formation is not entirely meaningless. This is because H_2 and CO are the two main syngas components required in various industrial processes. He and co-workers[185] investigated a series of cadmium sulfoselenide (CdS_xSe_{1-x}) nanorods for the ECO_2R to syngas selectivity. The synthesized electrocatalyst enabled a broad range of syngas proportions and observed a higher current density above 10 mA cm^{-2}. In addition, CdS_xSe_{1-x} nanorods exhibited an 81% faradaic efficiency with a current density of 27.1 mA cm^{-2} for CO production. The experiment also showed that the faradaic efficiency for H_2 emission increases at −1.2 V_{RHE} when Se content increases in CdS_xSe_{1-x} nanorods. The mechanistic study revealed that the higher Se percentage in CdS_xSe_{1-x} nanorods improved H atoms binding to the catalyst surface and resulted in increasing H* surface coverage, subsequently enhancing HER in ECO_2R.

2.2.2 Defect engineering. The incorporation of defects (S-vacancy, S_v) in sulfide electrocatalysts can be a promising approach for tuning the adsorption energy of the key intermediates to improve the catalytic reaction kinetics.[186] Theoretical findings have confirmed that the surface S_v is crucial for the ECO_2R because of the appropriate binding energy of COOH to desorb the CO product further. Additionally, S_v can increase the

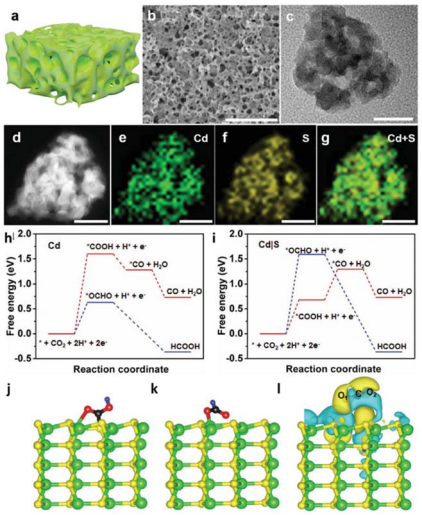

Fig. 9 (a) Schematic diagram of porous structure of P–Cd|S. The morphology of P–Cd|S characterized by (b) SEM, (c) TEM, and (d–g) HADDF-STEM. Scale bars are (b) 500 nm and (c–g) 100 nm. Gibbs free energy diagrams of (h) Cd metal, (i) sulfur-modified Cd. Optimized adsorption configuration of (j) *COOH and (k) *OCHO intermediates. (l) Differential charge density of CO_2 adsorbed on Cd|S, regions of yellow and cyan denote electron accumulation and depletion, respectively. Green, yellow, black, red, and blue balls represent Cd, S, C, O, and H atoms, respectively (reprinted with permission from ref. 183. Copyright 2020, John Wiley & Sons, Inc).

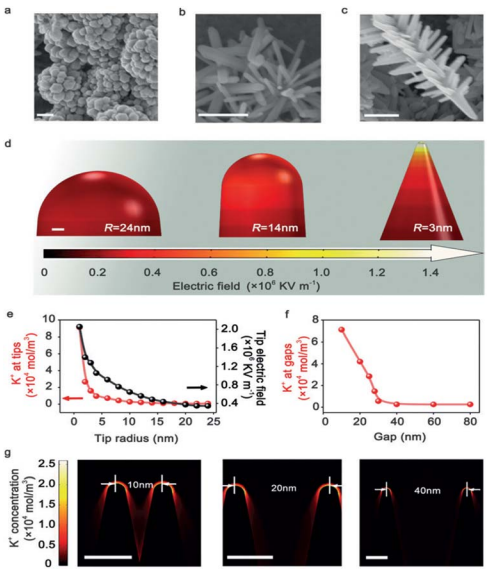

Fig. 10 (a)–(c) SEM images of CdS particles (a) rods (b) and needles (c). Scale bars, 400 nm. (d) Electric field on the surface of different catalysts is shown as a color map. The tip radius of the structure in each panel is 24 nm (left), 14 nm (middle), and 3 nm (right). Scale bar, 5 nm. (e) Adsorbed K^+ and the electric field intensity at the tip, revealing that both adsorbed K^+ and electrostatic field intensity increase as the tip radius decreases. (f) K^+ concentration intensity in the CdS needle gap increases as the gap distance decreases. (g) K^+ concentration distribution in the needle gap, showing enhanced K^+ concentration in the narrow gap. Scale bars from left to right: 10 nm, 10 nm, and 15 nm (reprinted with permission from ref. 184. Copyright 2020, John Wiley & Sons, Inc).

carrier concentration, enhancing charge transfer during the ECO_2R.[187–189] However, quantitative and continuous engineering of S_v content in CdS nanorods for CO_2 reduction has only received sporadic attention. More research is needed to gain a better understanding of the surface S_v contents and their effects on electrocatalytic properties.

Li *et al.*[190] developed simple cadmium sulfide (CdS) nanorods for ECO_2R to CO. The presence of (0002) surface with S_v in CdS nanorod increases the performance (95% FE with j_{CO} of −10 mA cm^{-2} at an overpotential of −0.55 V_{RHE}) and selectivity toward CO formation. Elsewhere, bulk CdS particles with size in micron level exhibited 60% selectivity for CO production in 0.5 M $KHCO_3$ at a potential of −0.9 V_{RHE}. The absence of (0002) face in CdS nanorods decreases the performance and selectivity toward CO formation. An ECO_2R to CO with low overpotential utilizing the cadmium sulfide (Cds) catalyst with S_V was studied by Li *et al.*[191] They observed that CdS nanorods were mainly exposed to the (002) face with sulfur vacancies, suppressing HER while increasing CO selectivity. Theoretical work confirmed that the (002) plane with a medium concentration of S_V showed better catalytic activity than without S_V due to the higher binding energy of *COOH intermediates. They also identified that CdS nanorods with a medium (9%) surface S_V resulted in better faradaic efficiency and catalytic activity. Qin *et al.*[192] reported the CO_2 electrochemical reduction for cadmium sulfide-supported carbon nanotubes composite catalyst (CdS-CNTs) (Fig. 11a–j) synthesized by a simple solvothermal approach. The composite material produced CO with a FE of more than 95%. Subsequently, the group explored the surface electron density of cadmium sulfide with S_V and the energy required for CO formation (Fig. 11k–s). The *in situ* infrared absorption spectroscopy with attenuated total reflection mode (ATR-IRAS) was used to evaluate the intermediate species formed during the process in order to detect the surface reaction on CdS-CNTs (Fig. 11k–n). As illustrated in Fig. 11m, it was observed that CO_2 adsorption above the CdS-CNTs surface increases after the electrode is electrified. Next, the area around Cd exhibits less blue in the presence of S_V than in the Cd without S_V, which signifies that the negative charge is partially transferred to Cd when S_V are created (Fig. 11o and p). DFT calculation proposed that S_V in CdS(111) increase the electron density on the catalyst surface and lower the energy required for COOH* to CO* conversion, facilitating the electro-reduction of CO_2 to CO (Fig. 11q–s).

In recent years, a new 2D material, MXene, emerged comprising transition metal carbides, nitrides, and carbonitrides.[193,194] These breakthrough materials are developed from three-dimensional (3D) ternary ceramic material MAX (M = transition metal, A is an A-group which is typically IIIA and IVA, or groups 13 and 14 components in the periodic table, and X is carbon/or nitrogen). MXene-based sulfides materials have been widely used as a substrate to prepare electrocatalysts for HER, nitrogen reduction reaction, oxygen reduction, or evolution reaction (ORR/OER) due to their 2-D structure, hydrophilic nature, excellent electrical conductivity, and richness of surface functional groups.[195–197] In 2021, Wang *et al.*[198] adopted a simple solvothermal approach to design a series of CdS and Ti_3C_2 MXene composites followed by H_2/Ar treatment, as shown in Fig. 12a. Uniform hierarchical structures of CdS nanoparticles with abundant sulfur vacancies dispersed in the Ti_3C_2 MXene matrix were observed by the SEM, HRTEM, and TEM (Fig. 12b, e, f and g). DES elemental mappings and XRD analysis confirmed the presence of the Cd, S-vacancies (V_S), Ti, and C (Fig. 12c and d). The 2D MXene skeleton structure accelerates electrolyte absorption, enables rapid electron transport, and increases electrochemical surface area. Because of these advantages, *i.e.*, high catalytic activity and electrical conductivity, V_S-CdS/Ti_3C_2 has faster CO_2 electroreduction reaction kinetics and achieved a FE_{CO} as high as 94% at −1.0 V *vs.* RHE (Fig. 12h–k). The group suggested that the HER activity of the composite materials can be regulated by regulating the surface exposed Ti element concentration. This study builds the foundation for developing MXene-based composite electrocatalysts for ECO_2R in aqueous solutions.

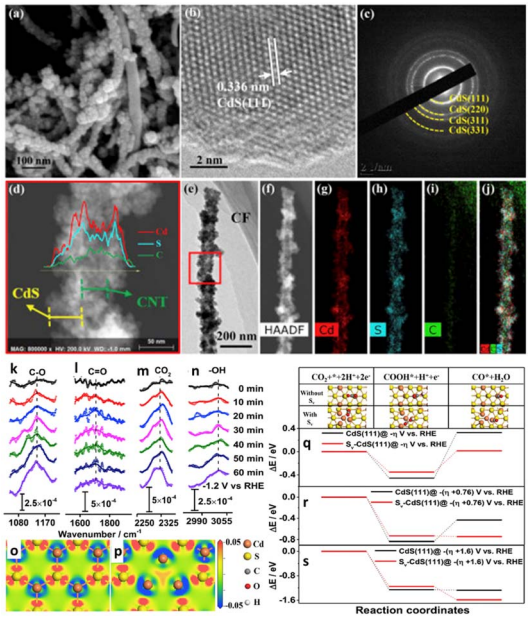

Fig. 11 (a) FESEM image of CdS-CNTs; HRTEM images of CdS-CNTs: (b) interplanar lattice fringe spacing, (c) SAED pattern, (d) line scan, (e) HRTEM image, (f–j) HAADF-STEM and element mapping; (k–n) *In situ* ATR-IRAS analyses of CdS-CNTs for ECO_2R. The distribution of electron deformation density: (o) CdS(111) without S-vacancy and (p) CdS(111) with S-vacancy. (q–s) DFT calculation results of relative energy for possible intermediates during CO2RR on CdS(111) without S-vacancy and CdS(111) with S vacancy (S_v) at different potentials (reprinted with permission from ref. 192. Copyright 2019, Elsevier).

2.2.3 Interfacial engineering. Constructing metal sulfide/metal sulfide heterojunctions is an effective strategy to create interfaces in MS-based electrocatalysts. For instance, combining Ag_2S nanodots with CdS nanorods showed excellent electrical conductivity and chemical stability during ECO_2R. Compared to separately synthesized bare CdS (j = 9.5 mA cm^{-2}) and Ag_2S (j = 5.5 mA cm^{-2}), Ag_2S/CdS electrocatalyst showed a higher partial current density of 10.6 mA cm^{-2} at −1.1 V *vs.* RHE for CO selectivity. They exhibited higher faradaic efficiency of 97% with a current density range of 80 to 200 mA cm^{-2} for

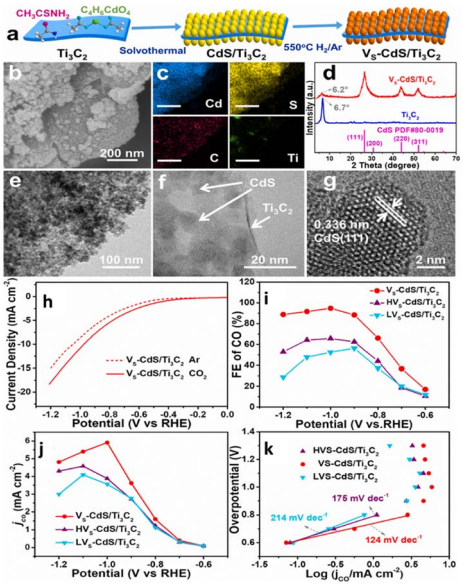

Fig. 12 (a) Schematic illustration for the preparation of V_S-CdS/Ti_3C_2. (b) SEM image and (c) DES elemental mapping images (scale bar, 5 μm) of V_S-CdS/Ti_3C_2. (d) XRD patterns of CdS, Ti_3C_2 and V_S-CdS/Ti_3C_2. (e and f) TEM and (g) HRTEM images of V_S-CdS/Ti_3C_2. (h) LSV curves of V_S-CdS/Ti_3C_2 in CO_2 (solid line) and Ar (dash line) saturated 0.1 M $KHCO_3$ aqueous solution. (i) FE for CO, (j) partial current density (CO) and (k) Tafel plots of LV_S-CdS/Ti_3C_2, V_S-CdS/Ti_3C_2 and HV_S-CdS/Ti_3C_2 (reprinted with permission from ref. 198. Copyright 2021, Elsevier).

formate and CO production when ECO_2R was employed in a flow cell. Compared to other loadings (2 wt%, 8 wt%, 10 wt%), the CO_2 reduction activity was found best at 5 wt% Ag_2S loading on the surface of the CdS nanorods.[199]

Designing catalysts with multiple active sites for synergistic CO_2 adsorption and activation of key intermediates, can significantly accelerate multicarbon chemicals (mainly ethanol) generation and inhibit the undesired HER. As reported, the conversion of ECO_2R to ethanol needs C–C coupling, which may be accomplished by fulfilling two conditions: first, sufficient carbon species at the catalyst surface for the coupling stage; second, stabilization of C_2 intermediates across the catalyst surface for the further reduction process.[200] In this context, Mosali *et al.*[201] prepared sulfide-derived copper-cadmium catalysts SD-Cu_xCd_y where x and y denote Cu to Cd molar ratio to facilitate the formation of crucial intermediates. The SD-$CuCd_2$ catalyst achieved a FE of ethanol production of ~32% at a low overpotential of 0.89 V_{RHE} in 0.1 M $KHCO_3$ solution. They found ethanol was the only formed C_2 product at low reduction potentials with the best-performed SD-$CuCd_2$ catalyst containing Cu_3Cd_{10} alloy/Cu_2S/CdS phase boundaries. The reaction mechanism is also described in detail, as shown in Scheme 2.

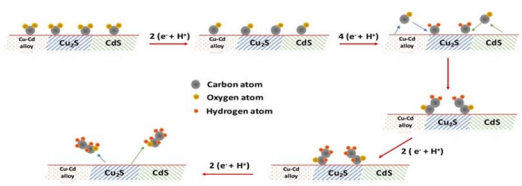

Scheme 2 Proposed mechanism for the formation of CH_3CH_2OH at SD-$CuCd_2$ catalyst – Cu–Cd alloy/Cu_2S/CdS phase boundaries (reprinted with permission from ref. 201. Copyright 2021, John Wiley & Sons, Inc).

2.3 Tin (Sn)-based sulfide

Tin sulfides are composed of many binary compounds, including SnS, Sn_2S_3, Sn_3S_4, Sn_4S_5, and SnS_2.[202,203] Among these compounds, SnS and SnS_2 are the most important and have attracted the greater interest of researchers due to their remarkable features and potential uses in energy storage systems.[204–208] Meanwhile, numerous SnS nanostructured with various morphologies, including nanoparticles,[209] nanorods,[210,211] nanoneedles,[212] rectangular nanosheets,[213] nanoflowers,[214] and core–shell nanospheres[215] have gained considerable interest for energy applications. Similarly, several SnS_2 nanomaterials, such as ultralong nanobelts,[216] hexagonal nanoplates,[217–220] nanosheets,[221] and 3D-hierarchical spheres/flowers modified by nanoplates/nanosheets[222–224] have been exhibited as high electrocatalytic activity. In this section, with a focus on Sn-based sulfides, we present the most popular design strategies for these materials with the goal of enhancing their ECO_2R catalytic performance by changing the structural and electrical properties at various length scales.

2.3.1 Heteroatom doping. Heteroatom doping can also be used to improve the electronic structure of electrocatalytic materials and tune CO_2 adsorption.[225] This process changes the material's electronic structure, altering the interaction strength between reactants and active sites and influencing electronic transport near active sites, which improves catalytic activity.[226] He *et al.*[227] designed and developed a hybrid bimetallic composite catalyst of Ag nanowire and defective SnS_2 nanosheets for CO_2 reduction, as shown in Fig. 13a–c. Moreover, it was found that free electrons present in Ag nanowires enhance the electron mobility in SnS_2 nanosheets, which improves the carrier density of Ag-SnS_2 hybrid nanosheets. Thus, the incorporation of Ag in defective SnS_2 catalyst exhibited a maximum faradaic efficiency of 83.8% (FE_{HCOOH} of 65.5%) for producing carbonaceous products. Zeng *et al.*[228] developed a scheme of element-doping engineering for synthesized ultrathin SnS_2 nanosheets with Ni atoms (Fig. 13d–f). These SnS_2 thin nanosheets effectively reduced CO_2 to formate with a greater current density and faradaic efficiency (FE) than pure SnS_2 nanosheets. A mechanistic analysis found that Ni doping caused a defect level and decreased the work function of SnS_2 nanosheets, resulting in increased CO_2 activation and hence better CO_2 electro-reduction performance. Likewise, in the ECO_2R application, Sargent *et al.*[229] fabricated Sulfur modulated tin (Sn(S)) deposited on Au needles (Sn(S)/Au) catalyst by a simple SnS_x atomic layer deposition (ALD) approach. The composite catalyst Sn(S)/Au observed a higher oxidation state than Sn nanoparticles and achieved a current density of 55 mA cm^{-2} with a FE_{HCOOH} of 93% for CO_2 electro-reduction. Fig. 13g–j shows that a small amount of S-doping (0–25%) into Sn could effectively reduce the Gibbs free energy (ΔG); in contrast, a more

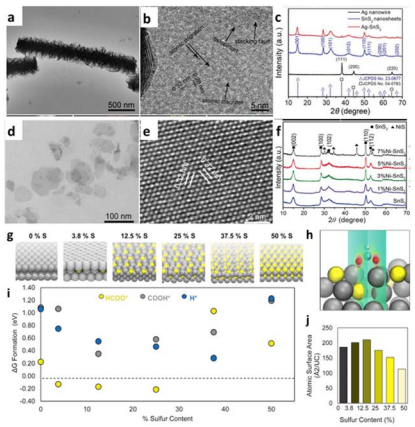

Fig. 13 (a) TEM image (b) HRTEM image and (c) XRD analysis of Ag-SnS_2 hybrid nanosheets (reprinted with permission from ref. 227. Copyright 2019, John Wiley & Sons, Inc); (d) TEM image (e) HRTEM image (f) XRD analysis of 5% Ni-SnS_2 nanosheets. (Reprinted with permission from ref. 228. Copyright 2019, John Wiley & Sons, Inc); computational investigation of (Sn(S)/Au) system (g) optimized surface slab structures of pure Sn, S-modulated Sn, and SnS. (h) Gibbs free energies of formation (DGformation) for HCOO* (yellow), COOH* (gray), and H* (blue) intermediates, which are the rate-limiting intermediates along the reaction pathway to produce formate, carbon monoxide, and hydrogen gas, respectively. (i) Volume slice of the charge densities through the middle of the oxygen atom of a bound HCOO* intermediate. (j) Atomic accessible surface area of the metal slab normalized to the number of tin atoms as a function of sulfur content (reprinted with permission from ref. 229. Copyright 2017, Elsevier).

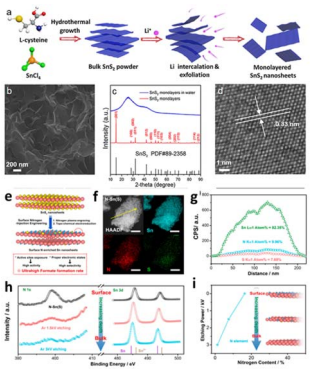

Fig. 14 Characterizations of SnS_2 monolayers. (a) Process used to synthesize; (b) SEM image; (c) XRD patterns of SnS_2 monolayers in the forms of powder and water dispersion; (d) HRTEM image; (reprinted with permission from ref. 232. Copyright 2018, Elsevier). (e) Illustration of synthesis from SnS_2 to N-Sn(S) nanosheets. (f) EDS mapping and (g) line scan of N-Sn(S) nanosheets. The scale bar is 30 nm. (h) *In situ* soft X-ray photoemission spectroscopy characterization of N, Sn elements in N-Sn(S). (i) The nitrogen content of different depth in N-Sn(S) nanosheets. (Reprinted with permission from ref. 233. Copyright 2020, American Chemical Society).

significant amount (25–50%) of S-doping into Sn can effectively increase the ΔG (Fig. 13i). The DFT simulations showed that the formation of HCOOH compared to CO was favored by Sn nanoparticles, both with and without sulfur doping.

2.3.2 Substrate coupling. As described in Section 2.1.1, coupling the electrocatalyst layer with a conductive support with controlled mesoscale morphology is particularly effective: recently, unprecedented selectivity for formate production (FE of 92.6%) was achieved at a moderate overpotential of −0.9 V *vs.* RHE using modified hollow nanotubes composed of SnS nanosheets with amino-functionalized carbon layers (SnS/aminated-C). The DFT theoretical calculation reveals high activity for formate production due to the synergistic effect of SnS and aminated-C, which enhances the electron transfer rate and higher the adsorption energies of OCHO* and CO_2* intermediates. They reported a density of states (DOS) calculation. According to the analysis, after adsorbing OCHO* on the SnS/aminated-C surface, it exhibits the highest peak of total DOS, which is close to the Fermi level than SnS, thus leading to a higher binding strength between SnS/aminated-C to OCHO*.[230] Zhang and co-workers synthesized SnS_2 nanosheets well dispersed on reduced graphene oxide (SnS_2/rGO) composite by a one-pot hydrothermal method and employed as a heterogeneous catalyst for ECO_2 R. The catalyst exhibited high formate selectivity with a faradaic efficiency of 84.5% at −0.68 V (*vs.* RHE). They found that rGO, along with SnS_2, stabilizes the intermediate ($CO_2^{\bullet-}$) during the reduction process and improves the catalyst's stability.[231]

2.3.3 Morphology and structure modulation. Liu and co-workers synthesized SnS_2 monolayers (thickness of 0.58 ± 0.04 nm) using a simple Li-intercalation/exfoliation method (Fig. 14a). In the case of SnS_2 monolayers, an interplanar spacing of 0.33 nm, corresponding to the (1 0 0) plane of SnS_2 is observed through HRTEM images (Fig. 14b–d). This electrocatalyst presented more than 90% FE for formate production with stability up to 80 h. Later, the theoretical analysis demonstrated that the thin atomic layers faster the crucial first step ($CO_2^{\bullet-}$ radical formation) in producing HCOO* intermediates, followed by proton–electron transfer processes resulting in formate production.[232] Similarly, Cheng *et al.*[233] enhanced the number of active sites, morphology and modified electronic structures of SnS_2 by surface nitrogen injection engineering (Fig. 14e). The derived surface nitrogen-enriched Sn(S) nanosheets, as shown in Fig. 14f–i provided better faradaic efficiency for formate production than SnS_2-derived Sn nanosheets. DFT simulation confirmed that the better catalytic performance is due to the Sn site valence modulation. Their findings showed that the surface nitrogen-injection engineering techniques enhanced the ECO_2R activity for other metal sulfides, such as CuS and In_2S_3.

2.3.4 Polymorph engineering. Polymorph engineering of SnS_2 is a practical approach to inhibit HER kinetics from achieving high ECO_2R performance and selectivity. To suppress the high HER activity of the metallic phase of 1H-SnS_2, Xu *et al.*[234] used a facile hydrogen-assisted low-temperature calcination technique to produce the meta-stable phase of the SnS_2 (1H-SnS_2) catalyst. They compared the ECO_2R activity between the stable semiconductor phase of SnS_2 (1T-SnS_2) and the meta-stable semimetal phase (1H-SnS_2). The novel nanosheets semimetal 1H-SnS_2 have an outstanding performance with a FE_{CO} of more than 98% at −0.8 V_{RHE} (partial j_{CO} of 10.9 mA

cm^{-2}). Theoretical studies revealed that the more robust electron exchange between *COOH intermediate and 1H-SnS_2 surface promotes CO formation.

2.4 Bismuth (Bi)-based sulfide

Bismuth sulfide (mineral bismuthinite) is a non-toxic and crystalline n-type V–VI group semiconductor material with a lamellar structure connected by weak Bi–S bonds.[235] It has a band gap energy value of 1.3 eV,[236] which is moderate but relatively higher than other sulfides in the similar group of metal chalcogenides of the type $A_2^{V}B_3^{VI}$ (A = Sb, Bi, As; B = S, Se, Te).[237] With such extraordinary properties, Bismuth sulfide is widely used in different applications such as solar cells,[238] sodium-ion batteries,[239] supercapacitors,[240] thermoelectric materials,[241] photoanode,[242] and so on.[243] This section will focus on bismuth sulfide-based electrocatalysts in their defect sites, interfacial phenomena, and morphological structure for CO_2 reduction application.

2.4.1 Substrate coupling. As identified in Section 2.1.1, coupling with conductive supports, generally carbon-based, improves both the electrochemical surface area and the conductivity of the catalytic framework: Liu *et al.*[244] prepared composites electrocatalyst S-doped Bi_2O_3 nanosheets (NSs) coupled with carbon nanotubes (S-Bi_2O_3-CNT) for improved catalytic activity towards CO_2 to HCOOH production (Fig. 15a–g). According to Fig. 15h and i, the HCOOH pathway is more energy-favorable than the CO pathway because the Gibbs free energy (G) for the production of *COOH (the intermediate for the CO pathway) is higher than that of *HCOO (the intermediate for the HCOOH pathway). DFT calculations indicate that less electronegative S doping was attributed to higher charge density distribution and electronic delocalization of Bi (Fig. 15j and k), which increased the adsorption of $*CO_2$ and *HCOO intermediates while preventing *H adsorption. As a result, S-Bi_2O_3 enhances formate production while suppressing HER.

2.4.2 Defect engineering. Bismuth sulfide is another potential metal sulfide-based electrocatalyst, which can be used as a suitable catalyst for ECO_2R by constructing lattice defects: Zhang *et al.*[245] showed that lattice defects in Bi-based catalysts strongly influenced formate production in ECO_2R. They observed that sulfur-derived Bi (SD-Bi) was exposed to more lattice defects owing to the release of lattice sulfur during the catalysis. Sulfur-derived Bi with structural lattice defects achieved high faradaic efficiency (maximum 84.0% at a potential of −0.75 V with a stability of 24 h), which has the best performance compared to the high crystalline SD-Bi catalysts under similar conditions. The authors also reported that though the selectivity of lattice defect-rich Bi derived from Bi_2S_3 was high, the catalytic current density needs to be enhanced.

In another work, Yang *et al.*[246] studied the role of defects and specific interfacial phenomena between bismuth oxide and bismuth sulfide (Bi_2S_3–Bi_2O_3). They used the partial precipitation conversion method to create many defects, including oxygen vacancies and lattice distortions. The hybrid catalysts Bi_2S_3–Bi_2O_3/rGO achieved unprecedented selectivity of over 90% for formate production with a stability of more than 24 h.

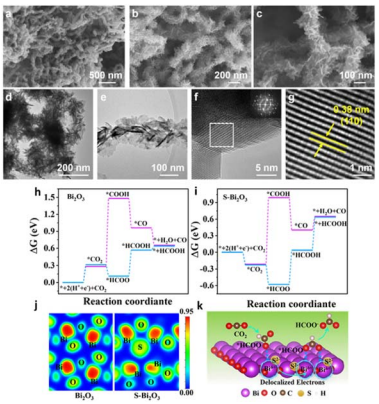

Fig. 15 (a–c) Field emission scanning electron microscopy (FESEM) images of S_2-Bi_2O_3-CNT with different magnifications. (d–g) TEM images of S_2-Bi_2O_3-CNT with different magnifications. Gibbs free energy diagrams for ECO_2R to CO and HCOOH on (h) Bi_2O_3 (110) and (i) S–Bi_2O_3 (110) surface. (j) Charge density distribution of Bi_2O_3 and S–Bi_2O_3. (k) Schematic illustration for the role of S in promoting the reduction of CO_2 to formate (reprinted with permission from ref. 244. Copyright 2021, American Chemical Society).

Mechanistic studies also reveal that the Bi_2S_3–Bi_2O_3 interface provides rich-defect sites as well as oxygen vacancies, thus offering more active sites that lowered the binding energy of the HCOO* intermediates, and the HCOOH product selectivity improved.

2.4.3 Interfacial engineering. A metal–semiconductor junction can modulate both the band positions of the semiconductor and the d-band center of the surface-active atoms. It thus helps to lower the activation barrier of CO_2 and suppress the competitive HER and hence improve the faradaic efficiency. In this regard, Shao *et al.*[247] successfully prepared a series of Bi–Bi_2S_3 by a facile one-pot solvothermal synthesis method. The High-resolution TEM (HRTEM) analysis of Bi–Bi_2S_3 revealed the visible lattice fringes of 0.36 nm and 0.3 nm, confirming to Bi_2S_3 (221) and Bi (012) planes, respectively. Dark-field TEM images with EDS elemental mappings of Bi–Bi_2S_3 nanorod unveil those Bi and S elements uniformly dispersed throughout the structure. Formate was the highly selective main product at high faradaic efficiency of 85%, accredited to the synergistic coupling effect of co-catalyst structure. The maximum current density reached a maximum of 17 mA cm^{-2} for Bi–Bi_2S_3, which is comparably better than the current density (12.9 mA cm^{-2}) observed for Bi_2S_3 catalysts. They also concluded that the synergistic effect between Bi_2S_3 and Bi^0 contributes to better product selectivity in high potentials.

2.4.4 Morphology and structure modulation. Several researchers found that carbonate ($*CO_3H$) intermediate adsorbed on the catalyst surface, which further reduced to *COOH and *OOCH intermediates, might also be enhanced for formate production.[248] In this regard, Wang *et al.*[249] prepared sulfur-modulated bismuth subcarbonate nanosheets using a facile hydrothermal method. They reported that sulfur incorporation significantly enhanced the local electron density around the Bi active sites and promoted proton-coupled electron transfer. The two-dimensional sulfur-doped bismuth subcarbonate (S-BiOC)

nanosheet contributed excellent CO_2 reduction with more than 90% FE_{HCOOH}, a broad negative potential range, and high partial current density.

Generally, like monolayers, nanosheets with highly active sites should be as thin as possible. But Wang *et al.*[250] demonstrated that it is not always 'the Thinner the Better.' They developed a microkinetic model that exhibited by considering the stabilization energy evolved by the spin–orbit coupling (SOC) effect; the Bi bilayer was found to have the most excellent catalytic activity of all the Bi nanosheets.

2.5 Molybdenum (Mo)-based sulfide

Molybdenum, a VIB group material, is a promising candidate for electrocatalytic applications. Among all the molybdenum (Mo)-based materials, molybdenum disulfide (MoS_2) exhibited better HER activity, attracting huge research attention in the past few years.[251] Before the twenty-first century, Molybdenum disulfide (MoS_2) was discarded as a prospective candidate as bulk MoS_2 was found to be inactive for electrochemical applications. In 2006, theoretical DFT studies discovered that the edge-exposed MoS_2 sites showed excellent catalytic activity,[252] further validated by Jaramillo *et al.*[253] using an experimental approach. The electrochemical assessment results exhibited that the catalytic activity was linearly allied with the number of exposed sites on the MoS_2 catalyst.[254] Molybdenum disulfide (MoS_2), as a two-dimensional (2-D) layered structure, offers high surface area, large electrical conductivity, and is rich in active sites. As van der Waal forces assembled these two-dimensional layers, MoS_2 can be considered a single sheet composed of multiple-layer nanosheets with edges having exposed active sites because of metallic properties and high d-electron density.[255]

The weak van der Waals interaction holds the stacked parallel layers of bulk MoS_2, just like graphite.[251] In 2014, Asadi *et al.*[256] first reported layer-stacked bulk MoS_2 with Mo-terminated edge catalyst towards the ECO_2R process. They observed that inexpensive and adaptable bulk-MoS_2 achieved high catalytic performance (FE_{CO} of more than 95% and a higher current density of 65 mA cm^{-2} at −0.764 V *vs.* RHE) for CO_2 reduction than costly noble metals such as Ag and Au. The higher current density in CO_2 reduction occurred mainly due to higher d-electron density in the Mo-terminated edges. This research suggested that TMCs can replace expensive noble metal catalysts (Ag, Au) for CO_2 reduction accompanied by product conversion and selectivity.

2.5.1 Substrate coupling. The edge site modification of the MoS_2 with carbonaceous support such as graphene,[257,258] CNTs,[259,260] carbon fibers/clothes,[261] and porous amorphous carbon[262] are necessary for ECO_2R and have been shown to enhance the catalytic efficiency and catalyst regeneration. For example, Li *et al.*[263] developed reduced graphene oxide supported polyethyleneimine-modified amorphous molybdenum sulfide, a low-cost catalyst for ECO_2R to CO in an aqueous medium. The synergistic interaction between the MoS_x and polyethyleneimine (PEI) catalyst reduced the activation energy for the conversion of the intermediates and enabled the CO_2-

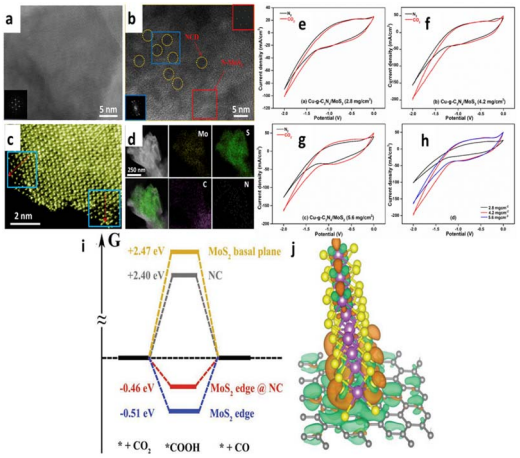

Fig. 16 HRTEM images of (a) E-MoS_2. (b) N-MoS_2@NCDs-180, the blue frame represents NCD and the red frame represents N-MoS_2. (c) Higher magnification HAADF image of N-MoS_2@NCDs-180 shows clearly distinct atomic configuration. (d) TEM image and corresponding elemental mappings of the N-MoS_2@C-180 nanosheets (reprinted with permission from ref. 264. Copyright 2019, Elsevier). CV of Cu-g-C_3N_4/MoS_2 composite material in N_2 and CO_2 saturated $KHCO_3$ solution with different catalytic loading such as (e) 2.8 mg cm^{-2}, (f) 4.2 mg cm^{-2}, and (g) 5.6 mg cm^{-2}; (h) comparison of CV of the Cu-g-C_3N_4/MoS_2 composite with different catalytic loading in CO_2 saturated $KHCO_3$ solution (0.5 M) (reprinted with permission from ref. 265. Copyright 2022, Elsevier). (i) The DFT calculations for demonstrating free energy profiles for ECO_2R catalyzed by different models at the equilibrium potential of −0.11 V. (j) The illustration of electron density changes in the NCMSH model (reprinted with permission from ref. 266. Copyright 2019, John Wiley & Sons, Inc).

reduction reaction at low potentials. They further reported that rGO as a substrate material increased electrical conductivity and catalytic stability.

Zhu *et al.*[264] prepared Nitrogen-doped MoS_2 (N-MoS_2) nanosheets and nitrogen-doped carbon nanodots (NCDs) composite for ECO_2R catalysts by a simple solvothermal method in the presence of exfoliated-MoS_2 and DMF as a solvent. As depicted in Fig. 16a–d, the HRTEM images explored a clear lattice fringe above the surface of N-MoS_2 nanosheets due to the uniform distribution of NCDs (diameter of 6 nm). The composite catalyst N-MoS_2@NCDs-180 with the high N content (8.35 at%) achieved FE_{CO} over 90% with a low onset potential. Energy calculations exposed that the N-doping procedure enhanced the electron density on the edge sites of MoS_2, which significantly decreases the energy barrier of the COOH* intermediates, consequently promoting CO formation. Hussain *et al.*[265] found that Cu-g-C_3N_4/MoS_2 hybrid material exhibited a much greater faradaic efficiency (19.7% and 4.8% for methanol and ethanol, respectively) compared to g-C_3N_4, MoS_2, Cu-g-C_3N_4, and Cu-MoS_2 in terms of current density and reduction potential (Fig. 16e–h). This increase in faradaic efficiency was attributed to high electrochemically active surface area (ECSA) and the synergistic effect between their components. The chronoamperometric study of the Cu-g-C_3N_4/MoS_2 hybrid material presented its long-term stability, without any decay in the current density, for up to 30 h. In another study, Li and the group prepared a hierarchical

hollow composite electrocatalyst of N-doped carbon (NC) and edge-exposed 2H MoS_2 (NCMSH). Theoretical analysis as shown in Fig. 16i revealed that the intermediates energy profiles for electrochemical CO_2 reduction activity for different models and the MoS_2 edge@NC catalyst (with an overpotential of 0.46 V) was the most effective among all the tested models. They also predicted that Mo sites stabilizes after taking electrons from the NC, which enhances more active edges exposed Mo sites and accelerates the electrocatalytic activity (Fig. 16j).[266]

2.5.2 Heteroatom doping. The effect of metal centers can synergistically affect the electrochemical performance of MoS_2. For example, Shi *et al.*[267] developed Cu nanoparticles interspersed with MoS_2 nanoflowers for selective conversion of CH_4 in an aqueous electrolyte. Compared to MoS_2 nanosheet electrode (−2.4% at −1.4 V_{SCE} and 4 mA cm^{-2} at −1.7 V_{SCE}, respectively), the designed Cu/MoS_2 composite achieved a better faradaic efficiency (17.08% at −1.4 V *vs.* saturated calomel electrode) and electron conductivity (−17 mA cm^{-2} at −1.7 V_{SCE}) for CH_4 formation. The use of Cu nanoparticles as a doping material has achieved unprecedented results for the reduction of CO_2 due to their enhanced electronic conductivity, higher specific surface area (51.6 m^2 g^{-1}), and synergetic effect between Cu NPs and MoS_2. In a similar work, Abbasi *et al.*[268] synthesized niobium-doped on vertically oriented MoS_2 with 20 nm thickness *via* the chemical vapor decomposition (CVD) method. Their findings revealed that a lesser amount of Nb atoms on Mo edges increased the TOF value for CO production and modified the binding energies of the reaction intermediates to the MoS_2 edge.

2.5.3 Interfacial engineering. Recently, Hussain *et al.*[269] employed a facile solution chemistry approach to synthesize non-noble metal-based Cu_2O nanoparticles decorated MoS_2(-Cu_2O–MoS_2) nanosheets using an environmentally benign reducing agent Glucose. They observed that the composite material (Cu_2O–MoS_2) exhibited exceptional ECO_2R activity, with a current density of 113 mA cm^{-2}, almost two times that of bare Cu_2O (61 mA cm^{-2}) and eightfold that of MoS_2 nanosheet (21.3 mA cm^{-2}). The authors attribute this improvement in catalytic activity because of the synergistic effect between the Cu_2O–MoS_2 composite catalyst. The faradaic efficiency of the composite catalyst depends on the applied potential, reaching a maximum of 12.3% for methanol and 7.9% for ethanol at −1.3 V_{RHE} and −1.1 V_{RHE}, respectively. Electrochemical impedance spectroscopy (EIS) study exhibited that the composite catalyst with a catalytic loading of 4.8 mg cm^{-2} presented an excellent electrocatalytic activity due to increase in charge transfer and decrease in ohmic resistance. The chronoamperometric studies examined the stability of Cu_2O–MoS_2 composite material in CO_2 reduction.

2.5.4 Polymorph engineering. Polymorph engineering of MoS_2 is an effective approach to tune its electronic conductivity: a study by Lv *et al.*[270] shows that hydrophobic exfoliated MoS_2 (H-E-MoS_2) nanosheets modified fluorosilane (FAS) act as an active CO_2 electroreduction catalyst under aqueous medium (Fig. 17a–d). The HRTEM images (Fig. 17e and f) and fast Fourier transform (inset) revealed that the E-MoS_2 layers were composed of two clearly distinct structural domains consisting

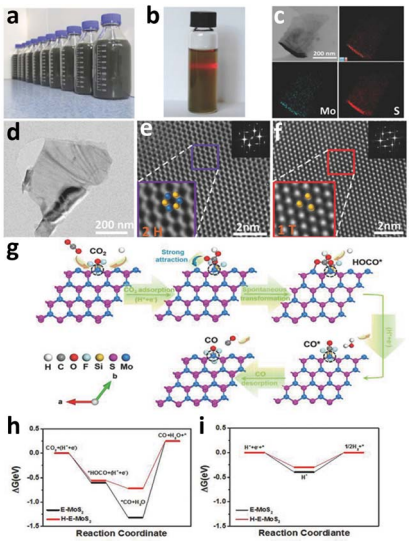

Fig. 17 (a) Digital photo of the exfoliated MoS_2 (E-MoS_2) nanosheets in NVP with a concentration of 3 mg mL^{-1} after ball milling. (b) Tyndall effect of the diluted E-MoS_2 dispersion. (c) TEM image of E-MoS_2 nanosheet and corresponding EDX maps, showing clearly the homogeneous distribution of Mo and S. (d) HRTEM image of an E-MoS_2 nanosheet. (e and f) Higher magnification HRTEM images of an E-MoS_2 nanosheet, showing atomic-resolution structural information, and their corresponding fast Fourier transforms (FFTs). Insets show the 2H and 1T phases in (e and f), respectively. (g) Schematic representation of CO formation mechanism on the H-E-MoS_2 monolayers. The atoms in the dashed circle are the catalytic sites (Mo atoms). Calculated free energy diagrams for (h) CO_2 electroreduction to CO and (i) the HER (reprinted with permission from ref. 270. Copyright 2018, John Wiley & Sons, Inc).

of a 1T (trigonal) phase and a 2H (hexagonal) phase, and the magnified images of selected regions further confirmed the coexistence of both 1T and 2H phases and is regarded to be a key to enhanced performance and stable selectivity. According to Fig. 17h and i, DFT results suggested that the FAS anchored on H-E-MoS_2 modified the electrical conductivity of the MoS_2 layer and lowered the energy barrier of the rate-determining CO-desorption step while increasing the energy barrier of H desorption. The reaction mechanism is also described in detail, as shown in Fig. 17g. Briefly, the single Mo atom of the H-E-MoS_2 adsorbs CO_2 and is combined with a proton–electron pair (H^+ + e−) to generate HOCO* intermediate. The HOCO* intermediate further evolved into a more stable structure in which HOCO* connected with two nearby Mo atoms. Subsequently, the HOCO* intermediate reacts with H^+ and e− to create the product. Therefore, in 2019, Chen *et al.*[271] employed DFT calculations to study ECO_2R on molybdenum sulfide monolayer with 2S vacancy in the 2H phase MoS_2 (DV-MoS_2) basal plane. Detailed electronic studies showed that steric hindrance in the DV-MoS_2 basal plane enhances CO–CH_4 conversion with high catalytic activities and product selectivity. In 2019, Kang *et al.*[272] used the modified CHE model to theoretically predicts possible electrochemical pathways for ECO_2R on V_S-MoS_2. The group demonstrated that the condensation of HCHO molecules is essential for forming C–C coupling at V_S. The CHE model

predicts that routes to multiple CN species for $N < 4$ can open at 0.40 V, whereas C4 product formation is unfavorable at such low potentials. These findings are consistent with the recent experiment, indicating that the V_S of MoS_2 is an essential active site for ECO_2R. They also reported that by implementing cascade catalysts and doping, ECO_2R selectivity improves against HER.

2.5.5 Morphology and structure modulation. As reported, ordinary binary TMDs typically showed low electrical conductivity, less active sites, and low intrinsic activity, which limited their electrochemical activity. Notably, the latest research found that ternary TMDs alloy monolayers possessed an ultra-high ratio of surface exposed atoms that potentially serve as the relatively single active sites.[273–275] Therefore, to check the faradaic efficiency, Xie and co-workers fabricated ternary TMDs alloy monolayers (MoSeS) for ECO_2R. Their catalytic system resulted in FE_{CO} of ~45%, which was remarkably more than those of MoS_2 (~16%) and $MoSe_2$ (~30%) monolayers at −1.15 V_{RHE}. They exhibited a current density of 43 mA cm^{-2} against −1.15 V_{RHE} which was 1.3 times that in MoS_2 and $MoSe_2$ monolayers. The monolayers (MoSeS) increase CO_2 adsorption and CO desorption rate with a low work function. The catalyst was found to be excellent for syngas formation as the only product.[276] In another study, Chan *et al.*[277] performed pioneering work by applying the QUANTUM ESPRESSO code and the BEEF-vdW exchange-correlation functional in investigating the electrocatalytic effect of S and Se in the reductive decomposition of CO_2 in aqueous media. The calculations indicate that combining S or Se atoms at the edge sites of TMDs monolayers promoted the binding of CHO and COOH intermediates rather than CO. They also reported that CO could be further reduced to hydrocarbons and alcohols by the S edges of Ni-doped MoS_2 and the Mo edges of $MoSe_2$. However, S edges in undoped and Ni-doped MoS_2 were found to suppress the HER and accelerate the ECO_2R compared to Mo edge sites. This research demonstrated that edge site tuning of TMDs should be tailored for improved CO_2 reduction.

2.6 Indium (In)-based sulfide

In_2S_3, a common III–VI main-group chalcogenide, exists in three crystallographic forms: a defective cubic structure α-In_2S_3, a defect spinel structure α-In_2S_3, and a higher-temperature-layered structure α-In_2S_3.[278] Besides, several In_2S_3 nanostructures, including nanoflakes,[279] nanosheets,[280] and flower-like microspheres,[281] were reported for electrochemical applications.

2.6.1 Heteroatom doping. Metal doping have also been widely used to modify electrocatalysts to bring about charge redistribution on the surface to adjust the ECO_2R activation:[225,226] Yuan *et al.*[282] modified In_2S_3 nanosheets doped with *in situ* formed metallic In atoms (In-In_2S_3) for the ECO_2R process. The hybrid electrocatalyst achieved a higher current density of 70.3 mA cm^{-2} at −1.1 V *vs.* RHE with a faradaic efficiency of 90% at −1.0 V_{RHE} (76% for HCOOH generation and 14% for CO generation). Similarly, Zhang *et al.*[283] synthesized thin Mn-In_2S_3 nanosheets and observed high faradaic efficiency (90% at −0.9 V_{RHE} with a current density of 20.1 mA cm^{-2}) for formate production (Fig. 18a–e). The mechanistic study demonstrated that Mn doping facilitated harmonic overlaps between the p orbitals of O atoms of CO_2 and the d orbitals of Mn atoms near the conduction band edge of the Mn-In_2S_3 slab. The unique structure lowered the energy barrier for initial CO_2 adsorption to form HCOO* intermediates; thus, they achieved effective CO_2-to-HCOOH conversion. In another work, Chi *et al.*[284] prepared Zn-modulated indium sulfide (In_2S_3), and the resultant catalysts $ZnIn_2S_4$ exhibited long-term stability for ECO_2R (Fig. 18f–h). The synthesis procedure enabled the modification of its phase and structure without affecting the morphology of the catalyst (Fig. 18i–m). Experimental and theoretical studies demonstrated that incorporating Zn enhanced the covalency of In–S bonds and stabilized sulfur – a catalytic site activating H_2O to combine with CO_2, resulting in the formation of the HCOO* intermediates. Thus, $ZnIn_2S_4$ achieved unprecedented CO_2 to formate production with stability up to 60 h.

2.6.2 Morphology and structure modulation. Feng *et al.*[285] studied the catalytic behavior of flower-like In_2S_3 assembled by nanoflakes catalyst for CO_2 conversion to HCOOH (Fig. 19a and b). The flower-like structure In_2S_3 electrocatalyst achieved higher formate selectivity (FE_{HCOOH} of 86%) compared to bulk In_2S_3 (FE_{HCOOH} of 63%) prepared *via* the hydrothermal method. The mechanistic studies explain that the complete route of ECO_2R to formate involves two-electron and two-proton transfer

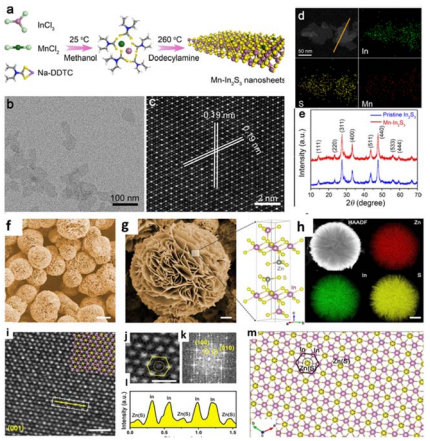

Fig. 18 (a) Scheme of the synthetic procedure of Mn-In_2S_3 nanosheets. (b) TEM image of Mn-In_2S_3 nanosheets. (c) HAADF-STEM image of an individual Mn-In_2S_3 nanosheet. (d) HAADF-STEM and STEM-EDX elemental mapping images of the Mn-In_2S_3 nanosheet. (e) XRD patterns of pristine In_2S_3 and Mn-In_2S_3 nanosheets. (Reprinted with permission from ref. 283. Copyright 2019, American Chemical Society); physical characterization of $ZnIn_2S_4$. (f and g) SEM images of the $ZnIn_2S_4$ catalyst. The right panel in (g) shows the crystal structure of $ZnIn_2S_4$. Scale bars, 5 μm (f) and 1 μm (g). (h) STEM-EDX elemental mapping of $ZnIn_2S_4$, exhibiting a uniform spatial distribution of Zn (red), In (green), and S (yellow), respectively. Scale bar, 1 μm. (i and j) Atomic-resolution Z-contrast images of $ZnIn_2S_4$ along [001] zone axis. Scale bars, 1 nm (i) and 0.5 nm (j). (k) The corresponding FFT pattern of (i). (l) The line intensity profile acquired along the yellow arrow in (i). (m) Atomic model of $ZnIn_2S_4$ along [001] zone axis. (Reprinted with permission from ref. 284. Copyright 2021, Nature Publishing Group).

processes *via* adsorbed CO_2 (CO_2*) and OCHO* intermediate. They employed DFT to calculate the adsorption energy of intermediates on the main exposed (311), (440) facets of flower-like In_2S_3, and (400) facets of bulk In_2S_3. The results depicted (440) facet shows the most negative adsorption energy on both CO_2* and OCHO*; this indicates (440) facet is advantageous to the binding of CO_2 and stabilizing OCHO*, which are convenient for decreasing onset potential and enhancing selectivity of formate, respectively.

In a recent report, Ma and the groups developed sulfur-doped indium (S–In) catalysts for efficient CO_2 reduction to formate (Fig. 19c and d). They fabricated a number of S–In catalysts with changing sulfur proportions by electro-reduction of sulfur-containing In_2O_3 precursors *via* the hydrothermal method. The S–In catalyst with 4.9 mol% sulfur content showed an exceptional formate generation rate of 1002 μmol h^{-1} cm^{-2} with more than 90% FE, 17 and 1.6 times higher than the In foil. Furthermore, the S–In catalysts possessed high formate FE (>85 percent) for ECO_2R in aqueous alkaline environments over a wide current density range (25–100 mA cm^{-2}). The production rate of formate in $CsHCO_3$ aqueous solution climbs to 1449 μmol h^{-1} cm^{-2} with a current density of 84 mA cm^{-2} and FE of 93%. As shown in Fig. 19e, DFT calculation exhibited the optimal adsorption configurations of reactants, intermediates, and products on indium and sulfur-doped indium surfaces. Theoretical studies also demonstrated that, for the HCOOH pathway, S–In catalysts minimize the Gibbs free energy for forming *COOH intermediates from 0.29 eV to −0.16 eV (Fig. 19f); and for the CO pathway, the Gibbs free energies for the formation of *COOH intermediates are 1.49 and 0.82 eV on bare In and S–In surfaces, respectively (Fig. 19g). Based on the DFT results, they suggested that the surface S^{2-} species acts as an anchor to keep the $K^+(H_2O)_n$ cation near to indium surfaces in the double layer *via* Coulomb interactions (Fig. 19i). As a result, the presence of sulfur on the indium surface provides a substantial energy advantage to the HCOOH pathway (Fig. 19h). However, tailoring In with Se and Te can enhance the FE with a higher formate generation rate, similar to sulfur. More interestingly, the group also identified as the electronegativity of chalcogen atoms is reduced, their affinity to adsorb *H species decreases, and the rate of formate generation also falls in the order S–In > Se–In > Te–In.[286]

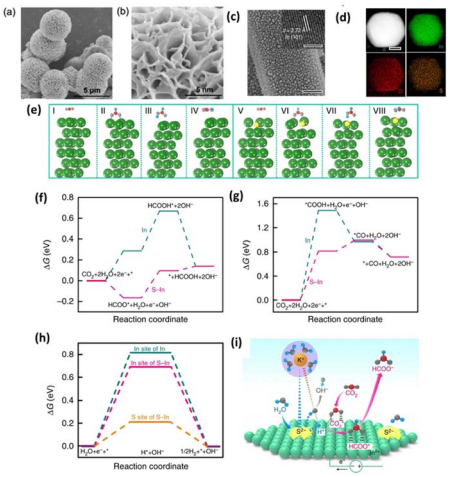

Fig. 19 SEM images of flower-like In_2S_3, (a) low-magnification and (b) high-magnification (reprinted with permission from ref. 285. Copyright 2019, John Wiley & Sons, Inc); characterizations of morphologies and chemical states for S–In catalysts. (c) SEM image and HRTEM image (insert) of S2–In catalyst. (d) STEM image of S2–In catalyst and the corresponding EDS elemental mapping. DFT calculation and reaction scheme (e) optimized configurations of (I) CO_2, (II) HCOO*, (III) HCOOH*, (IV) HCOOH on (101) facet of pure indium (In) and (V) CO_2, (VI) HCOO*, (VII) HCOOH*, (VIII) HCOOH on (101) facet sulfur-doped indium (S–In). (f) Gibbs free energy diagrams for ECO_2R to HCOOH on In (101) and S–In (101) surfaces. (g) Gibbs free energy diagrams for ECO_2R to CO on In (101) and S–In (101) surfaces. (h) Gibbs free energies for the formation of H* on pure In (101), In and S sites of S–In (101) surfaces. (i) Schematic illustration of the role of S^{2-} in promoting water dissociation and H* formation for the reduction of CO_2 to formate. Free energies of (d, e and f) are shown relative to gas CO_2 and H_2. The green, yellow, gray, red, and blue balls represent In, S, O, C, and H (reprinted with permission from ref. 286. Copyright 2019, Nature Publishing Group).

2.7 Lead (Pb)-based sulfide

Similar to other metals, *i.e.*, Sn and In, metallic Pb electrodes in aqueous electrolytes are also beneficial for producing HCOOH. In 1985, Hori *et al.* first reported Pb metal electrode in an aqueous solution for CO_2 to formate production.[41] Earlier studies reported that among Sulfide-derived (SD)-Pb, oxide-derived (OD)-Pb, and Pb cathodes, SD-Pb showed high catalytic activity for formate generation.[287] However, the application of PbS is still limited in the ECO_2R process.

2.7.1 Morphology and structure modulation. Recently, Pander *et al.*[288] emphasized the relation between catalyst morphology and HCOOH formation. They prepared S-derived Pb and O-derived Pb by reducing the PbS and PbO_x precursors. Compared to O-derived Pb (derived from PbO), the wafer-structured S-derived Pb showed better stability and catalytic activity (FE_{HCOOH} of 88% and $j_{HCOO^-,geom}$ of 12 mA cm^{-2} at −1.08 V_{RHE}) in 0.1 M $KHCO_3$ electrolyte. This work showed that wafer-structured SD-Pb exhibited better ECO_2R performance.

In a different report, Zhang *et al.*[289] used a hot-injection colloidal approach to create well-defined PbS nanocrystals (NCs) with tuneable sizes ranging from 5 to 12 nm. They investigated that during electrochemical CO_2 reduction, the PbS NCs undergo restructuring to Pb thin films, which achieved >90% $FE_{formate}$ over a wide range of −1.0 to −1.2 V *vs.* RHE and a maximum mass activity of 69.8 mA $mgPb^{-1}$. With the aid of an *in situ* synchrotron radiation X-ray diffraction (SR-XRD) technique, the authors demonstrated that during the PbS-to-Pb structural transformation, initially $PbCO_3$ is generated from the anion exchange in PbS between $CO_2/HCO_3^-/CO_3^{2-}$ and SCN^- (generated by the anion-exchange), as well as S^{2-}. And then $PbCO_3$ further reduced to Pb thin films.

2.8 Zinc (Zn)-based sulfide

Zinc sulfides are well-known semiconductor materials with appropriate large band gaps. With such distinct properties, zinc sulfide based materials have been employed in photocatalysis,

optical coatings, and various other applications and have gained considerable interest.[290] Many morphologies of zinc sulfides, such as nanowires,[291,292] nanorods,[293] nanosheets,[294] nanotubes,[295] and other low-dimensional materials,[296] have been reported by researchers. However, the application of Zn-based sulfides and their derivatives as ECO_2R catalysts is still limited.[297–299]

2.8.1 Interfacial engineering. Zhen *et al.*[297] synthesized ZnS/Zn electrode using sulfur infiltration techniques, demonstrating well-developed surface technology treatment. They found ZnS/Zn comprises three layers; ZnS is the upper layer, Zn is the substrate, and the transition layer in between (Fig. 20a). As shown from SEM images (Fig. 20b and c), this transition layer plays a significant role in strongly connecting the upper layer (ZnS) to the substrate (Zn) by offering more active sites. The current density was found to be stable at 6.72 mA cm^{-2} at −2.4 V_{Fc/Fc^+} with a faradaic efficiency (FE_{CO}) of 92% for ECO_2R in propylene carbonate/tetrabutylammonium perchlorate (PC/TBAP) electrolyte. In another work, Li and the group developed an exciting ECO_2R catalyst by tailoring the Zn nanosheet surface with ZnS subnanometer layer. Notably, the S–Zn–S nanosheet electrodes exhibited high faradaic efficiency and outstanding stability. Its performance is better than all previously stated Zn-based catalysts and comparable to noble metal electrocatalysts. Experimental and theoretical studies showed that S atoms in S–Zn–S nanosheets modified the Zn nanosheet to provide higher adsorption capability of the *COOH intermediate, improving CO_2 reduction and overturning the competing HER process. They found that S–Zn–S NSs achieved the highest FE of ~94.2% at −0.8 V *vs.* RHE for CO formation, which outperformed all Zn-based catalysts reported in the literature.[298] Recently, Song and co-workers fabricated ZnS/ZnO heterogeneous interfacial structure for improved CO_2 reduction performance (Fig. 20d). The ZnS/ZnO interface structure (Fig. 20e) considerably increases the ECO_2R performance (FE_{CO} 98%) than ZnS (FE_{CO} ~66%) and ZnO (FE_{CO} ~88%) catalysts, presenting a promising approach for developing an inexpensive, stable, and high-performance catalyst.[299]

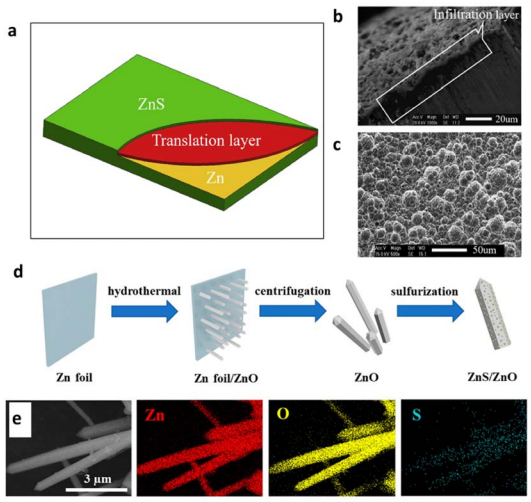

Fig. 20 (a) A schematic diagram of the infiltration layer (b and c) scanning electron microscopes image of ZnS electrode (reprinted with permission from ref. 297. Copyright 2018, Elsevier); (d) schematic diagram of the synthesis process of ZnS/ZnO catalyst; (e) SEM image and corresponding EDX elemental maps of ZnS/ZnO catalyst (reprinted with permission from ref. 299. Copyright 2021, American Chemical Society).

2.9 Titanium (Ti)-based sulfide

TiS_2 is a potential CO_2-to-CO conversion option because of the cohesive van der Waals type of bonding structure with zero bandgaps similar to TMDs such as Mo and W and semimetal class with conductivity similar to graphite.[300,301] In 2020, Aljabour *et al.*[302] synthesized semi-metallic titanium disulfide (TiS_2) using atomic layer deposition (ALD) methods. The catalyst exhibited exceptional cathodic energy efficiency of 64% and carbon conversion efficiencies, the combined faradaic efficiencies of 95% for CO and formate, with $j_{co} = 5$ mA cm^{-2} at −0.5 V_{RHE}. *In situ* FTIR further revealed that sulfur and CO_2 are bound as monothiocarbonate intermediates, which kinetically favored the higher CO formation.

2.10 Other metal-based sulfides

Simon and the group used the microwave-assisted non-aqueous sol–gel method to synthesize phase-pure spinel Ni_2FeS_4 nanosheets with a specific surface area of 80 m^2 g^{-1}. They utilized metal acetylacetonates and benzyl mercaptan as a sulfur precursor. They found noble metal-free Ni_2FeS_4 nanosheets electrochemically active for CO production from aqueous CO_2 at a potential of −0.7 V *vs.* RHE and CO product selectivity of 6.0% with a faradaic efficiency of 5.9%.[303] Similarly, Zhao *et al.*[304] developed FeS_2/NiS nanocomposite electrocatalyst by simple hydrothermal synthesis. It was seen that active sites at the FeS_2 and NiS interface efficiently suppressed the HER and facilitated CO_2 reduction. The low-cost nanocomposite catalyst obtained a 64% FE for CO_2 to CH_3OH. This research shows active sites at the FeS_2 and NiS interface suppressed the HER side reaction while promoting the ECO_2R.

In 2018, Piontek and co-workers reported a low-cost, efficient bimetallic sulfide $Fe_{4.5}Ni_{4.5}S_8$ (pentlandite) for electrochemical water splitting and CO_2 reduction with solvent-dependent product selectivity. Interestingly, they found that using aprotic solvents such as acetonitrile, dimethylformamide, dimethyl sulfoxide, and propylene carbonate with well-defined water concentrations suppressed HER and favored ECO_2R. The bimetallic sulfide presented a faradaic efficiency of 87% and 13% for CO and CH_4, respectively, with a current density of 3 mA cm^{-2}. The findings revealed that optimizing the availability of protons in the electrolyte–electrocatalyst interface was crucial for effective ECO_2R.[305] Inspired by the work done by Tetzlaff *et al.*[306] with Fe/Ni ratio in $Fe_xNi_{9-x}S_8$ for CO_2 electroreduction, Pellumbi *et al.*[307] explored the effect of S/Se by preparing bimetallic sulfide composite $Fe_{4.5}Ni_{4.5}S_{8-y}Se_y$ (y = 1–5). The results demonstrated that the selectivity for CO increased as the Se percentage increased, and the maximum faradaic efficiency reached 84% with the composition $Fe_{4.5}Ni_{4.5}S_4Se_4$. The formation of the product was changed due to variation of average interatomic distances at the active sites. Briefly, with the

increasing Se concentration, the dimensions of the underlying crystal lattice and the metal–metal distances gradually increased, suppressing proton binding and promoting CO_2 binding. In 2023, Han and the collaborators[308] synthesized Cu/Ag(S) using electrochemical treatment derived from $Cu/Ag_2S/Ag$, incorporating Cu single atom in Ag(S) defective sites. Consequently, the resulting yield and ECO_2R faradaic efficiency (FE_{ECO_2R}) reach 93.0% at an ECO_2R partial current density (j_{ECO_2R}) of 2.9 mA cm^{-2} under −1.0 V *vs.* RHE, respectively, showing a significant improvement as compared to that of sulfur-removed Ag_2S/Ag without Cu SACs (Ag(S), 78.5% FE_{ECO_2R} with 1.8 mA cm^{-2} j_{ECO_2R}). The group, by *in situ* and *ex situ* characterizations together with theoretical calculations, proposed interaction between Cu SACs and their neighboring defective Ag surface increase microstrain and downshift the d-band center of Cu/Ag(S), thus lowering the energy barrier by ~0.5 eV for *CO formation, which leads to the improved ECO_2R activity and selectivity toward CO and C_{2+} products.

However, for MS-based nanomaterials, S leaching was also widely observed during ECO_2R. For example, CuS is not thermodynamically stable in the reduction process and can easily convert into metallic Cu, CuO, or Cu_2O as per the observations from XPS and HRTEM analysis.[126,139,151] In this regard, Shinagawa *et al.*[145] did XPS and SAED analysis with the post-reaction sample. They demonstrated that during ECO_2R cathodic environment induces the loss of excess sulfur in the catalysts and that the S-modified materials, irrespective of the initial sulfur content, can significantly affect the stability of the catalyst. Zhao *et al.*[152] employed XPS and HRTEM and demonstrated that in ECO_2R, CuS nanosheets are partially reduced to metallic Cu, and the metallic Cu phase is partially oxidized to CuO after CO_2 electroreduction. Furthermore, Zhang and the collaborator employed XPS in their work and demonstrated CuS-HP electrocatalyst prepared from HKUST-1 was reconstructed to Cu(S) with a minimal $S^{\delta-}$ ($0 \leq \delta \leq 2$) in the derived catalysts. Further, they observed that despite having less S content, the polyhedron structures offer high activity and stability during the ECO_2R.[155] In this context, the ECO_2R mechanism on sulfur-modified Cu electrodes for highly selective formic acid (HCOOH) generation was investigated using experiment-based theoretical DFT modelling.[309] The stability of residual sulfur atoms was discovered to be highly dependent on their local environment and symmetry, with the majority of sulfur existing in relatively unstable forms that satisfy the experimentally observed negative XPS shift[157] and strong CO* surface-enhanced infrared absorption spectroscopy signal.[157,158] At the early stages of ECO_2R, the reduced S migrates from the Cu electrode to the electrode–electrolyte interface and CO* readily forms at the Cu electrode surface. During this dynamic process, additional of reduced S and already formed CO* appear at the interface due to a cooperation mechanism; that is, CO* reduces the loss of sulfur by stabilizing the residual S at Cu electrode surface, increasing the CO* coverage by enhancing CO* adsorption. According to the DFT simulation, ECO_2R energy diagrams revealed that these types of reduced S do not directly facilitate formic acid production but instead dominant CO* production and strong CO* adsorption. Theoretical study also confirms that the strong CO* adsorption caused by the sulfur atoms, increases CO* coverage four times more than clean Cu surface. At the end of the reaction, surface reaction sites are blocked in the presence of the dense CO* network, which leads to solution-phase CO_2 hydrogenation and favours highly selective HCOOH production.[145,310] Finally, a synergistic effect between residual S and CO* to achieve dominant formic acid production for the electrochemical CO_2 reduction reaction is proposed by combining actual experimental observations from the literature and our DFT calculations. These findings detailed the fundamental understanding of the important role of S atoms in a highly selective CO_2 electroreduction mechanism on metallic Cu surfaces. Meanwhile, it should be noted that this S-modified Cu electrode is a thermodynamically metastable structure, and further S loss during the reactions could be hindered the mechanism for ECO_2R towards HCOOH formation.[309]

Meanwhile, in work by Li *et al.*,[191] XPS results evidenced the negligible changes of the corresponding peak positions in Cd^{2+} and the S^{2-} XPS spectra of the initial and used electrocatalysts only with the reduced intensity. These findings support the stability of CdS nanorods during ECO_2R. In another work published by Luo's group, SnS_2 monolayers were synthesized by a facile Li intercalation/exfoliation method. Later, the XRD analysis of the catalysts after electrolysis indicated that the SnS_2 monolayers were partially reduced to metallic Sn in the CO_2 electroreduction.[232] Like SnS_2, defect-rich Bi_2S_3 also tends to reduce metallic Bi during ECO_2R; as observed by HRTEM analysis before and after electrolysis, Zhang *et al.*[245] exhibited a lattice fringe of 0.22 nm corresponding to (110) plane, suggesting the complete reduction of sulfide to crystalline Bi. A work by Chi *et al.*[284] illustrated a loss of excess S content for In_2S_3 during ECO_2R. A combined XPS and SEM-EDX results demonstrate that the stability degradation of In_2S_3 can be attributable to S leaching. Pander *et al.*[288] elucidated from XPS studies that the PbS would be partially reduced to metallic Pb in ECO_2R, and the metallic Pb phase could be further partially oxidized to PbO after electrochemical CO_2 reduction. Further, for most of the MS-based nanomaterials, it was observed that during ECO_2R S^{2-} ions were released into the electrolyte and absorbed on the surface of catalysts, suppressing the formation of other hydrocarbon products and resulting in high selectivity towards HCOOH.[151,153,309] Hence, the method of stabilizing MS-based nanomaterials in the catalytic process without converting them to their metallic and oxide counterparts needs to be explored.

As described in Section 2.1, a variety of strategies have been implemented to control catalyst deactivation (*i.e.*, corrosion and dissolution) and increase the stability and selectivity of MS-based nanomaterials for ECO_2R, including (i) doping, coupling, or loading a passive metal on the semiconductor surface, which acts as a co-catalyst to enhance the rate of electrochemical CO_2 reduction and (ii) tune or alteration of the semiconductor surface with a metal oxide, carbon-based material, or a polymer (iii) using techniques for nanostructuring to change the electrode's surface. These research efforts are aimed at improving the ECO_2R performance and stability of earth-abundant MS-based nanomaterials. The

Table 3 A summary of recently reported best-performing data for carbon-based ECO_2R catalysts

Products	Electrode	Potential	Electrolyte	Reactor	Current density (mA cm^{-2})	FE (%)	Stability (h)	Ref.
HCOOH	Sn/OMC-GDE	−0.86 V_{RHE}	0.5 M $KHCO_3$	Flow cell	80.12	97.4	—	311
	In SACs-1000	−0.79 V_{RHE}	0.5 M $KHCO_3$	H-cell	6.8	85.2	14	312
CH_3OH	Cu-SAs/TCNFs	−0.90 V_{RHE}	0.1 M $KHCO_3$	H-cell	90	44	50	313
Ethanol	Fe-*n*-f-CNTs	−0.80 V_{RHE}	0.5 M $KHCO_3$	H-cell	25	45	—	314
CH_4	SA-Zn/MNC	−1.80 V_{RHE}	1 M $KHCO_3$	H-cell	31.8	85	35	315
	Cu-N-C-800	−1.40 V_{RHE}	0.1 M $KHCO_3$	H-cell	10.6	38.7	10	316
CO	$Fe_1N_2O_2$/NC	−0.50 V_{RHE}	0.1 M $KHCO_3$	H-cell	2.5	99.7	12	317
	Bi-SAs-NS/C	−0.80 V_{RHE}	0.5 M $KHCO_3$	H-cell	10.24	98.3	24	318
	Sn-NOC	−0.70 V_{RHE}	0.1 M $KHCO_3$	H-cell	14.81	94	8	319
	NiSA-N_x-C	−0.80 V_{RHE}	0.5 M $KHCO_3$	H-cell	12	98	10	320
	Fe-SA/BNC	−0.70 V_{RHE}	0.1 M $KHCO_3$	H-cell	2	94	30	321
	A-Ni/CMK	0.80 V_{RHE}	1 M KOH	Flow cell	366	95	5	322
	Ni SAs-NCW	−0.43 V_{RHE}	1 M KOH	Flow cell	41.6	95.4	4	323
	Ni-N/PC	−0.40 V_{RHE}	1 M KOH	Flow cell	100	98	72	324
	CoPc/NH_2-CNT	−0.60 V_{RHE}	1 M KOH	Flow cell	225	100	100	325
	Ni-NC 60% PTFE	−2.73 V_{RHE}	1 M Cs_2SO_4	Flow cell	250	100	36	326
	Ni-SAC-CNT	−0.35 V_{RHE}	1 M KOH	Flow cell	400	99	8	327
	Cu-N-CNT	−0.82 V_{RHE}	1 M KOH	Flow cell	234.3	95.7	25	328
	Ni-$N_{4-x}C_x$	−0.34 V_{RHE}	1 M KOH	Flow cell	300	99.4	6	329
	Fe-NC-Q	−0.40 V_{RHE}	1 M KOH	Flow cell	121	99	10	330
	Ni DSC	−1.20 V_{RHE}	1 M $KHCO_3$	Flow cell	150	94.3	50	331
	CoN_4-CNT	−1.70 V_{RHE}	1 M KOH	Flow cell	350	99.8	8	332

results of prior studies and the performance data for various MS-based nanomaterials were summarized in Table 2. It was noted from Table 2 that certain MS-based electrocatalysts have shown excellent partial current density and faradaic efficiency, as well as suitable levels of stability during the ECO_2R. Besides, to compare the catalytic performance of MS-based nanomaterials focusing on partial current density and faradaic efficiency, recent best-performing carbon-based and copper-based ECO_2R catalysts are reported in Tables 3 and 4, respectively. For instance, CuS/BM coated with PTFE,[154] Sulfur modulated tin catalysts (Sn(S)/Au),[229] SnS/aminated-C,[230] S doped-Bi_2O_3-CNT,[244] in nanoparticles on In_2S_3 nanosheets,[282] $ZnIn_2S_4$,[284] sulfur-doped indium[286] have been exhibited better current density and faradaic efficiency for HCOOH formation as compared to copper-based and carbon-based catalyst. In addition, porous Cd modified by sulfur,[183] Cadmium sulfide (CdS) nanoneedle arrays,[184] Bulk MoS_2 with Mo-terminated edge,[256] rGO-PEI-MoS_x,[263] 5% Nb-doped on vertically oriented MoS_2,[268] ZnS/ZnO Interface[299] exhibited good performance in terms of current density and faradaic efficiency than a copper-based catalyst, for CO production. Meanwhile from Tables 3 and 4, it has been observed that carbon-based catalyst showed better CO current density (<100 mA cm^{-2}) in flow-cell as compared to MS-based nanomaterials. For other products (*i.e.*, C_{2+} and CH_4) Copper-based catalysts exhibited superior performance than MS-based nanomaterials.

3 Summary and future prospects

Metal sulfide-based nanomaterials have been the focus of significant scientific and technical importance due to their high electrocatalytic activity for ECO_2R. In this review: the electrochemical and morphological characteristics of these materials have been compared, and the relationship between structure and electrocatalytic properties has been highlighted, evaluating how it is possible to tune the composition, the active site nature, and the framework of the catalyst for ECO_2R applications. The recent advancement summarized below:

(1) We have shown the concentration of S in MS-based nanomaterials can enhance the activity of ECO_2R catalysts. Furthermore, incorporating S significantly changes reaction intermediates' adsorption/binding energy, thereby improving catalytic performance.

(a) The MS-based nanomaterials exhibited optimum catalytic performance due to the synergy between S and metals' active sites. According to the literature survey of single metals, Cd, Mo, and Zn tends to produce CO, whereas optimizing the electronic structure of metal atoms by introducing S can enhance charge density around the metal atoms, hence facilitating the capture and electroreduction process towards CO_2.

(b) The incorporated defect and interface engineering of S-derived catalysts accelerate charge density distributions on the catalyst surface, thereby tuning the intermediates' free energy and improving the overall catalytic performance.

(2) The chalcogen elements (S, Se) in MS-based nanomaterials are believed to influence the active sites, resulting in high activity and selectivity of ECO_2R. For instance, Sargent group[229] reported that the existence of S atoms on the Sn catalyst surface could promote undercoordinated sites, resulting in improving the ECO_2R to formate selectivity. They have shown by doping S atoms into Sn, the Sn atom near the S atom is responsible for ECO_2R, significantly reducing the free energy of formate production, and improving the overall catalytic performance. Similarly, Xie and collaborators[276] reported that

Table 4 A summary of recently reported best-performing data for copper-based ECO_2R catalysts

Products	Electrode	Potential	Electrolyte	Reactor	Current density (mA cm^{-2})	FE (%)	Stability (h)	Ref.
C_{2+}	Cu nanocubes	−0.7 V_{RHE}	0.25 M $KHCO_3$	H-cell	$j_{C_{2+}} = 41$	60.5	2	333
	Cu_3N	−1.15 V_{RHE}	1 M KOH	Flow cell	$j_{C_{2+}} = 1100$	73.7	6	334
	Defect-site-rich Cu catalyst	−1.02 V_{RHE}	0.1 M $KHCO_3$	Flow cell	$j_{C_{2+}} > 100$	70	30	335
	Cu–CuI composite catalyst	−0.87 V_{RHE}	1 M KOH	Flow cell	591	71	85	336
	Cu $(OH)_2$-D/Cu	−0.54 V_{RHE}	0.1 M $NaHCO_3$	Flow cell	217	∼87	11	337
	(100)-rich Cu	−0.63 V_{RHE}	0.1 M $NaHCO_3$	Flow cell	320	88	65	338
	Cu@C-0.4	−0.7 V_{RHE}	0.1 M $KHCO_3$	Flow cell	1.23	91	16	339
C_2H_4	Activated Cu nanowires	−1.01 V_{RHE}	0.1 M $KHCO_3$	H-cell	∼17.3	77	∼200	340
	Star decahedron Cu NPs	−0.993 V_{RHE}	0.1 M $KHCO_3$	H-cell	17	52.43	12	341
	Cu nanosheets with nano-scaled defects	−1.2 V_{RHE}	0.1 M K_2SO_4	RRDE	60	83.2	14	342
	Cu–Al	−0.5 V_{RHE}	1 M KOH	Flow cell	400	80	100	343
CO	Cu_2Sb decorated Cu nanowire arrays	−0.90 V_{RHE}	0.1 M $KHCO_3$	H-cell	—	86.5	12	344
	Ni–Cu dual atom catalysts	−0.6 V_{RHE}	0.5 M $KHCO_3$	H-cell	95.21	97.7	—	345
CH_3OH	Cu SA/MXene	−1.4 V_{RHE}	0.1 M $KHCO_3$	H-cell	21.3	59.1	30	346
	$Cu_{2-x}Se$	−2.1 V_{Ag/Ag^+}	[Bmim]PF_6-CH_3CN-H_2O	H-cell	41.5	77.6	25	347
CH_4	Cu-MOF-74/Cu NPs	−1.3 V_{RHE}	0.1 M $KHCO_3$	H-cell	10.9	>50	4	348
	Cu/p-Al_2O_3 SAC	−1.2 V_{RHE}	1 M KOH	Flow cell	153	62	—	349
HCOOH	Cu_3P NS/Cu	−0.1 V_{RHE}	0.1 M $KHCO_3$	Flow cell	—	90	16	350
	$In_{1.5}Cu_{0.5}$ NPs	−1.2 V_{RHE}	0.1 M $KHCO_3$	H-cell	3.59	90	5	351

doping Se atoms in MOS_2, enhanced MoS_2's ECO_2R selectivity. DFT calculations revealed that the active site of the ECO_2R is the Mo atom. Adding Se atoms to the system, shortens the MoS bonds, lowering the *CO adsorption energy and improving selectivity for CO production. According to their findings, chalcogen elements in MS-based materials can improve ECO_2R activity and selectivity by adjusting the adsorption energy of reaction intermediates (*COOH and *CO).

(3) The morphology and electrocatalytic properties of metal-sulfides differ significantly from those of their corresponding bare metals. For example, pure metal Mo often exhibits no ECO_2R activity. MoS_2, on the other hand, has a layered structure and can efficiently activate the ECO_2R to CO conversion because the layered structure of MoS_2 can offer more catalytic active sites that lead to the Gibbs free energy changing for intermediate formation. Cu is a commonly used ECO_2R catalyst with high selectivity for producing methane and ethylene. However, S-derived and S-doped copper catalyst mainly produces HCOOH and H_2. Sn exhibits high faradaic efficiency, selectivity, and stability for the formation of HCOOH. In contrast, atomically thin layer SnS shows improved activity during ECO_2R.

Despite its numerous advantages, some key challenges, such as a fundamental understanding of the role of S on materials properties and low catalytic performances (*i.e.*, selectivity and stability, and ambiguity), must be considered. The following research directions can be proposed to address these limitations:

(1) Investigating new MS-based nanomaterials catalysts through novel synthesis and modification methods. Although there are promising developments in the design of catalysts and overall improvement of the ECO_2R process, the catalytic efficiency and product selectivity are still very low. Therefore, more research is required to identify a new class of MS-based nanomaterials. For instance, there are various forms of bismuth, such as single metal, oxide, and oxyhalide with an ordinary 2D structure, which is an attractive material due to its economic and high selectivity for HCOOH production in ECO_2R. However, Bi-sulfide-based materials have not been thoroughly investigated, and additional research is required. An earlier research work studied the role of defect-rich structure and specific interfacial phenomena between Bi_2S_3–Bi_2O_3 interfaces.,[246] which can motivate further research into the effect of sulfur composition on product selectivity, the design of a 2D framework structure with particle size optimization, heteroatom-doping, and so forth. In addition, the electrocatalytic activity of other metal-sulfides, *i.e.*, Lead, zinc, iron, cobalt, and nickel, during ECO_2R should also be further studied. Although this review highlighted the critical advances in interfacial effect and facet promotion, more attention should focus on the strategy development of material doping, composition, and coupling substrate. In this regard, exploring new synthesis methods on highly efficient ECO_2R electrocatalysts would be beneficial.

(2) In order to catalyze the ECO_2R activity in terms of selectivity and stability of MS-based nanomaterials, it is necessary to conduct experimental and theoretical studies to have a better understanding of the role of the S group during the process. For example, the catalyst must be well characterized before increasing the S content to understand the S's local chemical environment comprehensively. Additionally, in order to understand the general trend among the oxygen group elements, it is also required to compare S-derived catalysts with O-derived or new catalysts. Finally, considering the different chemical and physical properties of catalysts, it should be investigated further whether their outstanding electrochemical performance can be attributed to defects or residual S.

(3) Improving product selectivity and catalyst stability of MS-based nanomaterials during ECO_2R. The ECO_2R catalytic selectivity of most MS-based nanomaterials is relatively unitary,

the faradaic efficiency of CO and HCOOH is high as summarizes in Table 2, and other products (C_1 and C_2 products) are challenging to be produced. For commercial electrochemical CO_2 conversion, achieving high-energy-dense C_2 products is crucial. However, there are few research findings on the selective formation of C_1 products (such as CH_4 and CH_3OH) and C_2 products (C_2H_4 and EtOH). In contrast, CO and HCOOH are the main products of Cu-sulfide-based, bimetallic and other MS-based catalysts. Therefore, more research is needed to investigate the use of MS-based nanomaterial in forming a wide range of products with high selectivity. More importantly, a long-term stability analysis is recommended to investigate the catalyst's poisoning or degradation, which is critical for the design and development of the catalyst.

(4) Finding the fundamental understanding of electrochemical reaction pathways through experimental and theoretical approaches. It is necessary to clarify the reaction mechanism with theoretical modelling and simulation and establish the structure–activity relationship to guide the subsequent catalyst structure design. Several literature reports show that DFT is an efficient tool for calculating reaction intermediates' energy values. However, it is well established that the theoretically predicted processes may differ with different DFT models. Furthermore, some calculations were shown to be theoretically feasible without experimental support. Thus, DFT analyses should be closely coupled with experiments to validate their feasibility for understanding reaction mechanisms. Some advanced characterization techniques, such as *in situ* electrochemical-spectroscopic methods, need to be developed, including *in situ* or operando electrochemical XRD, FTIR, Raman, XPS, synchrotron methods, *etc.*, to a better understanding of the reaction mechanisms.

Conflicts of interest

There are no conflicts to declare.

Acknowledgements

The authors gratefully acknowledge Birla Institute of Technology, Mesra for providing institute research fellowship and I-STEM/catalytic grant/acad_18/2022-2023 for the financial support.

References

1 S. J. Davis, K. Caldeira and H. D. Matthews, *Science*, 2010, **329**, 1330–1333.
2 M. I. Hoffert, *Science*, 2010, **329**, 1292–1294.
3 L. I. Eide, M. Batum, T. Dixon, Z. Elamin, A. Graue, S. Hagen, S. Hovorka, B. Nazarian, P. H. Nøkleby, G. I. Olsen, P. Ringrose and R. A. M. Vieira, *Energies*, 2019, **12**, 1945.
4 P. Falkowski, R. J. Scholes, E. Boyle, J. Canadell, D. Canfield, J. Elser, N. Gruber, K. Hibbard, P. Hogberg, S. Linder, F. T. Mackenzie, B. Moore, T. Pedersen, Y. Rosental, S. Seitzinger, V. Smetacek and W. Steffen, *Science*, 2000, **290**, 291–296.
5 B. M. Tackett, E. Gomez and J. G. Chen, *Nat. Catal.*, 2019, **2**, 381–386.
6 K. Teramura, S. Iguchi, Y. Mizuno, T. Shishido and T. Tanaka, *Angew. Chem., Int. Ed.*, 2012, **51**, 8008–8011.
7 H. Homayoni, W. Chanmanee, N. R. de Tacconi, B. H. Dennis and K. Rajeshwar, *J. Electrochem. Soc.*, 2015, **162**, E115–E122.
8 M. Li, E. Irtem, H.-P. Iglesias van Montfort, M. Abdinejad and T. Burdyny, *Nat. Commun.*, 2022, **131**(13), 1–11.
9 J. Guan, S. A. Berlinger, X. Li, Z. Chao, V. Sousa e Silva, S. Banta and A. C. West, *J. Biotechnol.*, 2017, **245**, 21–27.
10 R. Kortlever, I. Peters, S. Koper and M. T. M. Koper, *ACS Catal.*, 2015, **5**, 3916–3923.
11 M. Abdinejad, A. Seifitokaldani, C. Dao, E. H. Sargent, X. A. Zhang and H. B. Kraatz, *ACS Appl. Energy Mater.*, 2019, **2**, 1330–1335.
12 M. Abdinejad, C. Dao, B. Deng, F. Dinic, O. Voznyy, X. A. Zhang and H. B. Kraatz, *ACS Sustain. Chem. Eng.*, 2020, **8**, 9549–9557.
13 Z. Liang, J. Wang, P. Tang, W. Tang, L. Liu, M. Shakouri, X. Wang, J. Llorca, S. Zhao, M. Heggen, R. E. Dunin-Borkowski, A. Cabot, H. Bin Wu and J. Arbiol, *Appl. Catal. B Environ.*, 2022, **314**, 121451.
14 D. Kim, C. S. Kley, Y. Li and P. Yang, *Proc. Natl. Acad. Sci. U. S. A.*, 2017, **114**, 10560–10565.
15 Y. C. Li, Z. Wang, T. Yuan, D. H. Nam, M. Luo, J. Wicks, B. Chen, J. Li, F. Li, F. P. G. De Arquer, Y. Wang, C. T. Dinh, O. Voznyy, D. Sinton and E. H. Sargent, *J. Am. Chem. Soc.*, 2019, **141**, 8584–8591.
16 R. A. Geioushy, M. M. Khaled, K. Alhooshani, A. S. Hakeem and A. Rinaldi, *Electrochim. Acta*, 2017, **245**, 456–462.
17 A. Hasani, M. A. Teklagne, H. H. Do, S. H. Hong, Q. Van Le, S. H. Ahn and S. Y. Kim, *Carbon Energy*, 2020, **2**, 158–175.
18 J. Liu, C. Guo, A. Vasileff and S. Qiao, *Small Methods*, 2017, **1**.
19 P. Saha, S. Amanullah and A. Dey, *Acc. Chem. Res.*, 2022, **55**, 134–144.
20 G. F. Manbeck and E. Fujita, *J. Porphyr. Phthalocyanines*, 2015, **19**, 45–64, DOI: **10.1142/S1088424615300013**.
21 P. R. Yaashikaa, P. Senthil Kumar, S. J. Varjani and A. Saravanan, *J. CO_2 Util.*, 2019, **33**, 131–147.
22 A. Bagger, W. Ju, A. S. Varela, P. Strasser and J. Rossmeisl, *ChemPhysChem*, 2017, **18**, 3266–3273.
23 M. Todoroki, K. Hara, A. Kudo and T. Sakata, *J. Electroanal. Chem.*, 1995, **394**, 199–203.
24 G. O. Larrazábal, A. J. Martín, S. Mitchell, R. Hauert and J. Pérez-Ramírez, *ACS Catal.*, 2016, **6**, 6265–6274.
25 B. Ávila-Bolívar, L. García-Cruz, V. Montiel and J. Solla-Gullón, *Molecules*, 2019, **24**, 2032.
26 Q. Li, J. Fu, W. Zhu, Z. Chen, B. Shen, L. Wu, Z. Xi, T. Wang, G. Lu, J. J. Zhu and S. Sun, *J. Am. Chem. Soc.*, 2017, **139**, 4290–4293.
27 G. B. Damas, C. R. Miranda, R. Sgarbi, J. M. Portela, M. R. Camilo, F. H. B. Lima and C. M. Araujo, *Catal*, 2019, **9**, 636.

28 W. Zhu, R. Michalsky, Ö. Metin, H. Lv, S. Guo, C. J. Wright, X. Sun, A. A. Peterson and S. Sun, *J. Am. Chem. Soc.*, 2013, **135**, 16833–16836.
29 W. Zhu, Y. J. Zhang, H. Zhang, H. Lv, Q. Li, R. Michalsky, A. A. Peterson and S. Sun, *J. Am. Chem. Soc.*, 2014, **136**, 16132–16135.
30 K. Sun, L. Wu, W. Qin, J. Zhou, Y. Hu, Z. Jiang, B. Shen and Z. Wang, *J. Mater. Chem. A*, 2016, **4**, 12616–12623.
31 R. Wang, H. Haspel, A. Pustovarenko, A. Dikhtiarenko, A. Russkikh, G. Shterk, D. Osadchii, S. Ould-Chikh, M. Ma, W. A. Smith, K. Takanabe, F. Kapteijn and J. Gascon, *ACS Energy Lett.*, 2019, **4**, 2024–2031.
32 D. Hye Won, H. Shin, J. Koh, J. Chung, H. ee Sang Lee, H. Kim, S. Ihl Woo, D. H. Won, J. Chung, H. S. Lee, S. I. Woo, H. Shin, J. Koh and H. Kim, *Angew. Chem.*, 2016, **128**, 9443–9446.
33 W. Luo, J. Zhang, M. Li and A. Züttel, *ACS Catal.*, 2019, **9**, 3783–3791.
34 A. Klinkova, P. De Luna, C. T. Dinh, O. Voznyy, E. M. Larin, E. Kumacheva and E. H. Sargent, *ACS Catal.*, 2016, **6**, 8115–8120.
35 J. Zeng, W. Zhang, Y. Yang, D. Li, X. Yu and Q. Gao, *ACS Appl. Mater. Interfaces*, 2019, **11**, 33074–33081.
36 S. Pérez-Rodríguez, G. García, L. Calvillo, V. Celorrio, E. Pastor and M. J. Lázaro, *Int. J. Electrochem.*, 2011, **2011**, 1–13.
37 M. Umeda, Y. Niitsuma, T. Horikawa, S. Matsuda and M. Osawa, *ACS Appl. Energy Mater.*, 2020, **3**, 1119–1127.
38 F. A. Hanc-Scherer, M. A. Montiel, V. Montiel, E. Herrero and C. M. Sánchez-Sánchez, *Phys. Chem. Chem. Phys.*, 2015, **17**, 23909–23916.
39 T. Mizuno, M. Kawamoto, S. Kaneco and K. Ohta, *Electrochim. Acta*, 1998, **43**, 899–907.
40 R. Kortlever, J. Shen, K. J. P. Schouten, F. Calle-Vallejo and M. T. M. Koper, *J. Phys. Chem. Lett.*, 2015, **6**, 4073–4082.
41 Y. Hori, in *Modern Aspects of Electrochemistry*, Springer, New York, 2008, pp. 89–189.
42 S. Nitopi, E. Bertheussen, S. B. Scott, X. Liu, A. K. Engstfeld, S. Horch, B. Seger, I. E. L. Stephens, K. Chan, C. Hahn, J. K. Nørskov, T. F. Jaramillo and I. Chorkendorff, *Chem. Rev.*, 2019, **119**, 7610–7672.
43 E. Tayyebi, J. Hussain, Y. Abghoui and E. Skúlason, *J. Phys. Chem. C*, 2018, **122**, 10078–10087.
44 N. Atrak, E. Tayyebi and E. Skúlason, *Appl. Surf. Sci.*, 2021, **570**, 151031.
45 H. Chen, A. D. Handoko, T. Wang, J. Qu, J. Xiao, X. Liu, D. Legut, Z. Wei Seh and Q. Zhang, *ChemSusChem*, 2020, **13**, 5690–5698.
46 K. Kannan, M. H. Sliem, A. M. Abdullah, K. K. Sadasivuni and B. Kumar, *Catalysts*, 2020, **10**, 549.
47 Y. Ji, J. K. Nørskov and K. Chan, *J. Phys. Chem. C*, 2019, **123**, 4256–4261.
48 S. Kang, S. Ju, S. Han and Y. Kang, *J. Phys. Chem. C*, 2020, **124**, 25812–25820.
49 M. Abdinejad, C. Dao, X. an Zhang and H. B. Kraatz, *J. Energy Chem.*, 2021, **58**, 162–169.
50 M. Abdinejad, L. F. B. Wilm, F. Dielmann and H. B. Kraatz, *ACS Sustain. Chem. Eng.*, 2021, **9**, 521–530.
51 M. Abdinejad, I. Santos da Silva and H. B. Kraatz, *J. Mater. Chem. A*, 2021, **9**, 9791–9797.
52 M. Abdinejad, Z. Mirza, X. A. Zhang and H. B. Kraatz, *ACS Sustain. Chem. Eng.*, 2020, **8**, 1715–1720.
53 M. Li, K. Yang, M. Abdinejad, C. Zhao and T. Burdyny, *Nanoscale*, 2022, **14**, 11892–11908.
54 M. Abdinejad, M. K. Motlagh, M. Noroozifar and H. B. Kraatz, *Mater. Adv.*, 2022, **3**, 1224–1230.
55 M. Abdinejad, C. Ferrag, M. N. Hossain, M. Noroozifar, K. Kerman and H. B. Kraatz, *J. Mater. Chem. A*, 2021, **9**, 12870–12877.
56 J. Qiao, Y. Liu, F. Hong and J. Zhang, *Chem. Soc. Rev.*, 2014, **43**, 631–675.
57 X. Liu, J. Xiao, H. Peng, X. Hong, K. Chan and J. K. Nørskov, *Nat. Commun.*, 2017, **8**, 1–7.
58 Q. Kong, X. An, Q. Liu, L. Xie, J. Zhang, Q. Li, W. Yao, A. Yu, Y. Jiao and C. Sun, *Mater. Horiz.*, 2023, **10**, 698–721.
59 W. Sun, X. Zhao, E. Webb, G. Xu, W. Zhang and Y. Wang, *J. Mater. Chem. A*, 2023, **11**(5), 2092–2127.
60 M. Abdinejad, T. Yuan, K. Tang, S. Duangdangchote, A. Farzi, H.-P. Iglesias van Montfort, M. Li, J. of Middelkoop, M. of Wolff, A. Seifitokaldani, O. Voznyy, T. Burdyny, J. Middelkoop, M. Wolff, P. Thomas Burdyny and P. Oleksandr Voznyy, *Chem.– A Eur. J.*, 2023, **29**(14), e202203977.
61 W. Wang, L. Shang, G. Chang, C. Yan, R. Shi, Y. Zhao, G. I. N. Waterhouse, D. Yang and T. Zhang, *Adv. Mater.*, 2019, **31**, 1808276.
62 Q. Ding, B. Song, P. Xu and S. Jin, *Chem*, 2016, **1**, 699–726.
63 L. Zeng, J. Shi, J. Luo and H. Chen, *J. Power Sources*, 2018, **398**, 83–90.
64 Y. Zhang, L. Hu and W. Han, *J. Mater. Chem. A*, 2018, **6**, 23610–23620.
65 L. Hu, Y. Zhang and W. Han, *New J. Chem.*, 2019, **43**, 3269–3272.
66 Y. Dong, S. Yang, Z. Zhang, J. M. Lee and J. A. Zapien, *Nanoscale*, 2018, **10**, 3159–3165.
67 Y. Dong, M. Hu, Z. Zhang, J. A. Zapien, X. Wang and J. M. Lee, *Nanoscale*, 2018, **10**, 13343–13350.
68 M. Chhowalla, H. S. Shin, G. Eda, L. J. Li, K. P. Loh and H. Zhang, *Nat. Chem.*, 2013, **54**(5), 263–275.
69 M. Wang, L. Zhang, Y. He and H. Zhu, *J. Mater. Chem. A*, 2021, **9**, 5320–5363.
70 J. Joo, T. Kim, J. Lee, S. Il Choi and K. Lee, *Adv. Mater.*, 2019, **31**, 1806682.
71 Y. Guo, T. Park, J. W. Yi, J. Henzie, J. Kim, Z. Wang, B. Jiang, Y. Bando, Y. Sugahara, J. Tang and Y. Yamauchi, *Adv. Mater.*, 2019, **31**, 1807134.
72 P. Kulkarni, S. K. Nataraj, R. G. Balakrishna, D. H. Nagaraju and M. V. Reddy, *J. Mater. Chem. A*, 2017, **5**, 22040–22094.
73 G. Giuffredi, T. Asset, Y. Liu, P. Atanassov and F. Di Fonzo, *ACS Mater. Au*, 2021, **1**, 6–36.
74 S. L. Li, K. Tsukagoshi, E. Orgiu and P. Samorì, *Chem. Soc. Rev.*, 2015, **45**, 118–151.

75 S. Chandrasekaran, L. Yao, L. Deng, C. Bowen, Y. Zhang, S. Chen, Z. Lin, F. Peng and P. Zhang, *Chem. Soc. Rev.*, 2019, **48**, 4178–4280.
76 J. A. Dahl, B. L. S. Maddux and J. E. Hutchison, *Chem. Rev.*, 2007, **107**, 2228–2269.
77 S. Eustis and M. A. El-Sayed, *Chem. Soc. Rev.*, 2006, **35**, 209–217.
78 H. Şengül, T. L. Theis and S. Ghosh, *J. Ind. Ecol.*, 2008, **12**, 329–359.
79 L. Zeng, L. Tao, C. Tang, B. Zhou, H. Long, Y. Chai, S. P. Lau and Y. H. Tsang, *Sci. Rep.*, 2016, **6**, 1–8.
80 J. Tao, J. Chai, X. Lu, L. M. Wong, T. I. Wong, J. Pan, Q. Xiong, D. Chi and S. Wang, *Nanoscale*, 2015, **7**, 2497–2503.
81 Y. Zhong, X. Qiu, D. Chen, N. Li, Q. Xu, H. Li, J. He and J. Lu, *ACS Appl. Mater. Interfaces*, 2016, **8**, 28671–28677.
82 A. Jagadale, X. Zhou, D. Blaisdell and S. Yang, *Sci. Rep.*, 2018, **8**, 1–11.
83 M. S. M. Saifullah, M. Asbahi, M. Binti-Kamran Kiyani, S. Tripathy, E. A. H. Ong, A. Ibn Saifullah, H. R. Tan, T. Dutta, R. Ganesan, S. Valiyaveettil and K. S. L. Chong, *ACS Nano*, 2017, **11**, 9920–9929.
84 C. B. Roxlo, H. W. Deckman, J. Gland, S. D. Cameron and R. R. Chianelli, *Science*, 1987, **235**, 1629–1631.
85 A. Ambrosi, X. Chia, Z. Sofer and M. Pumera, *Electrochem. Commun.*, 2015, **54**, 36–40.
86 A. Kaltzoglou, P. Vaqueiro, T. Barbier, E. Guilmeau and A. V. Powell, *J. Electron. Mater.*, 2014, **43**, 2029–2034.
87 D. Voiry, H. Yamaguchi, J. Li, R. Silva, D. C. B. Alves, T. Fujita, M. Chen, T. Asefa, V. B. Shenoy, G. Eda and M. Chhowalla, *Nat. Mater.*, 2013, **12**, 850–855.
88 Y. Chen, J. Xi, D. O. Dumcenco, Z. Liu, K. Suenaga, D. Wang, Z. Shuai, Y. S. Huang and L. Xie, *ACS Nano*, 2013, **7**, 4610–4616.
89 J. Liu, Z. Zeng, X. Cao, G. Lu, L.-H. Wang, Q.-L. Fan, W. Huang and H. Zhang, *Small*, 2012, **8**, 3517–3522.
90 H. S. S. Ramakrishna Matte, A. Gomathi, A. K. Manna, D. J. Late, R. Datta, S. K. Pati and C. N. R. Rao, *Angew. Chem., Int. Ed.*, 2010, **49**, 4059–4062.
91 M. Abdinejad, K. Tang, C. Dao, S. Saedy and T. Burdyny, *J. Mater. Chem. A*, 2022, **10**, 7626–7636.
92 K. Kang, S. Xie, L. Huang, Y. Han, P. Y. Huang, K. F. Mak, C. J. Kim, D. Muller and J. Park, *Nature*, 2015, **520**, 656–660.
93 S. Zheng, L. Sun, T. Yin, A. M. Dubrovkin, F. Liu, Z. Liu, Z. X. Shen and H. J. Fan, *Appl. Phys. Lett.*, 2015, **106**, 063113.
94 E. Thimsen, S. V. Baryshev, A. B. F. Martinson, J. W. Elam, I. V. Veryovkin and M. J. Pellin, *Chem. Mater.*, 2013, **25**, 313–319.
95 E. Thimsen, S. C. Riha, S. V. Baryshev, A. B. F. Martinson, J. W. Elam and M. J. Pellin, *Chem. Mater.*, 2012, **24**, 3188–3196.
96 P. Yin, L. Sun, X. Han, C. Xia, H. Wu and F. Wang, *Rare Met. Mater. Eng.*, 2016, **45**, 1700–1704.
97 S. M. Lee, Y. N. Ko, S. H. Choi, J. H. Kim and Y. C. Kang, *Electrochim. Acta*, 2015, **167**, 287–293.
98 R. B. Ettlinger, A. Crovetto, S. Canulescu, A. Cazzaniga, L. Ravnkilde, T. Youngman, O. Hansen, N. Pryds and J. Schou, *Appl. Phys. A: Mater. Sci. Process.*, 2016, **122**, 1–10.
99 B. Li, L. Jiang, X. Li, P. Ran, P. Zuo, A. Wang, L. Qu, Y. Zhao, Z. Cheng and Y. Lu, *Sci. Rep.*, 2017, **7**, 1–12.
100 C. Liang, Y. Shimizu, T. Sasaki, H. Umehara and N. Koshizaki, *J. Phys. Chem. B*, 2004, **108**, 9728–9733.
101 X. Huang, M. G. Willinger, H. Fan, Z. L. Xie, L. Wang, A. Klein-Hoffmann, F. Girgsdies, C. S. Lee and X. M. Meng, *Nanoscale*, 2014, **6**, 8787–8795.
102 A. D. Mani, N. Xanthopoulos, D. Laub and C. H. Subrahmanyam, *J. Chem. Sci.*, 2014, **126**, 967–973.
103 N. M. Hosny and A. Dahshan, *J. Mol. Struct.*, 2015, **1085**, 78–83.
104 S. Vaidya, A. Patra and A. K. Ganguli, *Colloids Surf., A*, 2010, **363**, 130–134.
105 Z. Zhang, B. Xie, J. Li, B. Fang and Y. Lin, *Colloids Surf., A*, 2018, **546**, 203–211.
106 S. V. P. Vattikuti, C. Byon, C. V. Reddy, J. Shim and B. Venkatesh, *Appl. Phys. A: Mater. Sci. Process.*, 2015, **119**, 813–823.
107 S. Yadav and P. K. Bajpai, *Nano-Struct. Nano-Objects*, 2017, **10**, 151–158.
108 W. Dong, X. Wang, B. Li, L. Wang, B. Chen, C. Li, X. Li, T. Zhang and Z. Shi, *Dalton Trans.*, 2011, **40**, 243–248.
109 K. Li, Q. Wang, X. Cheng, T. Lv and T. Ying, *J. Alloys Compd.*, 2010, **504**, L31–L35.
110 J. C. Xing, Y. L. Zhu, M. Y. Li and Q. J. Jiao, *Electrochim. Acta*, 2014, **149**, 285–292.
111 S. Kamila, B. Mohanty, A. K. Samantara, P. Guha, A. Ghosh, B. Jena, P. V. Satyam, B. K. Mishra and B. K. Jena, *Sci. Rep.*, 2017, **7**, 1–13.
112 Y. J. Yuan, D. Chen, J. Zhong, L. X. Yang, J. Wang, M. J. Liu, W. G. Tu, Z. T. Yu and Z. G. Zou, *J. Mater. Chem. A*, 2017, **5**, 15771–15779.
113 A. Bhorde, A. Pawbake, P. Sharma, S. Nair, A. Funde, P. Bankar, M. More and S. Jadkar, *Appl. Phys. A: Mater. Sci. Process.*, 2018, **124**, 1–8.
114 C. Bara, A. F. Lamic-Humblot, E. Fonda, A. S. Gay, A. L. Taleb, E. Devers, M. Digne, G. D. Pirngruber and X. Carrier, *J. Catal.*, 2016, **344**, 591–605.
115 C. J. Chen and R. K. Chiang, *Dalt. Trans.*, 2011, **40**, 880–885.
116 Z. Liu, L. Zhang, R. Wang, S. Poyraz, J. Cook, M. J. Bozack, S. Das, X. Zhang and L. Hu, *Sci. Rep.*, 2016, **6**, 1–8.
117 D. H. Youn, J. W. Jang, J. Y. Kim, J. S. Jang, S. H. Choi and J. S. Lee, *Sci. Rep.*, 2014, **4**, 1–8.
118 C. W. Raubach, Y. V. B. De Santana, M. M. Ferrer, P. G. C. Buzolin, J. R. Sambrano and E. Longo, *Dalt. Trans.*, 2013, **42**, 11111–11116.
119 Y. Li, K. Ye, K. Cheng, J. Yin, D. Cao and G. Wang, *J. Power Sources*, 2015, **274**, 943–950.
120 Y. Chen, C. Davoisne, J. M. Tarascon and C. Guéry, *J. Mater. Chem.*, 2012, **22**, 5295–5299.
121 X. Rui, H. Tan and Q. Yan, *Nanoscale*, 2014, **6**, 9889–9924.
122 X. Jiang, Y. Xie, J. Lu, W. He, L. Zhu and Y. Qian, *J. Mater. Chem.*, 2000, **10**, 2193–2196.

123 P. Leidinger, R. Popescu, D. Gerthsen, H. Lünsdorf and C. Feldmann, *Nanoscale*, 2011, **3**, 2544–2551.
124 C. Wang, Z. Fang, F. Fan, X. Dong, Y. Peng, S. Hao and L. Long, *CrystEngComm*, 2013, **15**, 5792–5798.
125 L. Liu, H. Zhong, Z. Bai, T. Zhang, W. Fu, L. Shi, H. Xie, L. Deng and B. Zou, *Chem. Mater.*, 2013, **25**, 4828–4834.
126 Y. Chen, K. Chen, J. Fu, A. Yamaguchi, H. Li, H. Pan, J. Hu, M. Miyauchi and M. Liu, *Nano Mater. Sci.*, 2020, **2**, 235–247.
127 Y. Liu, Y. Deng, Z. Sun, J. Wei, G. Zheng, A. M. Asiri, S. B. Khan, M. M. Rahman and D. Zhao, *Small*, 2013, **9**, 2702–2708.
128 Y. Su, X. Lu, M. Xie, H. Geng, H. Wei, Z. Yang and Y. Zhang, *Nanoscale*, 2013, **5**, 8889–8893.
129 J. Liu and D. Xue, *J. Mater. Chem.*, 2011, **21**, 223–228.
130 H. Mazor, D. Golodnitsky, L. Burstein and E. Peled, *Electrochem. Solid-State Lett.*, 2009, **12**, A232.
131 C. Justin Raj, B. C. Kim, W. J. Cho, W. G. Lee, Y. Seo and K. H. Yu, *J. Alloys Compd.*, 2014, **586**, 191–196.
132 K. H. Liu, H. X. Zhong, S. J. Li, Y. X. Duan, M. M. Shi, X. B. Zhang, J. M. Yan and Q. Jiang, *Prog. Mater. Sci.*, 2018, **92**, 64–111.
133 A. Hasani, M. Tekalgne, Q. Van Le, H. W. Jang and S. Y. Kim, *J. Mater. Chem. A*, 2019, **7**, 430–454.
134 P. Geng, S. Zheng, H. Tang, R. Zhu, L. Zhang, S. Cao, H. Xue and H. Pang, *Adv. Energy Mater.*, 2018, **8**, 1703259.
135 Q. Yun, Q. Lu, X. Zhang, C. Tan and H. Zhang, *Angew. Chem., Int. Ed.*, 2018, **57**, 626–646.
136 Z. Fu, M. Wu, Y. Zhou, Z. Lyu, Y. Ouyang, Q. Li and J. Wang, *J. Mater. Chem. A*, 2022, **10**, 5699–5716.
137 A. W. Kahsay, K. B. Ibrahim, M. C. Tsai, M. K. Birhanu, S. A. Chala, W. N. Su and B. J. Hwang, *Catal. Lett.*, 2019, **149**, 860–869.
138 S. Wang, T. Kou, J. B. Varley, S. A. Akhade, S. E. Weitzner, S. E. Baker, E. B. Duoss and Y. Li, *ACS Mater. Lett.*, 2021, **3**, 100–109.
139 C. H. M. van Oversteeg, M. Tapia Rosales, K. H. Helfferich, M. Ghiasi, J. D. Meeldijk, N. J. Firet, P. Ngene, C. de Mello Donegá and P. E. de Jongh, *Catal. Today*, 2021, **377**, 157–165.
140 B. Zhang, M. Wang, J. Ding, Y. Li, G. Cao, M. T. Bernards, Y. He and Y. Shi, *J. CO2 Util.*, 2020, **39**, 101169.
141 X. Duan, J. Xu, Z. Wei, J. Ma, S. Guo, H. Liu and S. Dou, *Small Methods*, 2017, **1**, 1700156.
142 Q. Wang, Y. Lei, Y. Wang, Y. Liu, C. Song, J. Zeng, Y. Song, X. Duan, D. Wang and Y. Li, *Energy Environ. Sci.*, 2020, **13**, 1593–1616.
143 D. Voiry, H. S. Shin, K. P. Loh and M. Chhowalla, *Nat. Rev. Chem.*, 2018, **2**, 1–17.
144 D. Voiry, J. Yang and M. Chhowalla, *Adv. Mater.*, 2016, **28**, 6197–6206.
145 T. Shinagawa, G. O. Larrazábal, A. J. Martín, F. Krumeich and J. Pérez-Ramírez, *ACS Catal.*, 2018, **8**, 837–844.
146 J. W. Lim, W. J. Dong, J. Y. Park, D. M. Hong and J. L. Lee, *ACS Appl. Mater. Interfaces*, 2020, **12**, 22891–22900.
147 Z. Li, N. H. Attanayake, J. L. Blackburn and E. M. Miller, *Energy Environ. Sci.*, 2021, **14**, 6242–6286.
148 T. Heliso Dolla, T. Matthews, N. Wendy Maxakato, P. Ndungu and T. Montini, *J. Electroanal. Chem.*, 2023, **928**, 117049.
149 Q. G. Zhu, X. F. Sun, X. C. Kang, J. MA, Q. L. Qian and B. X. Han, *Acta Phys.-Chim. Sin.*, 2016, **32**, 261–266.
150 P. Shao, S. Ci, L. Yi, P. Cai, P. Huang, C. Cao and Z. Wen, *ChemElectroChem*, 2017, **4**, 2593–2598.
151 Y. Gao, Y. Guo, Y. Zou, W. Liu, Y. Luo, B. Liu and C. Zhao, *ACS Appl. Energy Mater.*, 2023, **6**(3), 1340–1354.
152 Z. Zhao, X. Peng, X. Liu, X. Sun, J. Shi, L. Han, G. Li and J. Luo, *J. Mater. Chem. A*, 2017, **5**, 20239–20243.
153 J. Chen, Y. Tu, Y. Zou, X. Li and J. Jiang, *Mater. Lett.*, 2021, **284**, 128919.
154 T. Dou, Y. Qin, F. Zhang and X. Lei, *ACS Appl. Energy Mater.*, 2021, **4**, 4376–4384.
155 X. Zhang, R. Sa, F. Zhou, Y. Rui, R. Liu, Z. Wen and R. Wang, *CCS Chem*, 2021, **3**, 199–207.
156 C. He, D. Duan, J. Low, Y. Bai, Y. Jiang, X. Wang, S. Chen, R. Long, L. Song and Y. Xiong, *Nano Res.*, 2021, DOI: 10.1007/s12274-021-3532-7.
157 K. R. Phillips, Y. Katayama, J. Hwang and Y. Shao-Horn, *J. Phys. Chem. Lett.*, 2018, **9**, 4407–4412.
158 Y. Deng, Y. Huang, D. Ren, A. D. Handoko, Z. W. Seh, P. Hirunsit and B. S. Yeo, *ACS Appl. Mater. Interfaces*, 2018, **10**, 28572–28581.
159 Y. Huang, Y. Deng, A. D. Handoko, G. K. L. Goh and B. S. Yeo, *ChemSusChem*, 2018, **11**, 320–326.
160 W. He, I. Liberman, I. Rozenberg, R. Ifraemov and I. Hod, *Angew. Chem.*, 2020, **132**, 8339–8346.
161 J. Li, J. Li, C. Dun, W. Chen, D. Zhang, J. Gu, J. J. Urban and J. W. Ager, *RSC Adv.*, 2021, **11**, 23948–23959.
162 L. Lin, N. Miao, Y. Wen, S. Zhang, P. Ghosez, Z. Sun and D. A. Allwood, *ACS Nano*, 2016, **10**, 8929–8937.
163 L. Dong, S. Guo, Y. Wang, Q. Zhang, L. Gu, C. Pan and J. Zhang, *J. Mater. Chem. A*, 2019, **7**, 27603–27611.
164 C. Wei, W. Wu, H. Li, X. Lin, T. Wu, Y. Zhang, Q. Xu, L. Zhang, Y. Zhu, X. Yang, Z. Liu and Q. Xu, *ACS Appl. Mater. Interfaces*, 2019, **11**, 25264–25270.
165 T. T. Zhuang, Z. Q. Liang, A. Seifitokaldani, Y. Li, P. De Luna, T. Burdyny, F. Che, F. Meng, Y. Min, R. Quintero-Bermudez, C. T. Dinh, Y. Pang, M. Zhong, B. Zhang, J. Li, P. N. Chen, X. L. Zheng, H. Liang, W. N. Ge, B. J. Ye, D. Sinton, S. H. Yu and E. H. Sargent, *Nat. Catal.*, 2018, **1**, 421–428.
166 C. Peng, G. Luo, J. Zhang, M. Chen, Z. Wang, T. K. Sham, L. Zhang, Y. Li and G. Zheng, *Nat. Commun.*, 2021, **12**, 1–8.
167 Y. P. Zhu, C. Guo, Y. Zheng and S. Z. Qiao, *Acc. Chem. Res.*, 2017, **50**, 915–923.
168 X. Wang, J. Lv, J. Zhang, X. L. Wang, C. Xue, G. Bian, D. Li, Y. Wang and T. Wu, *Nanoscale*, 2020, **12**, 772–784.
169 X. Han, T. Mou, S. Liu, M. Ji, Q. Gao, Q. He, H. Xin and H. Zhu, *Nanoscale Horiz.*, 2022, **7**, 508–514.
170 C. He, S. Chen, R. Long, L. Song and Y. Xiong, *Sci. China Chem.*, 2020, **63**, 1721–1726.
171 C. F. Wen, M. Zhou, P. F. Liu, Y. Liu, X. Wu, F. Mao, S. Dai, B. Xu, X. L. Wang, Z. Jiang, P. Hu, S. Yang, H. F. Wang and H. G. Yang, *Angew. Chem., Int. Ed.*, 2022, **61**(2), e202111700.

172 W. Xue, W. Chang, X. Hu, J. Fan and E. Liu, *Chinese J. Catal.*, 2021, **42**, 152–163.
173 P. Tan, A. Zhu, L. Qiao, W. Zeng, H. Cui and J. Pan, *J. Colloid Interface Sci.*, 2019, **533**, 452–462.
174 P. Tan, A. Zhu, L. Qiao, W. Zeng, Y. Ma, H. Dong, J. Xie and J. Pan, *Inorg. Chem. Front.*, 2019, **6**, 929–939.
175 K. Shen, X. Xue, X. Wang, X. Hu, H. Tian and W. Zheng, *RSC Adv.*, 2017, **7**, 23319–23327.
176 H. Rabizadeh, A. Feizbakhsh, H. Ahmad Panahi and E. Konoz, *Fuller. Nanotub. Carbon Nanostructures*, 2019, **27**, 788–795, DOI: 10.1080/1536383X.2019.1646251.
177 R. Shi, H. F. Ye, F. Liang, Z. Wang, K. Li, Y. Weng, Z. Lin, W. F. Fu, C. M. Che and Y. Chen, *Adv. Mater.*, 2018, **30**, 1705941.
178 J. W. Shi, D. Sun, Y. Zou, D. Ma, C. He, X. Ji and C. Niu, *Chem. Eng. J.*, 2019, **364**, 11–19.
179 R. Bin Wei, P. Y. Kuang, H. Cheng, Y. B. Chen, J. Y. Long, M. Y. Zhang and Z. Q. Liu, *ACS Sustain. Chem. Eng.*, 2017, **5**, 4249–4257.
180 R. Bin Wei, Z. L. Huang, G. H. Gu, Z. Wang, L. Zeng, Y. Chen and Z. Q. Liu, *Appl. Catal. B Environ.*, 2018, **231**, 101–107.
181 S. Sarkar and D. Basak, *ACS Appl. Mater. Interfaces*, 2015, **7**, 16322–16329.
182 Q. Lu, J. Rosen, Y. Zhou, G. S. Hutchings, Y. C. Kimmel, J. G. Chen and F. Jiao, *Nat. Commun.*, 2014, **51**(5), 1–6.
183 Y. Wu, P. Zhai, S. Cao, Z. Li, B. Zhang, Y. Zhang, X. Nie, L. Sun and J. Hou, *Adv. Energy Mater.*, 2020, **10**, 1–11.
184 F. Gao, S. Hu, X. Zhang, Y. Zheng, H. Wang, Z. Niu, P. Yang, R. Bao, T. Ma, Z. Dang, Y. Guan, X. Zheng, X. Zheng, J. Zhu, M. Gao and S. Yu, *Angew. Chem.*, 2020, **132**, 8784–8790.
185 R. He, A. Zhang, Y. Ding, T. Kong, Q. Xiao, H. Li, Y. Liu and J. Zeng, *Adv. Mater.*, 2018, **30**, 1–7.
186 Q. Xu, Y. Liu, H. Jiang, Y. Hu, H. Liu and C. Li, *Adv. Energy Mater.*, 2019, **9**, 1802553.
187 M. Shen, L. Zhang, M. Wang, J. Tian, X. Jin, L. Guo, L. Wang and J. Shi, *J. Mater. Chem. A*, 2019, **7**, 1556–1563.
188 F. Pan, B. Li, W. Deng, Z. Du, Y. Gang, G. Wang and Y. Li, *Appl. Catal. B Environ.*, 2019, **252**, 240–249.
189 T. Hou, N. Luo, Y. T. Cui, J. Lu, L. Li, K. E. MacArthur, M. Heggen, R. Chen, F. Fan, W. Tian, S. Jin and F. Wang, *Appl. Catal. B Environ.*, 2019, **245**, 262–270.
190 Y. H. Li, L. Cheng, P. F. Liu, L. Zhang, M. Y. Zu, C. W. Wang, Y. H. Jin, X. M. Cao, H. G. Yang and C. Li, *ChemSusChem*, 2018, **11**, 1421–1425.
191 L. Cheng, Y. Li, A. Chen, Y. Zhu and C. Li, *Chem. Commun.*, 2020, **56**, 563–566.
192 B. Qin, Y. Li, H. Wang, G. Yang, Y. Cao, H. Yu, Q. Zhang, H. Liang and F. Peng, *Nano Energy*, 2019, **60**, 43–51.
193 M. Naguib, M. Kurtoglu, V. Presser, J. Lu, J. Niu, M. Heon, L. Hultman, Y. Gogotsi and M. W. Barsoum, *Adv. Mater.*, 2011, **23**, 4248–4253.
194 M. Naguib, O. Mashtalir, J. Carle, V. Presser, J. Lu, L. Hultman, Y. Gogotsi and M. W. Barsoum, *ACS Nano*, 2012, **6**, 1322–1331.
195 Z. W. Seh, K. D. Fredrickson, B. Anasori, J. Kibsgaard, A. L. Strickler, M. R. Lukatskaya, Y. Gogotsi, T. F. Jaramillo and A. Vojvodic, *ACS Energy Lett.*, 2016, **1**, 589–594.
196 R. Meshkian, M. Dahlqvist, J. Lu, B. Wickman, J. Halim, J. Thörnberg, Q. Tao, S. Li, S. Intikhab, J. Snyder, M. W. Barsoum, M. Yildizhan, J. Palisaitis, L. Hultman, P. O. Å. Persson and J. Rosen, *Adv. Mater.*, 2018, **30**, 1706409.
197 Á. Morales-Garciá, F. Calle-Vallejo and F. Illas, *ACS Catal.*, 2020, **10**, 13487–13503.
198 Y. Wang, R. Du, Z. Li, H. Song, Z. Chao, D. Zu, D. Chong, N. Gao and C. Li, *Ceram. Int.*, 2021, **47**, 28321–28327.
199 L. Cheng, Y. Wang, Y. Li, Y. Shen, Y. Zhen, Z. Xing, L. Lin, A. Chen, Y. Zhu and C. Li, *ChemCatChem*, 2021, **13**, 1161–1164.
200 C. Zhan, F. Dattila, C. Rettenmaier, A. Bergmann, S. Kühl, R. García-Muelas, N. López and B. Roldan Cuenya, *ACS Catal.*, 2021, **11**, 7694–7701.
201 V. S. S. Mosali, X. Zhang, Y. Liang, L. Li, G. Puxty, M. D. Horne, A. Brajter-Toth, A. M. Bond and J. Zhang, *ChemSusChem*, 2021, **14**, 2924–2934.
202 X. L. Gou, J. Chen and P. W. Shen, *Mater. Chem. Phys.*, 2005, **93**, 557–566.
203 L. A. Burton, D. Colombara, R. D. Abellon, F. C. Grozema, L. M. Peter, T. J. Savenije, G. Dennler and A. Walsh, *Chem. Mater.*, 2013, **25**, 4908–4916.
204 M. R. Pallavolu, Y. Anil Kumar, G. Mani, R. A. Alshgari, M. Ouladsmane and S. W. Joo, *J. Electroanal. Chem.*, 2021, **899**, 115695.
205 C. Zhu, F. Wan, H. Ping, H. Wang, W. Wang and Z. Fu, *J. Power Sources*, 2021, **506**, 230180.
206 K. Li, S. Yan, Z. Lin and Y. Shi, *J. Alloys Compd.*, 2016, **681**, 486–491.
207 Y. Shan, Y. Li and H. Pang, *Adv. Funct. Mater.*, 2020, **30**, 2001298.
208 K. J. Norton, F. Alam and D. J. Lewis, *Appl. Sci.*, 2021, **11**, 2062.
209 Y. Li, J. P. Tu, X. H. Huang, H. M. Wu and Y. F. Yuan, *Electrochim. Acta*, 2006, **52**, 1383–1389.
210 J. Cai, Z. Li and P. K. Shen, *ACS Appl. Mater. Interfaces*, 2012, **4**, 4093–4098.
211 A. M. Tripathi and S. Mitra, *RSC Adv.*, 2014, **4**, 10358–10366.
212 K. Aso, A. Hayashi and M. Tatsumisago, *Cryst. Growth Des.*, 2011, **11**, 3900–3904.
213 Y. Zhang, J. Lu, S. Shen, H. Xu and Q. Wang, *Chem. Commun.*, 2011, **47**, 5226–5228.
214 D. D. Vaughn, O. D. Hentz, S. Chen, D. Wang and R. E. Schaak, *Chem. Commun.*, 2012, **48**, 5608–5610.
215 Z. Deng, H. Jiang, Y. Hu, C. Li, Y. Liu and H. Liu, *AIChE J.*, 2018, **64**, 1965–1974.
216 J. Wang, J. Liu, H. Xu, S. Ji, J. Wang, Y. Zhou, P. Hodgson and Y. Li, *J. Mater. Chem. A*, 2013, **1**, 1117–1122.
217 C. Zhai, N. Du and H. Z. D. Yang, *Chem. Commun.*, 2011, **47**, 1270–1272.
218 L. Wang, L. Zhuo, Y. Yu and F. Zhao, *Electrochim. Acta*, 2013, **112**, 439–447.

219 Y. Du, Z. Yin, X. Rui, Z. Zeng, X. J. Wu, J. Liu, Y. Zhu, J. Zhu, X. Huang, Q. Yan and H. Zhang, *Nanoscale*, 2013, **5**, 1456–1459.
220 J. Ma, D. Lei, L. Mei, X. Duan, Q. Li, T. Wang and W. Zheng, *CrystEngComm*, 2012, **14**, 832–836.
221 H. Zhong, G. Yang, H. Song, Q. Liao, H. Cui, P. Shen and C. X. Wang, *J. Phys. Chem. C*, 2012, **116**, 9319–9326.
222 J. Zai, K. Wang, Y. Su, X. Qian and J. Chen, *J. Power Sources*, 2011, **196**, 3650–3654.
223 J. Zai, X. Qian, K. Wang, C. Yu, L. Tao, Y. Xiao and J. Chen, *CrystEngComm*, 2012, **14**, 1364–1375.
224 J. Ma, D. Lei, X. Duan, Q. Li, T. Wang, A. Cao, Y. Mao and W. Zheng, *RSC Adv.*, 2012, **2**, 3615–3617.
225 A. A. Tedstone, D. J. Lewis and P. O'Brien, *Chem. Mater.*, 2016, **28**, 1965–1974.
226 X. Hong, K. Chan, C. Tsai and J. K. Nørskov, *ACS Catal.*, 2016, **6**, 4428–4437.
227 R. He, X. Yuan, P. Shao, T. Duan and W. Zhu, *Small*, 2019, **15**, 1–7.
228 A. Zhang, R. He, H. Li, Y. Chen, T. Kong, K. Li, H. Ju, J. Zhu, W. Zhu and J. Zeng, *Angew. Chem.*, 2018, **130**, 11120–11124.
229 X. Zheng, P. De Luna, F. P. García de Arquer, B. Zhang, N. Becknell, M. B. Ross, Y. Li, M. N. Banis, Y. Li, M. Liu, O. Voznyy, C. T. Dinh, T. Zhuang, P. Stadler, Y. Cui, X. Du, P. Yang and E. H. Sargent, *Joule*, 2017, **1**, 794–805.
230 Z. Chen, X. Zhang, M. Jiao, K. Mou, X. Zhang and L. Liu, *Adv. Energy Mater.*, 2020, **10**, 1–8.
231 F. Li, L. Chen, M. Xue, T. Williams, Y. Zhang, D. R. MacFarlane and J. Zhang, *Nano Energy*, 2017, **31**, 270–277.
232 J. He, X. Liu, H. Liu, Z. Zhao, Y. Ding and J. Luo, *J. Catal.*, 2018, **364**, 125–130.
233 H. Cheng, S. Liu, J. Zhang, T. Zhou, N. Zhang, X. S. Zheng, W. Chu, Z. Hu, C. Wu and Y. Xie, *Nano Lett.*, 2020, **20**, 6097–6103.
234 J. Xu, S. Lai, M. Hu, S. Ge, R. Xie, F. Li, D. Hua, H. Xu, H. Zhou, R. Wu, J. Fu, Y. Qiu, J. He, C. Li, H. Liu, Y. Liu, J. Sun, X. Liu and J. Luo, *Small Methods*, 2020, **4**, 1–8.
235 R. Sakthivel, S. Kubendhiran and S. M. Chen, *Ultrason. Sonochem.*, 2019, **54**, 68–78.
236 R. He, X. Qian, J. Yin and Z. Zhu, *J. Cryst. Growth*, 2003, **252**, 505–510.
237 P. Kumar Panigrahi and A. Pathak, *J. Nanopart.*, 2013, **2013**, 11.
238 D. B. Li, L. Hu, Y. Xie, G. Niu, T. Liu, Y. Zhou, L. Gao, B. Yang and J. Tang, *ACS Photonics*, 2016, **3**, 2122–2128.
239 W. Sun, X. Rui, D. Zhang, Y. Jiang, Z. Sun, H. Liu and S. Dou, *J. Power Sources*, 2016, **309**, 135–140.
240 S. S. Raut, J. A. Dhobale and B. R. Sankapal, *Phys. E*, 2017, **87**, 209–212.
241 D. Guo, C. Hu and C. Zhang, *Mater. Res. Bull.*, 2013, **48**, 1984–1988.
242 S. Sadhasivam, N. Anbarasan, M. Mukilan, P. Manivel and K. Jeganathan, *Int. J. Hydrogen Energy*, 2020, **45**, 30080–30090.
243 T. O. Ajiboye and D. C. Onwudiwe, *Results Chem.*, 2021, **3**, 100151.
244 S. Q. Liu, M. R. Gao, R. F. Feng, L. Gong, H. Zeng and J. L. Luo, *ACS Catal.*, 2021, **11**, 7604–7612.
245 Y. Zhang, F. Li, X. Zhang, T. Williams, C. D. Easton, A. M. Bond and J. Zhang, *J. Mater. Chem. A*, 2018, **6**, 4714–4720.
246 X. Yang, P. Deng, D. Liu, S. Zhao, D. Li, H. Wu, Y. Ma, B. Y. Xia, M. Li, C. Xiao and S. Ding, *J. Mater. Chem. A*, 2020, **8**, 2472–2480.
247 X. Shao and Y. Liu, *J. Electrochem. Soc.*, 2022, **169**, 026505.
248 C. Yang, J. Chai, Z. Wang, Y. Xing, J. Peng and Q. Yan, *Chem. Res. Chin. Univ.*, 2020, **36**, 410–419.
249 J. Wang, J. Mao, X. Zheng, Y. Zhou and Q. Xu, *Appl. Surf. Sci.*, 2021, **562**, 150197.
250 Y. Wang, X. Zhu and Y. Li, *J. Phys. Chem. Lett.*, 2019, **10**, 4663–4667.
251 X. Zou and Y. Zhang, *Chem. Soc. Rev.*, 2015, **44**, 5148–5180.
252 B. Hinnemann, P. G. Moses, J. Bonde, K. P. Jørgensen, J. H. Nielsen, S. Horch, I. Chorkendorff and J. K. Nørskov, *J. Am. Chem. Soc.*, 2005, **127**, 5308–5309.
253 T. F. Jaramillo, K. P. Jørgensen, J. Bonde, J. H. Nielsen, S. Horch and I. Chorkendorff, *Science*, 2007, **317**, 100–102.
254 W. Hua, H. H. Sun, F. Xu and J. G. Wang, *Rare Met.*, 2020, **39**, 335–351.
255 F. Qi, P. Li, Y. Chen, B. Zheng, X. Liu, F. Lan, Z. Lai, Y. Xu, J. Liu, J. Zhou, J. He and W. Zhang, *Vacuum*, 2015, **119**, 204–208.
256 M. Asadi, B. Kumar, A. Behranginia, B. A. Rosen, A. Baskin, N. Repnin, D. Pisasale, P. Phillips, W. Zhu, R. Haasch, R. F. Klie, P. Král, J. Abiade and A. Salehi-Khojin, *Nat. Commun.*, 2014, **5**, 1–8.
257 R. Tian, W. Wang, Y. Huang, H. Duan, Y. Guo, H. Kang, H. Li and H. Liu, *J. Mater. Chem. A*, 2016, **4**, 13148–13154.
258 L. Ma, G. Huang, W. Chen, Z. Wang, J. Ye, H. Li, D. Chen and J. Y. Lee, *J. Power Sources*, 2014, **264**, 262–271.
259 Y. Shi, Y. Wang, J. I. Wong, A. Y. S. Tan, C. L. Hsu, L. J. Li, Y. C. Lu and H. Y. Yang, *Sci. Rep.*, 2013, **3**, 1–8.
260 Q. Wang and J. Li, *J. Phys. Chem. C*, 2007, **111**, 1675–1682.
261 C. Wang, W. Wan, Y. Huang, J. Chen, H. H. Zhou and X. X. Zhang, *Nanoscale*, 2014, **6**, 5351–5358.
262 L. Fei, Y. Xu, X. Wu, G. Chen, Y. Li, B. Li, S. Deng, S. Smirnov, H. Fan and H. Luo, *Nanoscale*, 2014, **6**, 3664–3669.
263 F. Li, S. F. Zhao, L. Chen, A. Khan, D. R. MacFarlane and J. Zhang, *Energy Environ. Sci.*, 2016, **9**, 216–223.
264 K. Lv, W. Suo, M. Shao, Y. Zhu, X. Wang, J. Feng and M. Fang, *Nano Energy*, 2019, **63**, 103834.
265 N. Hussain, M. A. Abdelkareem, H. Alawadhi, K. Elsaid and A. G. Olabi, *Chem. Eng. Sci.*, 2022, **258**, 117757.
266 H. Li, X. Liu, S. Chen, D. Yang, Q. Zhang, L. Song, H. Xiao, Q. Zhang, L. Gu and X. Wang, *Adv. Energy Mater.*, 2019, **9**, 1–11.
267 G. Shi, L. Yu, X. Ba, X. Zhang, J. Zhou and Y. Yu, *Dalt. Trans.*, 2017, **46**, 10569–10577.
268 P. Abbasi, M. Asadi, C. Liu, S. Sharifi-Asl, B. Sayahpour, A. Behranginia, P. Zapol, R. Shahbazian-Yassar, L. A. Curtiss and A. Salehi-Khojin, *ACS Nano*, 2017, **11**, 453–460.

269 N. Hussain, M. A. Abdelkareem, H. Alawadhi, A. H. Alami and K. Elsaid, *Appl. Phys. A: Mater. Sci. Process.*, 2022, **128**, 15–20.
270 K. Lv, C. Teng, M. Shi, Y. Yuan, Y. Zhu, J. Wang, Z. Kong, X. Lu and Y. Zhu, *Adv. Funct. Mater.*, 2018, **28**, 1–10.
271 Z. W. Chen, W. Gao, W. T. Zheng and Q. Jiang, *ChemSusChem*, 2018, **11**, 1455–1459.
272 S. Kang, S. Han and Y. Kang, *ChemSusChem*, 2019, **12**, 2671–2678.
273 Q. Gong, L. Cheng, C. Liu, M. Zhang, Q. Feng, H. Ye, M. Zeng, L. Xie, Z. Liu and Y. Li, *ACS Catal.*, 2015, **5**, 2213–2219.
274 C. Xu, S. Peng, C. Tan, H. Ang, H. Tan, H. Zhang and Q. Yan, *J. Mater. Chem. A*, 2014, **2**, 5597–5601.
275 V. Kiran, D. Mukherjee, R. N. Jenjeti and S. Sampath, *Nanoscale*, 2014, **6**, 12856–12863.
276 J. Xu, X. Li, W. Liu, Y. Sun, Z. Ju, T. Yao, C. Wang, H. Ju, J. Zhu, S. Wei and Y. Xie, *Angew. Chem., Int. Ed.*, 2017, **56**, 9121–9125.
277 K. Chan, C. Tsai, H. A. Hansen and J. K. Nørskov, *ChemCatChem*, 2014, **6**, 1899–1905.
278 P. Pistor, J. M. M. Álvarez, M. León, M. Di Michiel, S. Schorr, R. Klenk and S. Lehmann, *Acta Crystallogr., Sect. B: Struct. Sci., Cryst. Eng. Mater.*, 2016, **72**, 410–415.
279 Y. Liu, H. Xu and Y. Qian, *Cryst. Growth Des.*, 2006, **6**, 1304–1307.
280 F. Ye, C. Wang, G. Du, X. Chen, Y. Zhong and J. Z. Jiang, *J. Mater. Chem.*, 2011, **21**, 17063–17065.
281 G. Li and H. Liu, *J. Mater. Chem.*, 2011, **21**, 18398–18402.
282 X. Yuan, Y. Luo, B. Zhang, C. Dong, J. Lei, F. Yi, T. Duan, W. Zhu and R. He, *Chem. Commun.*, 2020, **56**, 4212–4215.
283 A. Zhang, Y. Liang, H. Li, X. Zhao, Y. Chen, B. Zhang, W. Zhu and J. Zeng, *Nano Lett.*, 2019, **19**, 6547–6553.
284 L. P. Chi, Z. Z. Niu, X. L. Zhang, P. P. Yang, J. Liao, F. Y. Gao, Z. Z. Wu, K. Bin Tang and M. R. Gao, *Nat. Commun.*, 2021, **12**, 1–9.
285 J. Feng, H. Gao, J. Feng, L. Liu, S. Zeng, H. Dong, Y. Bai, L. Liu and X. Zhang, *ChemCatChem*, 2020, **12**, 926–931.
286 W. Ma, S. Xie, X. G. Zhang, F. Sun, J. Kang, Z. Jiang, Q. Zhang, D. Y. Wu and Y. Wang, *Nat. Commun.*, 2019, **10**, 892–901.
287 C. H. Lee and M. W. Kanan, *ACS Catal.*, 2015, **5**, 465–469.
288 J. E. Pander, J. W. J. Lum and B. S. Yeo, *J. Mater. Chem. A*, 2019, **7**, 4093–4101.
289 Z. Zhang, C. Liu, J. T. Brosnahan, H. Zhou, W. Xu and S. Zhang, *J. Mater. Chem. A*, 2019, **7**, 23775–23780.
290 X. Fang, T. Zhai, U. K. Gautam, L. Li, L. Wu, Y. Bando and D. Golberg, *Prog. Mater. Sci.*, 2011, **56**, 175–287.
291 Y.-C. Wang, I.-C. Leu, M.-H. Hon, Y. Xu, H. Wu, Y. Cai, X.-J. Xu, G.-T. Fei, W.-H. Yu, X.-W. Wang, L. Chen and L.-D. Zhang, *Nanotechnology*, 2005, **17**, 426.
292 G. H. Yue, P. X. Yan, D. Yan, X. Y. Fan, M. X. Wang, D. M. Qu and J. Z. Liu, *Appl. Phys. A*, 2006, **84**, 409–412.
293 X. Chen, H. Xu, N. Xu, F. Zhao, W. Lin, G. Lin, Y. Fu, Z. Huang, H. Wang and M. Wu, *Inorg. Chem.*, 2003, **42**, 3100–3106.
294 S.-H. Yu and M. Yoshimura, *Adv. Mater.*, 2002, **14**(4), 296–300.
295 Y. C. Zhu, Y. Bando and Y. Uemura, *Chem. Commun.*, 2003, **3**, 836–837.
296 S. Liang, X. Yeming and L. Quan, *Cryst. Growth Des.*, 2009, **9**, 2214–2219.
297 J. Z. Zhen, J. X. Liu, T. Y. Chen, F. Shi, Y. N. Dai, B. Yang, Y. F. Li, X. Wang, T. G. Nong, Y. Q. Hu and J. Shi, *J. Alloys Compd.*, 2019, **771**, 994–999.
298 C. Li, G. Shen, R. Zhang, D. Wu, C. Zou, T. Ling, H. Liu, C. Dong and X. W. Du, *J. Mater. Chem. A*, 2019, **7**, 1418–1423.
299 Y. Song, Y. Wang, J. Shao, K. Ye, Q. Wang and G. Wang, *ACS Appl. Mater. Interfaces*, 2022, **14**(18), 20368–20374.
300 V. V. Ivanovskaya and G. Seifert, *Solid State Commun.*, 2004, **130**, 175–180.
301 M. Inoue and H. Negishi, *J. Phys. Chem.*, 1986, **90**, 235–238.
302 A. Aljabour, H. Coskun, X. Zheng, M. G. Kibria, M. Strobel, S. Hild, M. Kehrer, D. Stifter, E. H. Sargent and P. Stadler, *ACS Catal.*, 2020, **10**, 66–72.
303 C. Simon, J. Zander, T. Kottakkat, M. Weiss, J. Timm, C. Roth and R. Marschall, *ACS Appl. Energy Mater.*, 2021, **4**, 8702–8708.
304 S. Zhao, S. Guo, C. Zhu, J. Gao, H. Li, H. Huang, Y. Liu and Z. Kang, *RSC Adv.*, 2017, **7**, 1376–1381.
305 S. Piontek, K. Junge Puring, D. Siegmund, M. Smialkowski, I. Sinev, D. Tetzlaff, B. Roldan Cuenya and U. P. Apfel, *Chem. Sci.*, 2019, **10**, 1075–1081.
306 D. Tetzlaff, K. Pellumbi, K. junge Puring, D. Siegmund, W. S. K. Polet, M. P. Checinski and U. P. Apfel, *ChemElectroChem*, 2021, **8**, 3161–3167.
307 K. Pellumbi, M. Smialkowski, D. Siegmund and U. P. Apfel, *Chem.–Eur. J.*, 2020, **26**, 9938–9944.
308 Z. Ma, T. Wan, D. Zhang, J. A. Yuwono, C. Tsounis, J. Jiang, Y.-H. Chou, X. Lu, P. V. Kumar, Y. H. Ng, D. Chu, C. Y. Toe, Z. Han and R. Amal, *ACS Nano*, 2023, **17**(3), 2387–2398.
309 D. Liu, Y. Liu and M. Li, *ACS Appl. Mater. Interfaces*, 2020, **124**(11), 6145–6153.
310 T. Cheng, H. Xiao and W. A. Goddard, *J. Am. Chem. Soc.*, 2016, **138**, 13802–13805.
311 X. Han, Q. Wang, Y. Wu and C. Wu, *Electrochim. Acta*, 2022, **402**, 139526.
312 P. Lu, X. Tan, H. Zhao, Q. Xiang, K. Liu, X. Zhao, X. Yin, X. Li, X. Hai, S. Xi, A. T. S. Wee, S. J. Pennycook, X. Yu, M. Yuan, J. Wu, G. Zhang, S. C. Smith and Z. Yin, *ACS Nano*, 2021, **15**, 5671–5678.
313 H. Yang, Y. Wu, G. Li, Q. Lin, Q. Hu, Q. Zhang, J. Liu and C. He, *J. Am. Chem. Soc.*, 2019, **141**, 12717–12723.
314 K. Lakshmanan, W. H. Huang, S. A. Chala, B. W. Taklu, E. A. Moges, J. F. Lee, P. Y. Huang, Y. C. Lee, M. C. Tsai, W. N. Su and B. J. Hwang, *Adv. Funct. Mater.*, 2022, **32**, 2109310.
315 L. Han, S. Song, M. Liu, S. Yao, Z. Liang, H. Cheng, Z. Ren, W. Liu, R. Lin, G. Qi, X. Liu, Q. Wu, J. Luo, H. L. Xin, X. Liu, Q. Wu, J. Luo and H. L. Xin, *J. Am. Chem. Soc.*, 2020, **142**, 12563–12567.

316 A. Guan, Z. Chen, Y. Quan, C. Peng, Z. Wang, T. K. Sham, C. Yang, Y. Ji, L. Qian, X. Xu and G. Zheng, *ACS Energy Lett.*, 2020, **5**, 1044–1053.
317 G. Qu, K. Wei, K. Pan, J. Qin, J. Lv, J. Li and P. Ning, *Nanoscale*, 2023, **15**, 3666–3692.
318 Z. Wang, C. Wang, Y. Hu, S. Yang, J. Yang, W. Chen, H. Zhou, F. Zhou, L. Wang, J. Du, Y. Li and Y. Wu, *Nano Res.*, 2021, **14**, 2790–2796.
319 J. Guo, W. Zhang, L. H. Zhang, D. Chen, J. Zhan, X. Wang, N. R. Shiju and F. Yu, *Adv. Sci.*, 2021, **8**, 2102884.
320 Y.-N. Gong, L. Jiao, Y. Qian, C.-Y. Pan, L. Zheng, X. Cai, B. Liu, S.-H. Yu and H.-L. Jiang, *Angew. Chem.*, 2020, **132**, 2727–2731.
321 S. Liu, M. Jin, J. Sun, Y. Qin, S. Gao, Y. Chen, S. Zhang, J. Luo and X. Liu, *Chem. Eng. J.*, 2022, **437**, 135294.
322 B. Chen, B. Li, Z. Tian, W. Liu, W. P. Liu, W. Sun, K. Wang, L. Chen and J. Jiang, *Adv. Energy Mater.*, 2021, **11**, 2102152.
323 H. Chang, H. Pan, F. Wang, Z. Zhang, Y. Kang and S. Min, *Nanoscale*, 2022, **14**, 10003–10008.
324 W. Hua, H. Sun, L. Lin, Q. Mu, B. Yang, Y. Su, H. Wu, F. Lyu, J. Zhong, Z. Deng and Y. Peng, *Chem. Eng. J.*, 2022, **446**, 137296.
325 H. Li, Y. Pan, Z. Wang, Y. Yu, J. Xiong, H. Du, J. Lai, L. Wang and S. Feng, *Nano Res.*, 2022, **15**, 3056–3064.
326 X. Sheng, W. Ge, H. Jiang and C. Li, *Adv. Mater.*, 2022, **34**, 2201295.
327 G. Hwa Jeong, Y. Chuan Tan, J. Tae Song, G. Y. Lee, H. Jin Lee, J. Lim, H. Young Jeong, S. Won, J. Oh and S. Ouk Kim, *Chem. Eng. J.*, 2021, **426**, 131063.
328 J. Feng, L. Zheng, C. Jiang, Z. Chen, L. Liu, S. Zeng, L. Bai, S. Zhang and X. Zhang, *Green Chem.*, 2021, **23**, 5461–5466.
329 S. A. Abbas, J. T. Song, Y. C. Tan, K. M. Nam, J. Oh and K. D. Jung, *ACS Appl. Energy Mater.*, 2020, **3**, 8739–8745.
330 H. Yang, P. Zhang, X. Yi, C. Yan, D. Pang, L. Chen, S. B. Wang, C. Wang, B. Liu, G. Zhang, Z. Zhou and X. Li, *Chem. Eng. J.*, 2022, **440**, 135749.
331 T. Ding, X. Liu, Z. Tao, T. Liu, T. Chen, W. Zhang, X. Shen, D. Liu, S. Wang, B. Pang, D. Wu, L. Cao, L. Wang, T. Liu, Y. Li, H. Sheng, M. Zhu and T. Yao, *J. Am. Chem. Soc.*, 2021, **143**, 11317–11324.
332 C. Wang, Y. Liu, H. Ren, Q. Guan, S. Chou and W. Li, *ACS Catal.*, 2022, **12**, 2513–2521.
333 K. Jiang, R. B. Sandberg, A. J. Akey, X. Liu, D. C. Bell, J. K. Nørskov, K. Chan and H. Wang, *Nat. Catal.*, 2018, **1**, 111–119.
334 M. Zheng, P. Wang, X. Zhi, K. Yang, Y. Jiao, J. Duan, Y. Zheng and S. Z. Qiao, *J. Am. Chem. Soc.*, 2022, **144**, 14936–14944.
335 Z. Gu, H. Shen, Z. Chen, Y. Yang, C. Yang, Y. Ji, Y. Wang, C. Zhu, J. Liu, J. Li, T. K. Sham, X. Xu and G. Zheng, *Joule*, 2021, **5**, 429–440.
336 H. Li, T. Liu, P. Wei, L. Lin, D. Gao, G. Wang and X. Bao, *Angew. Chem.*, 2021, **133**, 14450–14454.
337 D. Zhong, Z. J. Zhao, Q. Zhao, D. Cheng, B. Liu, G. Zhang, W. Deng, H. Dong, L. Zhang, J. Li, J. Li and J. Gong, *Angew. Chem., Int. Ed.*, 2021, **60**, 4879–4885.
338 Y. Wang, Z. Wang, C. T. Dinh, J. Li, A. Ozden, M. Golam Kibria, A. Seifitokaldani, C. S. Tan, C. M. Gabardo, M. Luo, H. Zhou, F. Li, Y. Lum, C. McCallum, Y. Xu, M. Liu, A. Proppe, A. Johnston, P. Todorovic, T. T. Zhuang, D. Sinton, S. O. Kelley and E. H. Sargent, *Nat. Catal.*, 2019, **32**(3), 98–106.
339 H. Xu, D. Rebollar, H. He, L. Chong, Y. Liu, C. Liu, C. J. Sun, T. Li, J. V. Muntean, R. E. Winans, D. J. Liu and T. Xu, *Nat. Energy*, 2020, **58**(5), 623–632.
340 C. Choi, S. Kwon, T. Cheng, M. Xu, P. Tieu, C. Lee, J. Cai, H. M. Lee, X. Pan, X. Duan, W. A. Goddard and Y. Huang, *Nat. Catal.*, 2020, **310**(3), 804–812.
341 C. Choi, T. Cheng, M. F. Espinosa, H. Fei, X. Duan, W. A. Goddard and Y. Huang, *Adv. Mater.*, 2019, **31**, 1805405.
342 B. Zhang, J. Zhang, M. Hua, Q. Wan, Z. Su, X. Tan, L. Liu, F. Zhang, G. Chen, D. Tan, X. Cheng, B. Han, L. Zheng and G. Mo, *J. Am. Chem. Soc.*, 2020, **142**, 13606–13613.
343 M. Zhong, K. Tran, Y. Min, C. Wang, Z. Wang, C. T. Dinh, P. De Luna, Z. Yu, A. S. Rasouli, P. Brodersen, S. Sun, O. Voznyy, C. S. Tan, M. Askerka, F. Che, M. Liu, A. Seifitokaldani, Y. Pang, S. C. Lo, A. Ip, Z. Ulissi and E. H. Sargent, *Nature*, 2020, **581**, 178–183.
344 S. Mou, Y. Li, L. Yue, J. Liang, Y. Luo, Q. Liu, T. Li, S. Lu, A. M. Asiri, X. Xiong, D. Ma and X. Sun, *Nano Res.*, 2021, (14), 2831–2836.
345 J. Zhu, M. Xiao, D. Ren, R. Gao, X. Liu, Z. Zhang, D. Luo, W. Xing, D. Su, A. Yu and Z. Chen, *J. Am. Chem. Soc.*, 2022, **144**, 9661–9671.
346 Q. Zhao, C. Zhang, R. Hu, Z. Du, J. Gu, Y. Cui, X. Chen, W. Xu, Z. Cheng, S. Li, B. Li, Y. Liu, W. Chen, C. Liu, J. Shang, L. Song and S. Yang, *ACS Nano*, 2021, **15**, 4927–4936.
347 D. Yang, Q. Zhu, C. Chen, H. Liu, Z. Liu, Z. Zhao, X. Zhang, S. Liu and B. Han, *Nat. Commun.*, 2019, **101**(10), 1–9.
348 M. K. Kim, H. J. Kim, H. Lim, Y. Kwon and H. M. Jeong, *Electrochim. Acta*, 2019, **306**, 28–34.
349 S. Chen, B. Wang, J. Zhu, L. Wang, H. Ou, Z. Zhang, X. Liang, L. Zheng, L. Zhou, Y. Q. Su, D. Wang and Y. Li, *Nano Lett.*, 2021, **21**, 7325–7331.
350 A. B. Laursen, K. U. D. Calvinho, T. A. Goetjen, K. M. K. Yap, S. Hwang, H. Yang, E. Garfunkel and G. C. Dismukes, *Electrochim. Acta*, 2021, **391**, 138889.
351 B. Wei, Y. Xiong, Z. Zhang, J. Hao, L. Li and W. Shi, *Appl. Catal. B Environ.*, 2021, **283**, 119646.